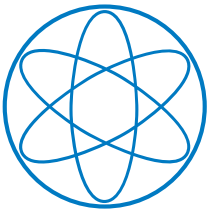

Cosmic Background Studies of a Silicon Drift Detector Setup for the IAXO Experiment

Studien des kosmischen Hintergrunds eines Silizium-Driftdetektor-Aufbaus für das IAXO-Experiment

Master Thesis

Lucinda Schönfeld

03695615

Course of studies:

Nuclear, Particle and Astrophysics

at the

Technical University of Munich

24.04.2024

Primary Reviewer:	Prof. Dr. Susanne Mertens
Secondary Reviewer:	Dr. Raimund Strauß
Supervisor:	Dr. Christoph Wiesinger

Abstract

Axions are hypothetical particles that were proposed to solve the strong CP problem but turn out to also be a compelling dark matter candidate. If they exist, they would be produced by the Sun, so one way to detect them would be by converting the solar axion flux to X-rays. One experiment that intends to do exactly that is the International Axion Observatory (IAXO). To achieve its ambitious goals, it needs a highly sensitive low-background X-ray detector. A promising technology in this regard are silicon drift detectors (SDDs). They potentially fulfill all requirements for BabyIAXO, the first stage of IAXO, if they can reach a background of $10^{-7}\,\mathrm{cts}/(\mathrm{cm}^2\,\mathrm{s}\,\mathrm{keV})$. Achieving this low background is especially challenging since the site where BabyIAXO will be built has only limited protection from cosmic shower particles.

This thesis focuses on mitigating the contribution of cosmic shower particles to the background of the SDD. It contains two parts: The first is about Monte Carlo simulation studies of the cosmic background in an above-ground setup. The second is about the development of a muon veto system for a setup meant to measure the background of the SDD.

The simulations are aimed at understanding how the above-ground flux of cosmic shower particles produces background in the SDD and how this background is affected by different shielding concepts. They reveal that the leading contributor to the cosmic background are neutrons and their interactions in the shielding. Since neutrons proliferate in common shielding materials like lead and are hard to eliminate, developing an effective shielding concept against them is key to reaching the BabyIAXO background goal. An approach using multiple layers of lead and borated polyethylene aimed at slowing down and capturing neutrons was shown to reduce the cosmic background significantly.

The muon veto is an essential element of the above-ground SDD demonstrator setup that is meant to take long-term background data. The veto is placed outside the passive shielding and tags muons that cause a coincident signal in the SDD. This thesis details all steps in setting up this veto. From the testing and characterization of the individual plastic scintillator panels, over the commissioning of the setup and development of a working data acquisition and analysis chain, to the first coincidence measurement with the veto and SDD together. The muon veto was shown to be effective at tagging prompt muon-induced events and is now ready for long-term background measurements.

Zusammenfassung

Axionen sind hypothetische Teilchen, die eingeführt wurden, um das Problem der starken CP-Verletzung lösen. Dabei stellten sie sich auch als exzellenter Kandidat für dunkle Materie heraus. Wenn sie existieren, wäre die Sonne eine starke Quelle für Axionen. Dementsprechend könnte man diese Teilchen nachweisen, indem man den Fluss solarer Axionen in messbare Röntgenstrahlung umwandelt. Ein Experiment mit genau diesem Ansatz ist das International Axion Observatory (IAXO). Um seine ehrgeizigen Ziele zu erreichen, benötigt es einen hochempfindlichen Röntgendetektor mit niedrigem Hintergrund. Eine vielversprechende Technologie in dieser Hinsicht sind Silizium-Driftdetektoren (SDDs). Sie erfüllen potenziell alle Anforderungen für BabyIAXO, die erste Stufe von IAXO, wenn sie einen Hintergrund von $10^{-7}\,\mathrm{cts}/(\mathrm{cm}^2\,\mathrm{s}\,\mathrm{keV})$ erreichen können. Dieser niedrige Hintergrund ist eine besondere Herausforderung, da der Standort, an dem BabyIAXO gebaut werden soll, nur begrenzt vor kosmischer Strahlung geschützt ist.

Der Fokus dieser Arbeit ist die Verringerung des kosmischen Beitrags zum Hintergrund des SDDs. Die Arbeit besteht aus zwei Teilen: Der erste befasst sich mit Monte-Carlo-Simulationen des kosmischen Hintergrunds in einem oberirdischen Versuchsaufbau. Der zweite umfasst die Entwicklung eines Myonen-Vetosystems für einen Versuchsaufbau, der den Hintergrund des SDDs messen soll.

Das Ziel der Simulationen ist ein besseres Verständnis dafür, wie der oberirdische Fluss kosmischer Schauerteilchen den Hintergrund im SDD erzeugt und welchen Einfluss verschiedene Abschirmungskonzepte darauf haben. Die Simulationen zeigen, dass Neutronen und deren Wechselwirkungen den größten Beitrag zum kosmischen Hintergrund leisten. Da sich Neutronen in gängigen Abschirmungsmaterialien wie Blei vermehren und nur schwer zu eliminieren sind, ist die Entwicklung eines wirksamen Abschirmungskonzepts gegen Neutronen essenziell, um das BabyIAXO-Hintergrundziel zu erreichen. Ein Konzept mit mehreren Schichten Blei und boriertem Polyethylen, die Neutronen verlangamen und einfangen, reduzierte den kosmischen Hintergrund erheblich.

Das Myonen-Veto ist ein Teil des oberirdischen SDD-Demonstrators, mit dem der Hintergrund des SDDs gemessen werden soll. Das Veto außerhalb der passiven Abschirmung und markiert Myonen, die ein koinzidentes Signal im SDD verursachen. Diese Arbeit beschreibt alle Schritte der Entwicklung dieses Vetos im Detail. Von der Charakterisierung der einzelnen Kunststoff-Szintillatorplatten über die Inbetriebnahme des Aufbaus und die Entwicklung einer Datenerfassungs- und Analysekette bis hin zur ersten Koinzidenzmessung mit dem Veto und dem SDD. Das Myonen-Veto identifiziert prompte Myonen-induzierten Ereignisse effektiv. Es ist nun bereit für langfristige Hintergrundmessungen.

Contents

1. Axions

The Standard Model (SM) of Elementary Particles is the most complete theory of particle physics to date. It describes all known elementary particles and their interactions, except for gravity. Its predictions closely agree with experimental findings even decades after its inception. Still, it does not explain all observations and leaves several questions unanswered. The hope of physicists today is to find an even more complete theory, explaining those phenomena the SM does not cover. The axion is a hypothetical particle that is a promising candidate for physics beyond the standard model, potentially solving several problems at once: The strong CP problem and the question as to the nature of dark matter.

Section 1.1 first gives a general introduction to the physics of the axion, outlining its theory and how it relates to the aforementioned open questions. Section 1.2 then delves into the current status of axion searches and their different experimental approaches.

1.1. Motivation

Axion-like particles (ALPs) show up in extensions of the SM that involve breaking one or several new symmetries. These extensions are usually devised to turn the SM into a more complete theory to explain a variety of observations that are hitherto not covered by it. The progenitor of these particles is the axion. Originally proposed to solve the strong CP problem, it serves as the blueprint for similar particles and has been the target of ongoing experimental searches [1, 2].

1.1.1. Strong CP Problem

CP symmetry is the invariance under combined charge conjugation (C) and parity transformation (P). It is maintained if a physical process stays the same when replacing particles with their antiparticles and mirroring space coordinates. Nature does not conserve CP symmetry. This was first observed in 1964 in kaon decays, proving that the weak interaction is CP-violating [3].

Quantum chromodynamics (QCD) is the theory that describes quarks, gluons, and their interactions via the strong force. Notably, the QCD Lagrangian contains the CP-violating term

$$\mathcal{L}_{\not{C}\not{P}} = \theta \frac{\alpha_s}{8\pi} G^a_{\mu\nu} \widetilde{G}^{\mu\nu}_a, \tag{1}$$

where α_s is the QCD-equivalent of the fine-structure constant, $G^a_{\mu\nu}$ and $\widetilde{G}^{\mu\nu}_a$ are the color field strength tensor and its dual, respectively, and θ is the vacuum angle of the theory. Since the term is odd under CP transformation, it induces CP-violating observables. One of them is an electric dipole moment of the neutron (nEDM), $d_n = C_{\mathrm{EDM}} \theta e$ with e the elementary charge. The coefficient C_{EDM} can be calculated within QCD, leading to [4]

$$d_n \approx 10^{-16}\, \theta e\, \mathrm{cm}. \tag{2}$$

The current experimental upper limit for the nEDM is [5]

$$|d_n| < 1.8 \times 10^{-26}\, e\, \mathrm{cm}, \tag{3}$$

which would require a vacuum angle of $\theta < 10^{-10}$. This is a surprisingly small value.

If QCD violates CP symmetry, we would expect to find an nEDM. Yet it has not been found, meaning that within current experimental limits, CP symmetry is conserved by the strong force. There is no fundamental reason that θ, which in theory could take any value between 0 and 2π, should be so small. Moreover, when looking at the SM as a whole, θ contains not just the bare QCD vacuum component, but also a contribution from the electroweak sector [2], which as we already know does violate CP symmetry. To explain experimental findings, the two independent contributions would have to cancel each other out almost exactly. This is a remarkable case of

fine-tuning. The question why QCD seemingly preserves CP symmetry is called the strong CP problem [6].

1.1.2. Peccei-Quinn Mechanism

A potential solution to this problem was proposed by Roberto Peccei and Helen Quinn in 1977 [7, 8]. They postulate that θ does not just happen to be small but is driven towards zero dynamically. They do this by introducing a new $U(1)$ symmetry and a complex scalar field ϕ. This field has the potential

$$V(\phi) = \lambda \left(|\phi|^2 - \frac{f_a^2}{2} \right)^2 , \tag{4}$$

where λ is a dimensionless coefficient and f_a is an energy scale that is not fixed by the theory. Above the scale f_a, the potential is parabolic with a minimum at 0, so ϕ vanishes. Below f_a, the potential takes on the 'Mexican hat' shape illustrated in Figure 1. The center is no longer a local minimum, so to minimize its energy the scalar field ϕ takes on a non-zero value in the valley of the hat. Since ϕ now has an arbitrary phase, the $U(1)$ symmetry is broken. The transition from the symmetry-conserving to the symmetry-breaking potential at f_a is called the Peccei-Quinn (PQ) transition.

The vacuum angle θ is no longer just a parameter of the QCD Lagrangian, but the phase of ϕ. This means that after the PQ transition, θ takes on an arbitrary value $\theta \in [0, 2\pi)$. The next step at the QCD energy scale of 200 MeV is the QCD transition illustrated in Figure 1. The PQ field interacts with the gluon field, which tilts the potential and gives it a new minimum. Due to the nature of these interactions, the minimum lies at the CP-conserving value of $\theta = 0$. Once again, ϕ minimizes its energy with respect to the PQ potential, resulting in θ vanishing. Thus, the PQ mechanism solves the strong CP problem.

According to the Goldstone theorem, a spontaneously broken symmetry produces a massless particle [9, 10]. Steven Weinberg and Frank Wilczek both realized that this also applies to the PQ mechanism that, by breaking its $U(1)$ symmetry, creates a new particle A [11, 12]. This is the axion. While it is massless after the initial PQ transition, the later QCD transition gives it a mass. A particle produced via spontaneous symmetry-breaking with non-zero mass is called a pseudo Nambu-Goldstone boson.

The axion can be understood as an angular degree of freedom of the field ϕ. Indeed, it can be defined in a way that absorbs the phase of ϕ. In other words, the original QCD vacuum angle, now phase of the PQ field, θ, can be redefined into the axion field $\theta \to \theta(t, x) = A(t, x)/f_a$. The axion is a new elementary particle that arises as a natural consequence of the PQ mechanism.

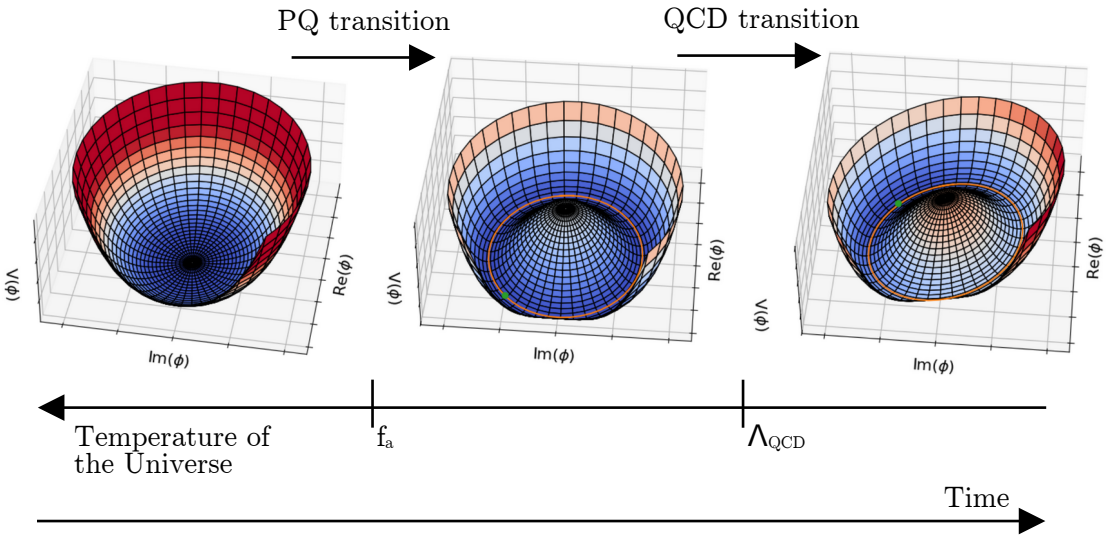

Figure 1: **Visualization of the Peccei-Quinn mechanism**
The complex scalar field ϕ always takes on a value that minimizes its vacuum energy with respect to the PQ potential $V(\phi)$. In the early Universe, at energies above f_a, the PQ potential is parabolic and ϕ is zero. Below the energy scale f_a, the potential takes on a Mexican hat shape. The radius of the valley of this hat is f_a, so a larger energy means a broader hat and vice versa. The vacuum expectation value of the field $\langle\phi\rangle$ is no longer zero, but $\langle\phi\rangle = f_a/\sqrt{2}$. The phase θ of the field takes on an arbitrary value. This breaks the initial $U(1)$ symmetry. This symmetry breaking creates a new boson, the axion. The axion field can be understood as an angular degree of freedom in the bottom of the potential, its value visualized as a green marble inside the hat. At this point, the axion is still massless. During the QCD transition at the energy scale of $\Lambda_{QCD} \approx 200\,\mathrm{MeV}$, the gluon field starts interacting with the PQ potential and causes the latter to tilt. There is now a singular minimum that the axion 'rolls' towards from its initial position. This is called the vacuum realignment mechanism, since the vacuum of the field has to realign itself with the new value. The realignment makes the field oscillate around the potential minimum. These oscillations lead to the vacuum state of the axion field having non-zero energy, which means that the associated particle has a rest mass. Figure adapted from [1].

1.1.3. Properties of the Axion

The production mechanism of the axion informs its properties. The decay constant is also the energy scale f_a of the PQ $U(1)$ symmetry breaking. The axion mass m_a is inversely proportional to the same parameter [13]:

$$m_a = 5.70(7)\,\mu\mathrm{eV}\left(\frac{10^{12}\,\mathrm{GeV}}{f_a}\right) \propto \frac{1}{f_a}. \tag{5}$$

This mass comes from QCD effects, meaning that it vanishes at energy scales larger than the QCD scale around 200 MeV. Just like the mass, the axion couplings to other particles are inversely proportional to f_a. An example is the axion-photon coupling [1]

$$g_{a\gamma} = \frac{\alpha}{2\pi}\frac{C_{a\gamma}}{f_a}, \tag{6}$$

where $C_{a\gamma}$ is a coefficient that contains two terms. One is constant and the other one depends on the chosen axion model, meaning how the PQ Lagrangian is integrated into the SM. Axions also inherently couple to gluons. There is a model-independent axion-nucleon coupling, whereas the axion-electron coupling is fully model-dependent [1].

Experimental axion searches usually focus on the axion-photon coupling by exploiting the inverse Primakoff effect as their detection channel. This effect describes the conversion of the weakly interacting axion into a detectable photon in a magnetic field, see Figure 2. The reverse, a photon converting to an axion, is the Primakoff effect [1, 2]. For larger distances, both processes can also be understood as oscillations between axions and photons. The distance of these oscillations depends on the axion decay constant f_a. According to Equation (6), a larger constant f_a means a weaker coupling $g_{a\gamma}$ and with that a larger oscillation length.

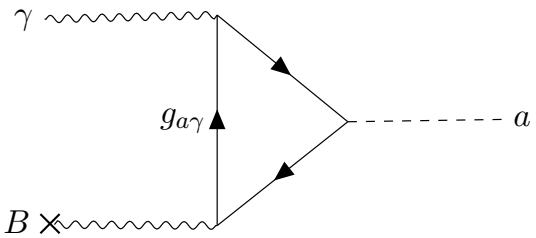

Figure 2: **Feynman diagram of the Primakoff effect**
A photon γ interacts with a virtual photon emitted by a strong electromagnetic field B and is converted into an axion a. The same diagram, read from right to left, also works for an axion interacting with the virtual photon and being converted to a photon. The likelihood of this process is determined by the strength of the axion-photon coupling $g_{a\gamma}$.

1.1.4. Axion-Like Particles

The original PQ theory has the symmetry-breaking energy scale f_a manually set to the electroweak scale $f_a \approx 250\,\text{GeV}$. However, the same mechanism also works for an arbitrary f_a, and produces a pseudo Nambu-Goldstone boson in all cases. As a matter of fact, the original PQ axion has already been excluded by experimental searches. If the energy scale f_a were of the same order as the electroweak scale, it would lead to signatures that should have been found already, but were never detected [14].

The original PQ axion theory has been supplanted by several newer, modified axion theories [15, 16, 17]. More generally, there are many other extensions of the SM that feature the spontaneous breaking of $U(1)$ symmetries. Those extensions also produce pseudo Nambu-Goldstone bosons, collectively referred to as axion-like particles (ALPs) [18]. Since their production is similar to the axion, their properties are similar as well, i.e., their mass and coupling to other particles are inversely proportional to their decay constant, which is also the scale of the breaking of their $U(1)$ symmetry, and they experience the Primakoff effect. What sets them apart

from the axion is that they do not solve the strong CP problem. Most axion experiments do not just search for axions, but ALPs in general, which is why the terms are often used loosely interchangeably. In this thesis, I use the term 'QCD axion' when referring specifically to the axion that also solves the strong CP problem.

1.1.5. Dark Matter

One of the biggest open questions in physics concerns the nature of dark matter, which makes up around 85% of matter in the Universe [19]. It affects the Cosmos in many ways through its gravitational attraction but has never been observed directly. Axions, since they are massive but barely interact with ordinary matter, are a well-suited candidate for dark matter.

Cosmological observations favor so-called cold dark matter that allows for the formation of large-scale structures in the Universe [20]. Axions are produced via the PQ mechanism non-thermally, which makes them a cold dark matter candidate. There are two scenarios for the production of axions in the early Universe: Either the PQ transition happens before the inflation stage, or it happens after. Each scenario produces different restraints on the axion properties for them to be good dark matter candidates, although in general their mass should be below 1 eV [20, 21].

Peccei and Quinn originally endeavored to solve the strong CP problem, one of the big unsolved problems in physics today. Almost as a side effect, they created a particle that could be dark matter and therefore answer another big open question in physics. However, this particle has not yet been experimentally found.

1.2. Experimental Searches

Since axion experiments are sensitive to the axion-photon coupling $g_{a\gamma}$, and both $g_{a\gamma}$ and the axion mass m_a are inversely proportional to the decay constant f_a, the $g_{a\gamma}$-m_a plane is usually used as the parameter space of axion searches. ALPs can fill the full parameter space, but the QCD axion only occupies a limited area. Axion search experiments usually focus on the sub-eV mass region since this is where axions can be dark matter [20].

There are various experiments searching for axions in different ways. They are complementary since they make different model assumptions and cover different areas of parameter space. The current exclusion limits are summarized in Figure 3. The data is from an open-access repository that continuously collects axion limits and includes references to all individual papers [22]. The different experimental approaches are described in more detail in this chapter.

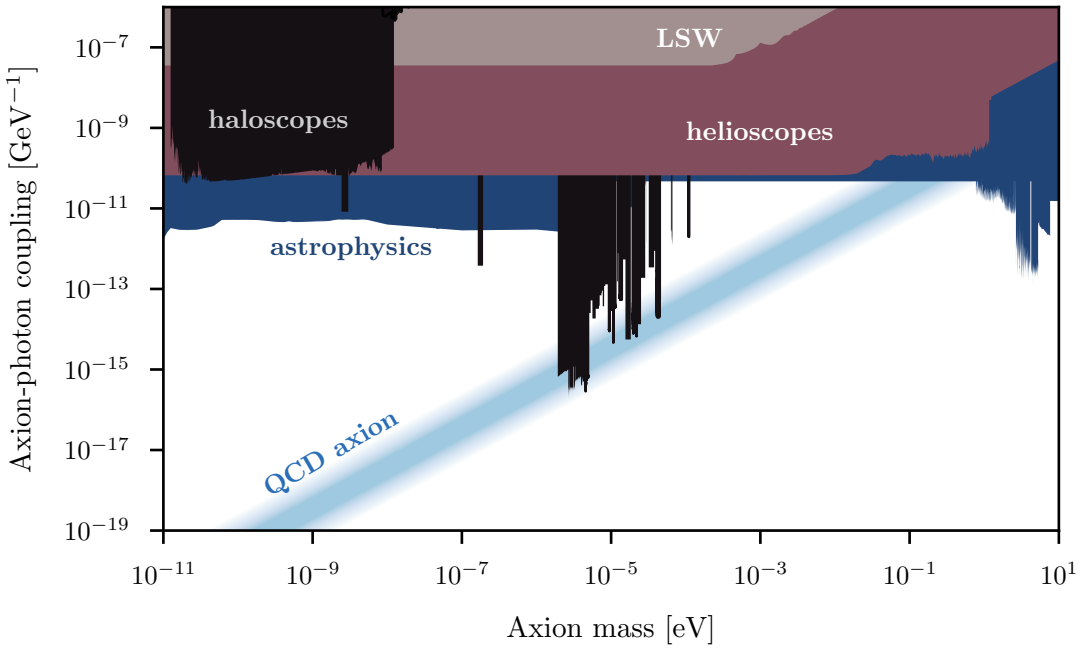

Figure 3: **Axion search exclusion limits**
Current limits on the axion-photon coupling as a function of the axion mass. The light blue band (**QCD axion**) indicates the parameter space of axions that solve the strong CP problem. Dark blue areas labelled **astrophysics** are exclusion limits from astrophysical observations. The black areas labelled **haloscopes** are limits from dark matter axion searches. The area labelled **LSW** is the current limit from light shining through a wall experiments. The area labeled **helioscopes** is the limit set by previous helioscope experiments. Data taken from [22].

Despite not being dedicated axion experiments, over a large mass range astrophysical observations pose the most stringent bounds on the axion-photon coupling. The cores of stars contain strong electromagnetic fields that could transform photons to axions via the Primakoff effect. These axions could easily leave the star and transport energy out of it. This would accelerate the cooling of the star and im-

pact its evolution and other properties. Analyzing star populations, white dwarfs, supernovae, and other stellar objects can therefore give limits on the axion-photon coupling [23]. Telescopes can also look for photon flux as an indication of axions, for example from axion decays or axion conversions to photons in cosmic electromagnetic fields [24].

1.2.1. Haloscopes

If axions constitute most or all of dark matter, they must make up the dark matter halo that envelops our galaxy. Since their production in the early universe through the PQ mechanism is non-thermal, they have low kinetic energy. This means that the population of dark matter axions can be described as a classical coherent field that fills the Universe. The frequency of the field corresponds to the mass of the particle. The basic assumption of haloscopes is that the dark matter halo surrounding us is this axion field.

The original type of haloscope tries to detect this axion field by converting it to microwaves in a strong magnetic field. To create a measurable signal, these experiments tune the geometry of their setup to different resonance frequencies. If the resonance of the setup matches the frequency of the axion field, it creates a signal. Haloscopes can investigate axion-photon couplings down to $10^{-16}\,\mathrm{GeV}^{-1}$, lower than any other experiments. On the other hand, they have to scan across the axion mass range one frequency at a time. Likewise, since the wavelength of the axion field must match the geometry of the setup exactly, these haloscopes are currently limited to the $10^{-6}\,\mathrm{eV}$ to $10^{-3}\,\mathrm{eV}$ axion mass range due to technical restraints of building smaller or larger experiments [25, 26].

A newer type of haloscope tries to detect the modulation of an oscillating magnetic field that would be induced by the dark matter axion field coupling to it. These experiments are sensitive to much lighter axion masses below $10^{-7}\,\mathrm{eV}$, whose wavelengths would be too small to detect with conventional haloscopes [27].

1.2.2. Light Shining Through a Wall

Of course, there is the possibility that axions exist, but do not make up a significant amount of dark matter. Light shining through a wall (LSW) experiments take this possibility into account by creating axions in the lab. They shoot a laser beam at a wall that stops photons. On both sides of the wall, cavities are placed in magnetic fields to allow the Primakoff effect and its inverse to take place. The photons of the laser beam can be converted to axions and pass the wall unhindered. Once they pass the wall, they can be converted back to photons and thus detected. As opposed to the dark matter searches described above, the sensitivity of LSW experiments is largely independent of the axion mass. This holds true up until the point where the oscillation length of the axion field exceeds the scale of the experiment around 100 m. At higher masses, the sensitivity drops [28].

Since LSW experiments produce axions in the lab, they do not rely on any assumptions other than the Primakoff effect, which is inherent to all axion models. On the other hand, they are looking for the double conversion of photon-axion-photon. The likelihood of this happening is proportional to $g_{a\gamma}^4$ as opposed to $g_{a\gamma}^2$ for a single conversion [28, 1]. For this reason, LSW experiments have a lower sensitivity to $g_{a\gamma}$ than all other experiments.

1.2.3. Helioscopes

Helioscopes have a similar experimental approach to LSW experiments. They too try to detect axions by converting them to photons in a strong magnetic field. The difference is that helioscopes do not convert photons to axions in the first place, mitigating the difficulty of trying to measure the exceedingly rare double conversion. Instead, they rely on the Sun to produce axions.

Both photons and strong electromagnetic fields are present in the Sun, so Primakoff conversion can take place and produce axions that escape the Sun's core. Since the light emitted by the Sun follows a black-body spectrum, the axion flux converted from these photons should have a similar distribution, shown in Figure 4.

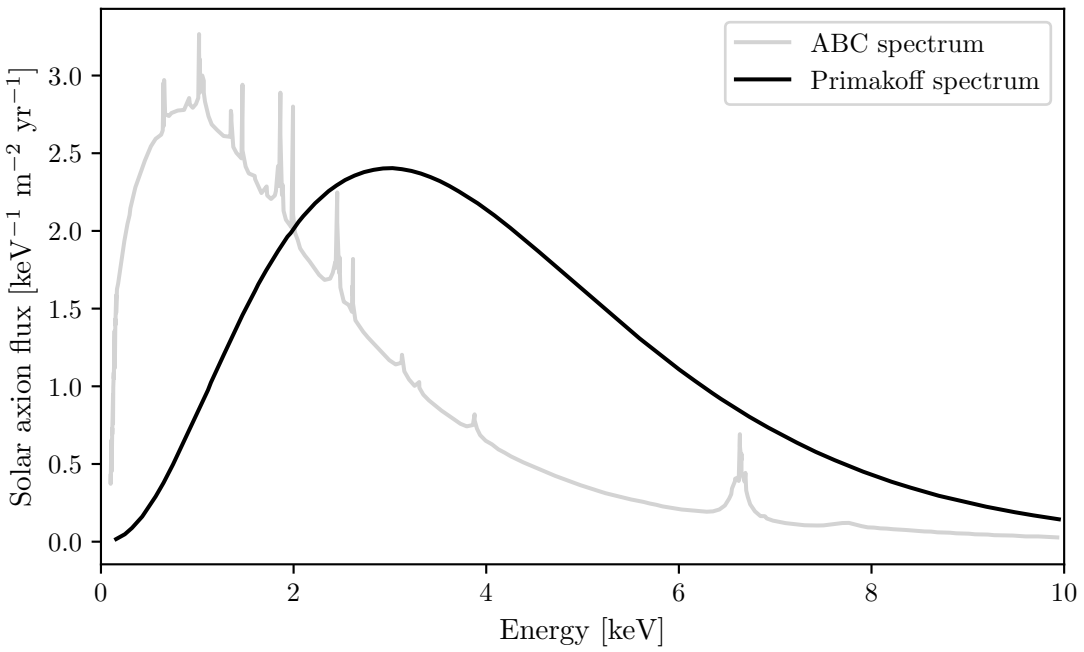

Figure 4: **Solar axion flux**
Expected flux of axions produced in the Sun for the axion-photon coupling $g_{a\gamma} = 10^{-11}\,\mathrm{GeV}^{-1}$ and axion-electron coupling $g_{ae} = 10^{-13}$. The values were chosen for illustration purposes. Axions converted from photons inside the Sun's core are expected to follow the so-called Primakoff spectrum. The ABC spectrum describes axions that are produced from electrons. The production mechanisms in the latter case are more complex and diverse, resulting in various features in the spectrum. Data from from [1].

In addition to the Primakoff spectrum, Figure 4 also shows the ABC spectrum, so called for the atomic, bremsstrahlung and Compton processes that produce axions from electrons. This spectrum has more features than the simple black-body spectrum of axions from solar photons. However, the axion-electron coupling is also much more model-dependent than the axion-photon coupling. This is why helioscopes primarily look for the Primakoff spectrum to detect axions. Once they are found, the ABC spectrum can give more detailed insights into the physics of the discovered axion.

Helioscopes are essentially X-ray telescopes looking at the Sun, as shown in Figure 5. Solar axions are converted to X-rays inside a strong magnet to produce a measurable signal. The strength of this signal depends on the strength of the axion-photon coupling, but also on the strength of the magnetic field where the conversion takes place.

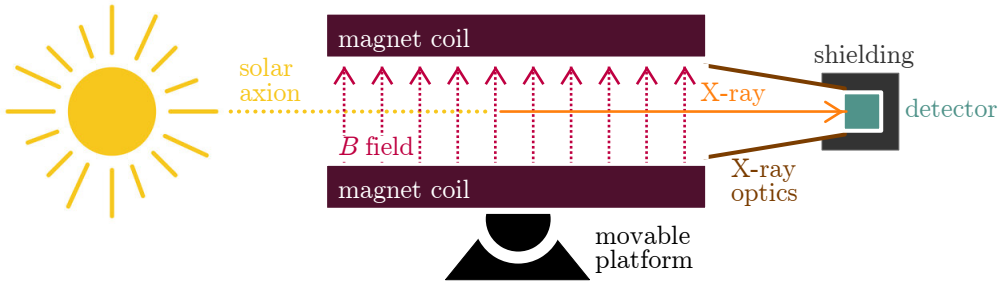

Figure 5: **Helioscope schema**
The heart of the helioscope are the magnet coils producing a strong magnetic field within. This is where solar axions are converted to X-rays. They are then focused onto the detector by an X-ray optics system. The detector is surrounded by shielding to reduce background. The entire device sits on a movable platform so it can track the motion of the Sun.

The reason for the characteristic shape of the helioscope exclusion limit is the same one as for LSW experiments. At some point, the oscillation wavelength between axion and photon becomes too large for the experiment and the sensitivity drops. This can be mitigated by filling the cavity inside the helioscope with a gas, effectively giving mass to the photon and altering the oscillation wavelength. This explains the extension of the helioscope sensitivity to masses $m_a \gtrsim 10^{-1}\,\mathrm{eV}$.

The most recent helioscope was the CERN Axion Solar Telescope (CAST). The experiment also set the most stringent limits of any helioscope to date at a coupling $g_{a\gamma} < 8.8 \times 10^{-11}\,\mathrm{GeV}^{-1}$ (95% CL) in a mass range up to $m_a \lesssim 0.02\,\mathrm{eV}$ [29]. Many CAST collaboration members have moved on to its successor, which aims to improve the solar axion detection limits even further.

2. International Axion Observatory

The International Axion Observatory (IAXO) is the next-generation axion helioscope currently in development. It is the successor to CAST and aims to surpass the sensitivity of that experiment by more than an order of magnitude to probe new regimes of axion-photon coupling, including part of the QCD axion band. Achieving this goal requires highly sensitive low-background detectors. One subgroup of IAXO is investigating silicon drift detectors (SDDs), a relatively new type of semiconductor detector, for this purpose. The group has built a custom setup to demonstrate that the stringent background requirements can be met with their technology, pioneering the use of SDDs in such a low-background experiment.

Section 2.1 first describes the goals of IAXO and how it aims to outdo CAST, before Section 2.2 showcases the IAXO prototype BabyIAXO currently in development. Section 2.3 addresses the requirements for the helioscope's X-Ray detector and the different detector types that are being developed receive their own section. Finally, Section 2.4 covers one specific detector type, the SDD, explaining the technology behind it and how the SDD performs in the context of IAXO. The section also introduces the setup meant to show the low-background performance of the detector, which leads directly into my own work in Chapters 3 and 4.

2.1. Goals

The IAXO experiment, shown in Figure 6, aims to surpass CAST in scale and technology to probe new regimes in solar axion parameter space [30]. While primarily a helioscope, IAXO also has potential for other physics applications. For example, the RADES project wants to use the strong magnet for an integrated haloscope experiment [31]. IAXO could also search for other hypothetical particles like dark photons [32]. Most importantly however, it will have significant potential for the discovery of solar axions.

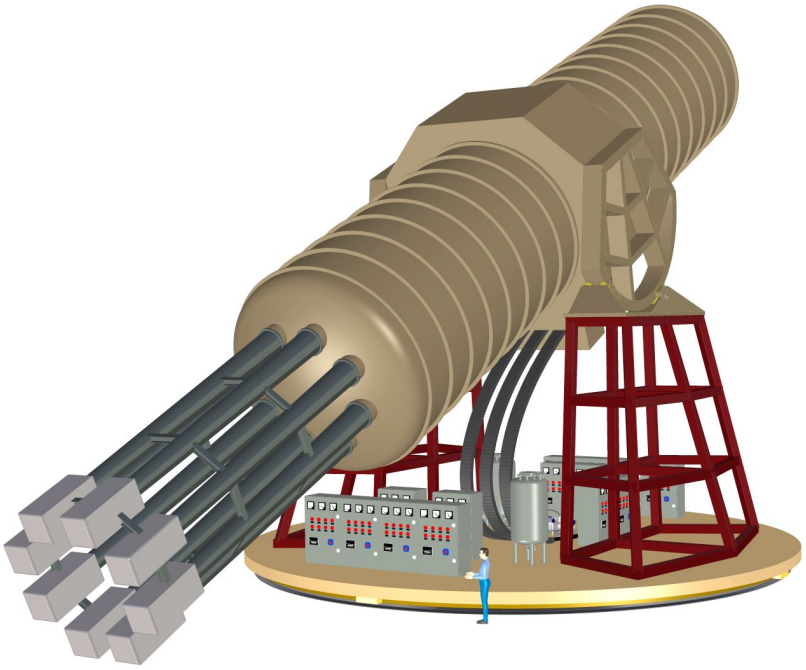

Figure 6: **Conceptual sketch of IAXO**
IAXO contains all the elements of a helioscope shown in Figure 5. The big beige tube is a cryostat containing the 20 m long superconducting magnet. It has eight bores of 60 cm diameter, each of which equipped with a set of X-Ray optics to focus the signal into a sub-cm^2 spot. At the end of the optics system are eight detectors surrounded by shielding to operate with minimal background. The mobile platform allows the helioscope to track the Sun. Adapted from [30].

IAXO will be mounted on a fully mobile platform to follow the Sun across the sky for 12 hours a day, vastly improving its exposure time compared to CAST that could only track the Sun during dusk and dawn. Previous helioscopes all used recycled magnets, for example the one in CAST was originally a LHC prototype [33]. IAXO will have a custom magnet specially engineered for it. Likewise, the X-Ray optics will be custom-built, where CAST used an optics system from old X-Ray satellite missions [34]. Using custom components means that they can be optimized for the application at hand, which will lead to a better performance of the experiment compared to its predecessors [35].

If IAXO is successful, it will surpass the CAST limit by more than one order of magnitude, as shown in Figure 7. It will be sensitive to part of the QCD axion regime and in places even be more sensitive than astrophysical limits. The figure also shows the projected sensitivity for BabyIAXO, the IAXO prototype experiment currently in development.

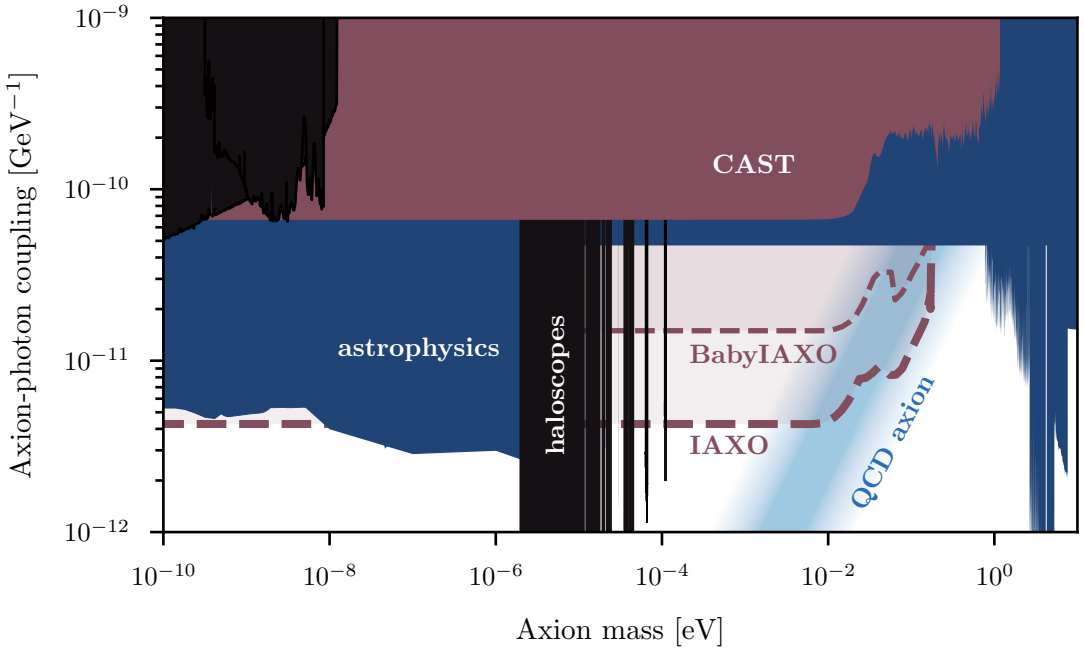

Figure 7: **Projected IAXO sensitivity**
Projected sensitivity to the axion-photon coupling $g_{a\gamma}$ for IAXO and BabyIAXO. They both aim to surpass the limits set by the previous axion helioscope CAST and cover part of the QCD axion band. Data taken from [22].

2.2. BabyIAXO

The first step towards IAXO is the construction of a smaller-scale prototype called BabyIAXO, shown in Figure 8. It will serve as a developing and testing site for the technologies of IAXO, while also being a fully-fledged helioscope that will take real physics data covering new parameter space [36]. The current IAXO design will be further improved with the experience and discoveries made during the BabyIAXO operation. The prototype will be built at DESY in Hamburg, in the south hall of the former HERA accelerator. All subsystems are currently in development.

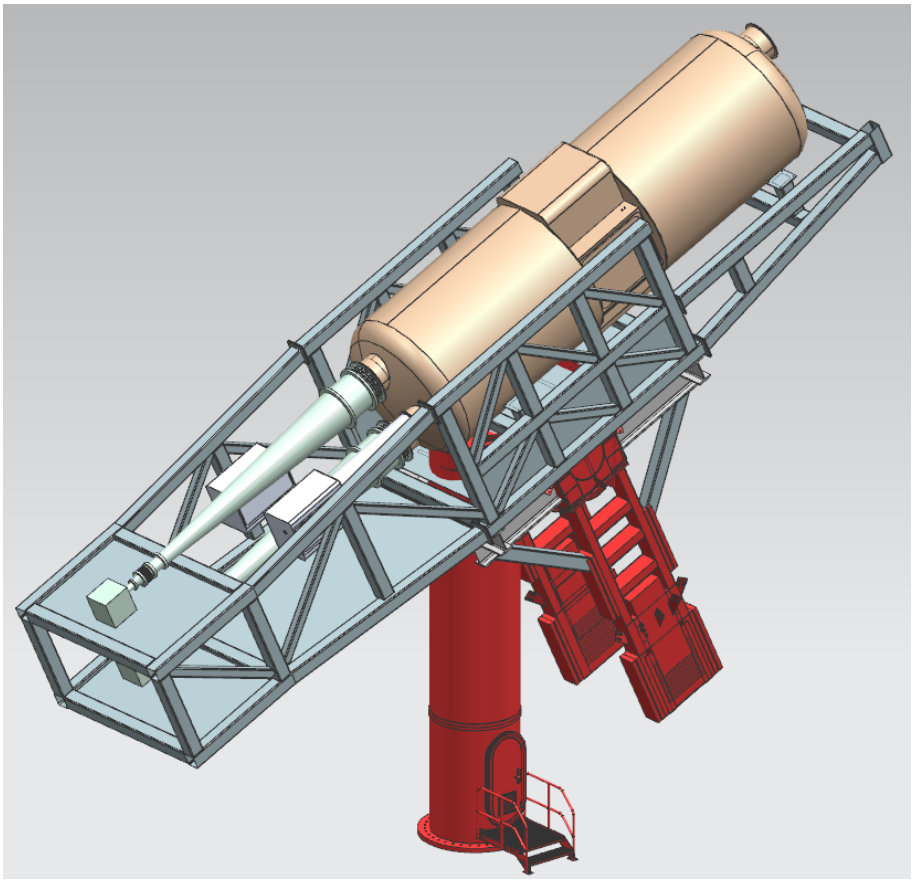

Figure 8: **Conceptual sketch of BabyIAXO**
Conceptual design of the BabyIAXO experiment. The magnet in the big beige tube is 10 m long, half as long as the one planned for IAXO. Instead of eight bores, it has two with 70 cm diameter, equipped with one X-Ray optics line and detector each. The helioscope sits on a telescope drive system to track the Sun.

The figure of merit of a helioscope's magnet is defined as $f_M = B^2 L^2 A$, where B is the magnetic field and L and A are the length and combined cross-section area of the bore holes, respectively. This figure indicates the strength of the axion signal, since Primakoff conversion is more likely for a stronger magnetic field and longer path through said field while a larger cross-section increases the total number of axions entering the magnet [37]. The magnet of BabyIAXO will be the largest improvement over CAST, being custom-made for the experiment rather than recycled. While the magnetic field of $B \approx 2\,\mathrm{T}$ will be weaker than the 10 T CAST magnet, the bore cross-sections will be much larger with a total $0.77\,\mathrm{m}^2$. CAST had only $0.003\,\mathrm{m}^2$. Even

with a weaker magnetic field, this increase in area will lead to a tenfold improvement of the BabyIAXO magnet's figure of merit over CAST [36].

Comparing other subsystems to CAST is less straightforward, since the old experiment used many different components during its runtime, sometimes simultaneously. BabyIAXO will follow the Sun for 12 hours a day just as IAXO will, requiring a much different drive system, frame, and Sun-tracking system than CAST. Two different X-Ray optics systems are currently in development, one custom-made and one recycled from a satellite mission. They face the challenge of having to focus the signal from a much larger area onto the detectors. For the detectors themselves, there are several groups working on different technologies to find the detector that is best suited for BabyIAXO [36].

2.3. Detector Challenge

The signal a helioscope is looking for is exactly the Primakoff spectrum in Figure 4, since the photons converted from solar axions follow the same distribution. This means that a helioscope detector needs to be sensitive to X-Rays in the single digit keV range. Ideally, it should have an energy threshold below 1 keV, so it could also see a large part of the ABC spectrum shown in Figure 4. To identify the different peaks in the ABC spectrum also requires a good energy resolution. The Primakoff spectrum has its peak around 3 keV and contains no fine features that require great energy resolution.

The main challenge in developing a detector for BabyIAXO is the high sensitivity the experiment wants to achieve. At the axion-photon coupling of almost $10^{-11}\,\mathrm{GeV}^{-1}$ that BabyIAXO is aiming for, the signal amounts to a handful of counts per year. To not lose any of those few counts, the detectors need to have a very high detection efficiency in the energy range of the signal. The background also needs to be kept as low as possible, to not drown out the small signal. Usually, experiments looking for such rare events are built deep underground, to shield them against cosmic background. But BabyIAXO does not enjoy this luxury since the size and movement of a helioscope limit the places where it can be built. The site of the experiment, the HERA south hall, offers only limited protection from cosmic particles. Even so, the background goal of BabyIAXO is $10^{-7}\,\mathrm{cts}/(\mathrm{cm}^2\,\mathrm{s}\,\mathrm{keV})$. The detector groups have to figure out a way to achieve such a low background in an essentially above-ground setting. Four main detector technologies are currently in development.

Micromegas

Micromegas stands for Micromesh Gaseous Structure and is a type of gaseous time projection chamber. A thin entrance window allows ionizing particles to enter the gas volume, where they produce free charges. On the opposite side of the gas chamber is the readout electrode, above which, at a distance of 50 µm, sits a wire mesh. The strong electric field between the wire mesh and readout cathode accelerates the charges towards the cathode where they produce a signal. Micromegas detectors were already used in CAST and achieved a background of $10^{-6}\,\mathrm{cts}/(\mathrm{cm}^2\,\mathrm{s}\,\mathrm{keV})$, the lowest of all CAST detectors [38]. More recent studies showed a background of $8.8 \times 10^{-7}\,\mathrm{cts}/(\mathrm{cm}^2\,\mathrm{s}\,\mathrm{keV})$ at ground level, with an efficiency around 50 % in the region 2 keV to 7 keV [39]. The low efficiency comes from the analysis cuts that were performed to eliminate background events.

Gridpix

The Gridpix detector is an evolution of the Micromegas, where a densely pixelated readout chip is placed under the wire mesh to read out each individual hole [40]. This adaptation allows for single electron detection and excellent spatial resolution with effectively no deadtime. A Gridpix detector was also installed in CAST, achieving

a background of a few $10^{-5}\,\mathrm{cts}/(\mathrm{cm}^2\,\mathrm{s}\,\mathrm{keV})$ above 2 keV [41]. The Gridpix group is currently working to improve its detectors and is looking to start background measurements with an improved design in the near future.

MMC

MMC stands for Metallic Magnetic Calorimeter. These detectors are operated at mK temperatures and consist of a sensitive volume thermally coupled to a paramagnetic temperature sensor in a static magnetic field. A particle interacting in the sensitive volume creates a slight increase in temperature that changes the magnetization of the temperature sensor. This change in magnetization in turn creates a magnetic flux differential that induces an electric signal in a superconducting pickup coil. MMCs are known to have excellent energy resolution of single eV and detection efficiency of near 100% across a wide range of energies [42]. The energy resolution means that MMCs are especially good at detailed spectroscopy, to unveil the finer features of the axion spectrum and learn about the underlying theory. First background measurements of an MMC test setup for IAXO showed a background of the order of $10^{-4}\,\mathrm{cts}/(\mathrm{cm}^2\,\mathrm{s}\,\mathrm{keV})$, which could be improved with additional shielding [43].

SDD

Silicon Drift Detectors, short SDDs, are a type of semiconductor detector. A commercial SDD was used in one CAST run looking for solar chameleons, a dark energy candidate [44]. Since they are central to this thesis, SDDs and their application in BabyIAXO are discussed in detail in the following section.

2.4. TRISTAN SDD for IAXO

The KATRIN experiment is measuring the absolute neutrino mass by looking at the endpoint energy of the electron spectrum from tritium beta decay [45]. A future upgrade of KATRIN aims to shift the focus of the experiment to the whole electron spectrum to look for a signature from keV-scale sterile neutrinos. For this, a new detector had to be developed, the so-called TRISTAN detector [46]. It is an SDD, a versatile type of detector that can be used in many different experiments, including IAXO.

TRISTAN SDD for IAXO (TAXO) is the name the SDD detector group of IAXO gave their project, since they started using detectors from the TRISTAN production to investigate their use for BabyIAXO. These SDDs have the potential to meet all the requirements outlined in the previous section.

2.4.1. Silicon Drift Detectors

Semiconductors are materials wherein the energy gap between the valence and conduction band is small, so electrons can easily become free charge carriers, for example through thermal excitation. Semiconductors can be modified via doping, which is purposeful insertion of foreign atoms. There are two types of doping. N-type doping inserts elements with more valence electrons than needed for bonding into the crystal lattice, effectively creating free electrons as negative charge carriers. P-type doping is the opposite, inserting an element with fewer valence electrons and creating electron holes as positive charge carriers [47].

When a p-doped and n-doped material come into contact, free charge carriers diffuse across the junction and recombine. The immobile ions stay behind, which creates a local charge distribution and with it an electric field countering the flow of charge carriers and preventing further diffusion. The area around the junction without any free charge carriers is called the depletion region. By applying a reverse bias, the depletion region can be enlarged. Free charge carriers that are created here drift towards the anode and cathode, following the electric field. Figure 9 illustrates this principle. By collecting and measuring these charges one has effectively created a detector for ionizing radiation [47, 48].

Silicon drift detectors (SDDs) are such detectors, made from the semiconductor silicon, utilizing a technique called sideways depletion [49]. Instead of the anode and cathode being of the same size across from each other like in Figure 9, the electric field is shaped by a voltage gradient so that the anode can be much smaller than the cathode. Figure 10 shows a schematic of an SDD employing this technique. The small readout anode compared to the dimensions of the detector allows for a small capacitance against a large active volume, leading to an improved noise performance and with that a better energy resolution [50].

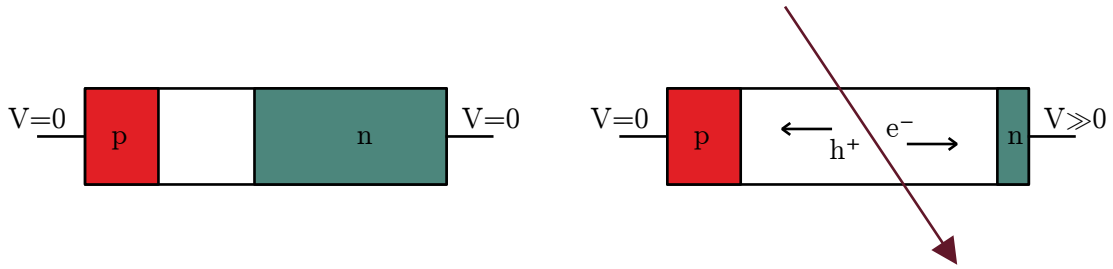

Figure 9: **Semiconductor p-n junction**
Left: A p-n junction in equilibrium, with no external field. Between the red p-doped and the green n-doped region, a white depletion region forms. *Right*: The same p-n junction, now with a reverse bias applied. The negative charge carriers in the n-region wander towards the anode, which creates a much larger depletion region in the center. An ionizing particle can create free charges in this area. Due to the electric field, holes drift towards the p-doped region and electrons drift towards the n-doped region.

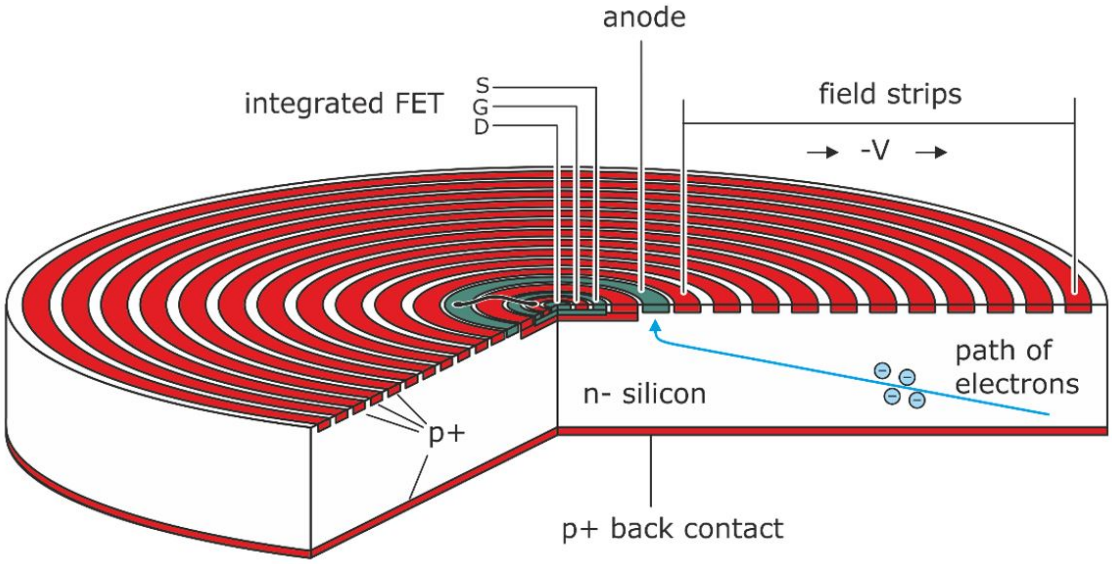

Figure 10: **SDD working principle**
The bulk of the detector is n-doped silicon, with the p-doped areas marked in red and connected to negative biases. The field strips on the top are increasingly negatively biased towards the outer rings, which in combination with the back contact creates an electric field that guides negative charges towards the anode ring and leads to the depletion of the white volume. The integrated field-effect transistor (FET) amplifies the signal. Adapted from [51].

Where data exists, the SDD performs well on all criteria for a BabyIAXO detector. Measurements showed an energy resolution of 139 eV at 6 keV when cooled to −30 °C [46]. The detector has an energy threshold of 200 eV when cooled, 300 eV at room temperature [52], which means that it is sensitive to the peak of the ABC spectrum. Additionally, it does not need an entrance window and has only a thin deadlayer [53], which means that low-energy particles can enter the sensitive detector volume quite easily. The detection efficiency of the TRISTAN SDD has not been measured so far. However, since silicon is such a commonly used semiconductor, its properties are well understood. Both calculations [54] and TAXO-internal simula-

tions [55] show that SDDs have a 99% absorption efficiency for X-Ray gammas of the Primakoff spectrum, and 92% for the ABC spectrum. Measurements to verify the detection efficiency are currently in preparation. The final, and arguably most critical, requirement is the low background. Silicon, which makes up the bulk of an SDD, can be made radiopure. Placing the electronics at a distance from the sensitive detector volume reduces the background contributed by electronic components, at the potential cost of worsening the noise performance. For these reasons, SDDs have great potential as low-background detectors. However, since they have never been used in low-background experiments before, this has never been shown in practice. That is why the TAXO group is trying to demonstrate a low-background SDD with their own setup.

2.4.2. TAXO Demonstrator

A detector for BabyIAXO needs to show a background level of $10^{-7}\,\mathrm{cts/(cm^2\,s\,keV)}$. For this purpose, the TAXO group has devised a setup called the TAXO demonstrator. At the center of the demonstrator is the SDD, currently a prototype from the TRISTAN production with seven hexagonal pixels, shown in Figure 11. The same figure also shows the custom low-background printed circuit board (PCB) on which the detector chip sits. Both the detector itself and the PCB are continuously improved upon and replaced in an iterative process.

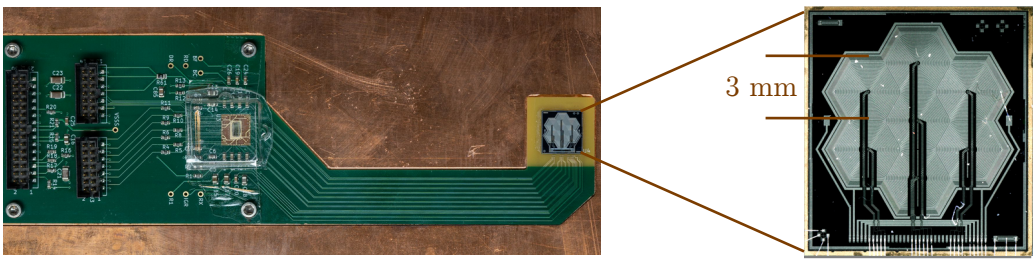

Figure 11: **TAXO PCB and seven-pixel SDD**
The PCB is designed specifically for a low background, with the detector at a distance and shielded from the electronics. The detector has seven hexagonal pixels with 3 mm diameter.

2.4.2.1 Shielding

The shielding of the demonstrator consists of several different layers, shown in Figure 12. Lighter and more radiopure materials are closer to the detector to absorb emissions from the outer layers of shielding. The outer layers in turn are the primary shield against external background. The bulk of the shielding consists of lead. Lead is well-established as a radiation shield due to its high density and atomic number. It is especially effective at reducing gammas; however, it also contains radioactive isotopes. For example, ^{210}Pb undergoes beta decay, which leads to the emission of 10 keV and 47 keV gammas. To shield against those emissions, the detector is

surrounded by copper. Copper, however, can emit X-ray fluorescence. It has two fluorescence lines at 8 keV and 9 keV. To shield against these lines, the SDD is sandwiched between two silicon plates.

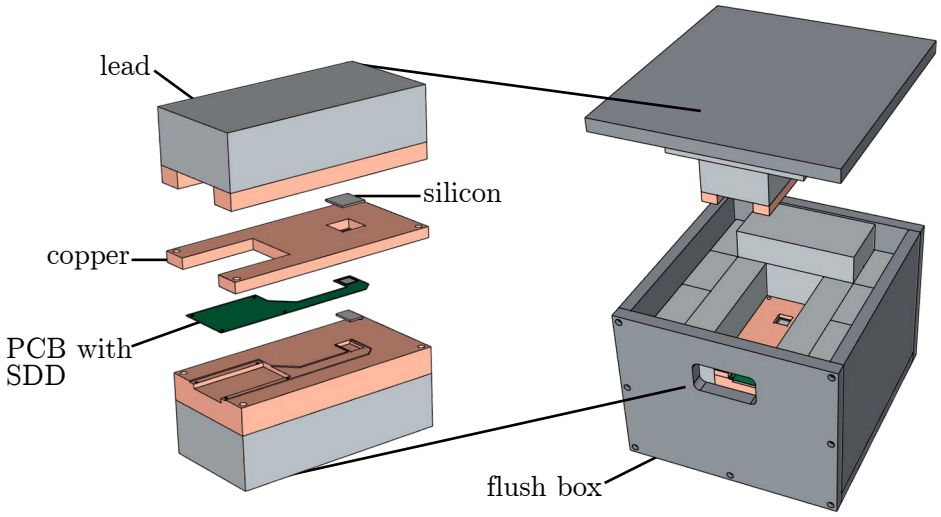

Figure 12: **TAXO demonstrator shielding**
Right: The nitrogen flushed box filled with lead bricks surrounding the centermost part of the demonstrator. *Left*: An exploded view of the inner shielding. The PCB with the detector fits inside a copper enclosure with the same dimensions as a lead brick to fit seamlessly into the lead castle. Above and below the SDD are two silicon plates.

The TAXO group is planning to add borated polyethylene (PE(Bo)) to the demonstrator shielding to reduce the background produced by neutrons. PE(Bo) is a neutron shield that functions by first slowing down free neutrons and then capturing those low-energy neutrons. Polyethylene is the neutron moderator since it contains a lot of hydrogen. Because they have similar mass, neutrons lose a large fraction of their kinetic energy when scattering with hydrogen atoms. Boron is the neutron captor. It reacts with free neutrons in the following way [56]:

$$\begin{aligned} {}^{10}\mathrm{B} + \mathrm{n} \quad & \longrightarrow {}^{4}\mathrm{He} + {}^{7}\mathrm{Li} + 2.79\,\mathrm{MeV} \qquad (6\,\%) \\ & \longrightarrow {}^{4}\mathrm{He} + {}^{7}\mathrm{Li}^{*} + 2.31\,\mathrm{MeV} \qquad (94\,\%) \\ & \qquad\quad \hookrightarrow {}^{7}\mathrm{Li} + \gamma + 0.48\,\mathrm{MeV} \end{aligned} \tag{7}$$

This reaction is notable since it is an inelastic process that does not produce secondary neutrons. It effectively removes free neutrons from the system, preventing them from producing background signals in the detector. However, the 480 keV gamma emitted by the excited lithium atom is a potential source of background if not shielded against properly. The reaction is more probable at lower kinetic energies, which is why boron needs to be paired with a neutron moderator to reduce a significant amount of neutron flux. How exactly the addition of borated polyethylene affects the TAXO demonstrator is part of my investigations when simulating the setup in Chapter 3.

2.4.2.2 Twin Setups

There are two instances of the TAXO demonstrator at different laboratories. One is deep underground, one at ground-level. The idea behind these twin setups is that they allow the investigation of different types of background. The underground lab is shielded from cosmic particles so that the cosmic background is negligible. Taking data here gives insights into the intrinsic background of the setup, produced by impurities in the various materials. Of course, BabyIAXO will not be deep underground, so the cosmic background also needs to be accounted for. This is why a second setup at ground level is necessary. Comparing data taken with this setup to data taken with the underground setup reveals the contribution of cosmic particles to the measured background.

The underground setup is at Laboratorio Subterráneo de Canfranc (LSC), a laboratory in the Spanish Pyrenees with 2400 m water equivalent overburden. The TAXO demonstrator was installed there in 2022 and took data for several months. The measurement yielded a background level about one order of magnitude higher than anticipated, which was traced back to the PCB material that turned out to be less radiopure than expected. This revelation prompted the development of a new PCB design, where the area around the SDD is made of radiopure silicon, to reduce the background from radioactive decays in the material. The demonstrator at LSC will be upgraded with this new PCB design soon for another run of data taking. For more details on the past LSC measurement campaign and the TAXO demonstrator there, see [57].

The above-ground setup is in a laboratory at Technische Universität München (TUM). In the future, this demonstrator could also be moved to a shallow underground laboratory at TUM or directly to the site of the BabyIAXO experiment at DESY. This setup is a copy of the one at LSC, equipped with an additional muon veto, and will take data both with and without PE(Bo) as an extra layer of shielding. The full setting up and testing of the muon veto is one topic of this thesis, covered in Chapter 4. The other topic is Monte Carlo simulations of this setup to investigate the expected cosmic background, which are covered in the following chapter.

3. Cosmic Background Simulations

Cosmic shower particles are an inevitable source of background in IAXO. TAXO aims to reduce this background through a combination of active and passive shielding. Developing an effective shielding concept requires a thorough understanding of the interactions of cosmic particles with different materials, for which GEANT4 Monte Carlo simulations are useful. Previous TAXO simulations only covered cosmic muons. This thesis is the first time the full cosmic particle spectrum has been implemented in a background simulation for TAXO.

Section 3.1 gives a brief introduction to cosmic shower particles before explaining how they are generated in the simulations. Section 3.2 covers the details of the cosmic background simulations themselves. Section 3.3 gives the simulation results with a detailed breakdown of the background contributions from different cosmic particles and their interactions with the shielding materials.

3.1. Cosmic Particle Generation

Previous cosmic background simulations for TAXO only considered cosmic muons as primaries [55]. Studies done by other detector groups suggest that other cosmic particles, mainly neutrons, could also significantly contribute to the background [58]. Studying this requires simulations that implement the entire cosmic particle flux.

3.1.1. Cosmic Showers

Cosmic rays are high-energy particles of cosmic origin. They are mainly protons, but also contain other charged nuclei, electrons, and non-charged particles. When they enter the atmosphere, they create a cascade of secondaries known as cosmic showers. Rather than the primary cosmic rays, it is particles from these showers that reach the earth's surface [59].

The most abundant cosmic shower particles at sea level, aside from the barely-interacting neutrinos, are muons [4]. They are produced mainly in pion and kaon decays. Their highly relativistic energies allow them to easily pass through thick layers of material despite losing energy through interactions. For this reason, they are often called the 'hard' or 'penetrating' shower component. The muon energy loss due to ionization is roughly 2 MeV/cm, though at kinetic energies above 2 GeV the energy loss is dominated by other effects such as nuclear interactions and increases linearly [60]. Effectively shielding against high-energy cosmic muons is only feasible by going deep underground. The muon flux at sea level is roughly one particle per cm^2 and minute. Deep underground at a level equivalent to 10 km of water, it is reduced by six orders of magnitude [61].

Other particles are less common at sea level and have lower energies than muons. Neutrons and protons are mainly created in hadronic showers. Electrons and gammas are produced in electromagnetic showers or pion decays [61]. This electromagnetic component of cosmic showers is often called the 'soft' component, since it can be stopped by a few cm of lead [62]. Pions can also reach the surface, but they are the least common particle type at sea level [61].

The direction of cosmic shower particles is isotropic in the polar angle. Their azimuth angle roughly follows a cosine squared distribution, i.e., $\cos^2(\theta)$. This means that most particles come from above, with the flux from the sides decreasing towards zero at an angle of $\theta = 90°$ [61].

3.1.2. Cosmic Ray Particle Library

The Cosmic-Ray Particle Library (CRY) is a simulation toolkit developed by the Lawrence Liverpool National Laboratory [63]. It contains data tables from previous Monte Carlo simulations of primary cosmic rays interacting with the fully modelled atmosphere. From these it generates correlated cosmic shower particles using probability calculations. Since it does not run full atmospheric simulations itself, CRY is a fast and efficient way to simulate cosmic particle data.

The user can edit the CRY interface to modify format and content of the program's output. The output can be printed to the terminal or saved as a file and can contain several parameters, such as the particle type, location, incidence angle, information on timing, and correlations between particles. The user can also specify the elevation, latitude, and area on which to generate particles, as well as the types and total number of particles she wants. For parameters corresponding to the location of the TAXO demonstrator at TUM, CRY generates the particle flux shown in Figure 13. It covers muons above 1 MeV and neutrons even down to the thermal regime, as well as all other particle types at relevant energies. Lower-energy particles are not able to penetrate the shielding and create background events in the SDD.

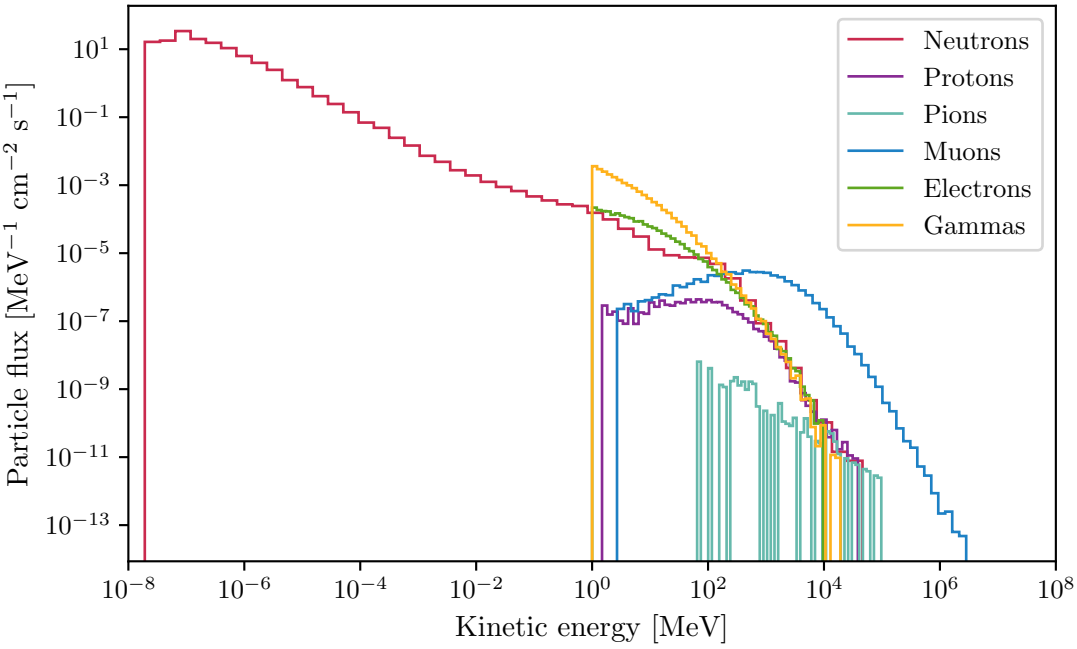

Figure 13: **CRY particle flux**
Full flux of each cosmic shower particle type generated with the CRY simulation toolkit. The input parameters of a latitude of 48° and elevation of 0 m match the location of the TAXO demonstrator at TUM. CRY only generates particles down to a low-energy cutoff. For most particles this is at or above 1 MeV, but neutrons are generated down to much lower energies. For the background simulations, only high-energy particles are of interest since they can penetrate the shielding.

By default, CRY generates its particles on a square, flat plane. Using the output as is for background simulations would mean generating primaries on a flat surface above the setup. There would be no flux from the sides, and a portion of the flux at the position of the setup would be lost. Instead, generating particles on a half-sphere above the setup automatically induces a flux from the sides while maintaining the full flux through the center of the setup. This requires the CRY output format to be converted to this geometry as shown in Figure 14. I implemented this conversion in the CRY interface code so that the new coordinates are written directly into the output file.

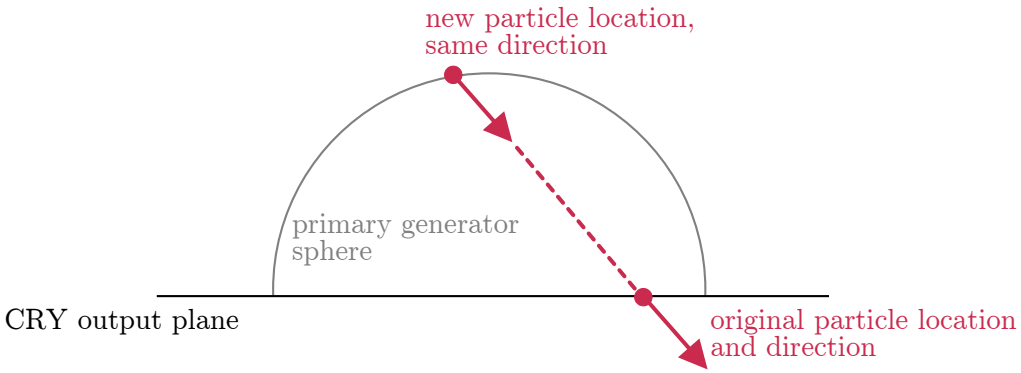

Figure 14: **Sketch of the CRY output geometry conversion**
The simulation toolkit CRY generates particles on a flat output plane with an incidence angle and position coordinates. In the cosmic background simulations, primaries should start from a half-sphere above the experimental setup, the primary generator sphere. The conversion traces back the particle track along its incidence angle and determines the point where it crosses the sphere. These are the new particle coordinates. Particles whose track never crosses the sphere are discarded.

It should be noted that some flux from the sides is still lost and could be recovered by increasing the size of the plane for the initial particle generation. Nevertheless, this conversion retains a larger fraction of the flux from all sides with a smaller plane compared to the flat plane without a conversion. Since the angular distribution of cosmic shower particles follows a $\cos^2(\theta)$ distribution, less than 1 % of the flux is lost when using a square plane with a side length of 10 m and converting it to a sphere with a radius of 3 m.

Some other adjustments to the native CRY code were the implementation of a new random number generation and changing the particle names to the same naming scheme used by GEANT4. With this modified CRY application, I generated output files that were directly used to simulate the cosmic background in TAXO.

3.2. Simulation

GEANT4, short for GEneration ANd Tracking, is a Monte Carlo simulation toolkit for the interactions between particles and matter [64]. I wrote a GEANT4 interface that can process the files generated by CRY to start primary particles. GEANT4 then simulates their passage through the implemented setups and their interactions with the various materials. It also tracks any secondary particles produced in these interactions in the same way.

3.2.1. Simulation Geometry

The simulated setup, sketched in Figure 15, is a simplified version of the real world TAXO demonstrator with spherical geometry. Different shielding materials are layered in an onion-like structure around the SDD in the center. The purpose of the Monte Carlo simulations is to study the general effect of various shielding materials on the cosmic background. Therefore, a more realistic geometry is not necessary.

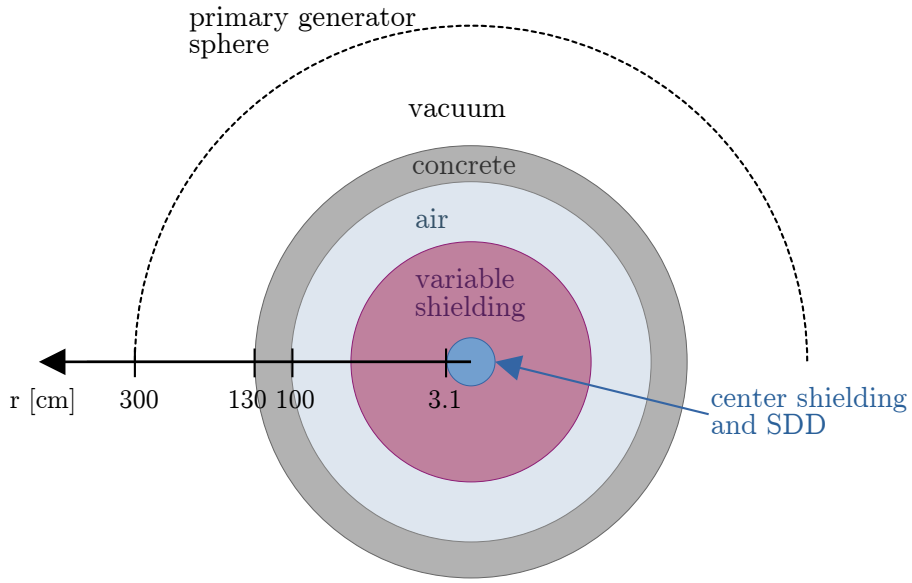

Figure 15: **Sketch of the setup implemented in the background simulations** The setup is centered around the SDD and inner shielding, followed by several variable shielding layers. The different simulated shielding concepts are shown in more detail in Figure 16. From the outer part of the variable shielding up to a radius of 100 cm, the space is filled with air, followed by a 30 cm-thick concrete layer. The generation of primary particles happens on a half sphere above the setup, at a radius of 300 cm.

The outer layers of the simulated geometry, concrete and air, represent the lab room the setup is situated in. The shielding in the center consists of 1 mm of silicon and 1 cm of copper, reflecting the innermost part of the TAXO demonstrator setup as it was shown in Figure 12. An SDD with an area of 10 cm^2 sits in the center. It has a larger surface area than the real detectors to collect higher statistics more efficiently.

There are four different shielding configurations, shown in Figure 16. The 'standard' configuration mimics the TUM demonstrator setup. At this setup, PE(Bo) can be added between the muon veto and lead shielding, same as in the 'outer PE(Bo)' configuration. In comparison, the 'inner PE(Bo)' configuration was implemented to investigate the impact of the order of materials on the background. Lastly, the 'multi-layer' configuration is inspired by the shielding of the Conus experiment [65] and was used to study the impact of multiple alternating layers.

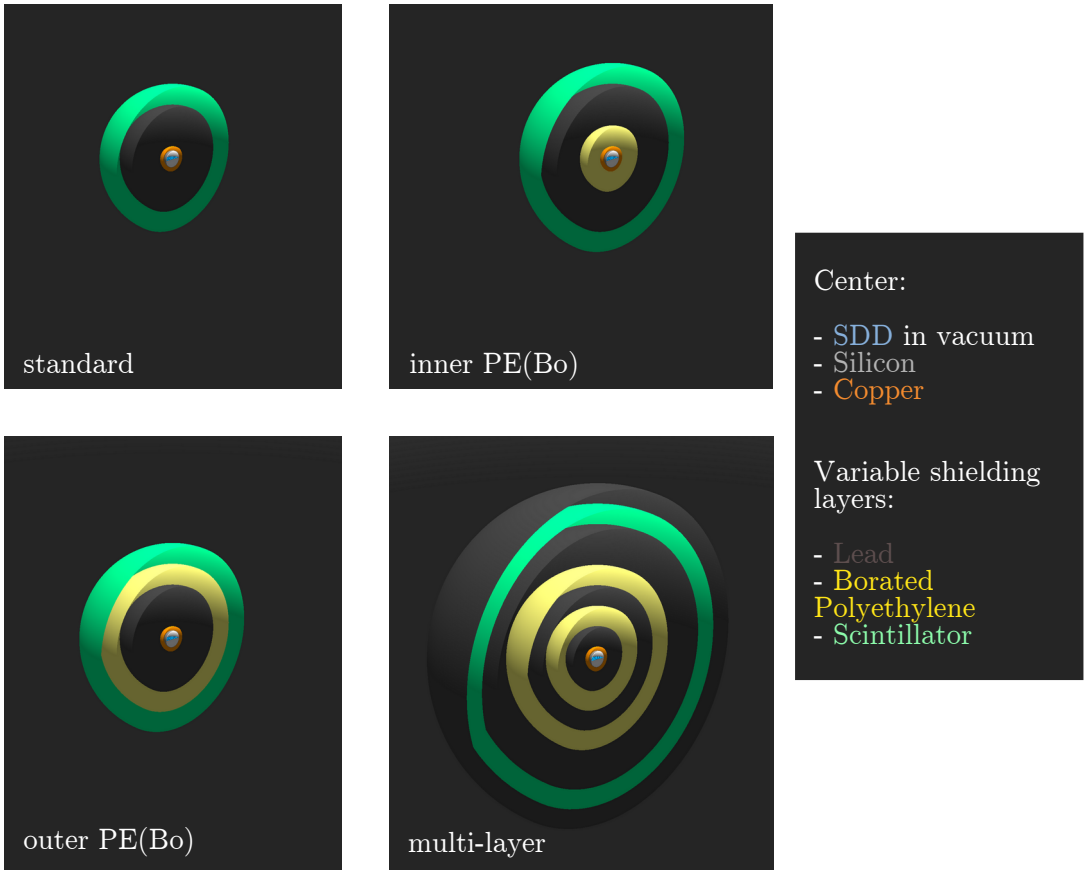

Figure 16: **Simulated shielding concepts**
Renderings of the four different shielding configurations of the background simulations. The central part — SDD, silicon, and copper — remains unchanged. The **standard** configuration adds one 10 cm layer of lead for shielding, and scintillator as a muon veto. The two following variations add a 5 cm layer of PE(Bo) as a neutron shield in different positions. The **inner PE(Bo)** configuration has this layer between the lead and copper, while **outer PE(Bo)** has it between the lead and scintillator. Finally, the **multi-layer** configuration has several alternating layers of lead and PE(Bo), with the scintillator also sandwiched between two layers of lead.

3.2.2. Observables

GEANT4 can generate a large volume of output data. Depending on the goal of the simulations, different observables must be written out. The goal of these simulations is to do a detailed investigation of the effect of different shielding concepts on the background, so I chose observables that support this analysis. The simulated energy deposition needed further corrections before being able to use it in the analysis.

3.2.2.1 Energy Deposition

In GEANT4, the user can declare volumes as sensitive detectors and store information if a hit, i.e., an energy deposition, is registered in this volume. The sensitive detectors in the TAXO simulations are the SDD and the scintillator. For each hit, the simulations store the particle type, process, location, time, and energy deposition.

The energy deposition given by GEANT4 corresponds to the total energy deposited in the detector by the incoming particle. When performing measurements with a real SDD however, the measured signal is only due to ionization. For electrons and gammas, this matches the simulated energy. Neutrons on the other hand undergo nuclear recoils that deposit a large fraction of their energy as phonon excitations. Only a small fraction of the energy corresponds to ionization and can be measured. The ratio of ionization energy of neutron, compared to the ionization energy of an electron of the same kinetic energy, is called the neutron quenching factor or ionization efficiency.

The energy transfer of atomic collisions in matter has been studied by Jens Lindhard [66]. His model also describes the ionization efficiency of neutrons in silicon, shown in Figure 17. I used this model to correct the energy deposition given by GEANT4 for neutrons. This way, the simulations better reflect measured data.

More recent studies show that reality deviates from the Lindhard model at low energies [68, 67]. Figure 17 shows that the model overestimates the ionization efficiency at energies below 5 keV. However, this has no impact on the TAXO simulations. The region of interest (ROI) of the past LSC TAXO demonstrator measurements was (2 to 10) keV, so the simulations cover the same range. This means that neutrons whose measured energy ends up below 2 keV do not play a role in the analysis. A neutron with a raw GEANT4 energy deposition of 5 keV is shifted to 1.25 keV by the Lindhard quenching factor, so the deviations between model and experiment at lower energies only affect neutrons that fall outside the ROI.

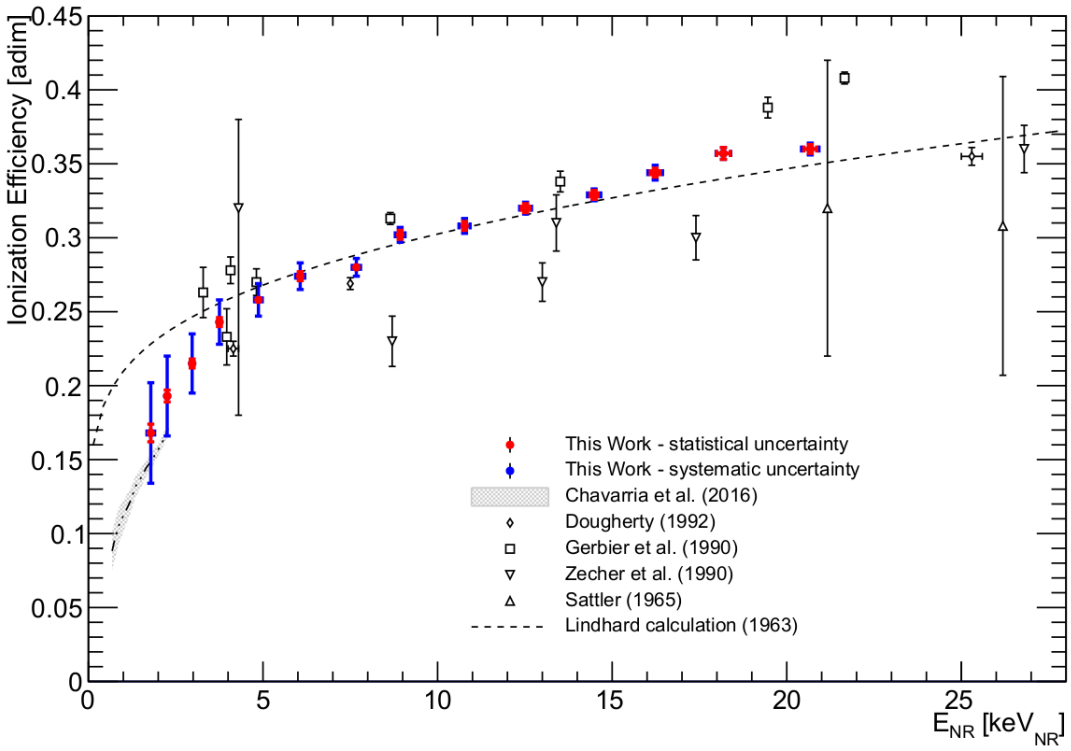

Figure 17: **Ionization efficiency of neutrons in silicon**
Ionization efficiency, also known as quenching factor, of neutrons in silicon, as a function of the full nuclear recoil energy. The plot compares measurement data (markers) and the theoretical model by Lindhard (dashed black line). Figure taken from [67].

3.2.2.2 Particle Tracking

The so-called stacking action is executed by GEANT4 whenever a new particle is created during a simulation run. The customized stacking action of the TAXO background simulations saves the energy, location, and type of the new particle, as well as the parent and process that created it, and stores this information in the output file. It can later be used to reconstruct the track of an event, from the primary all the way to the particle that created the detector hit.

During the analysis I first identified the events with an SDD signal that falls into the ROI of (2 to 10) keV. The scintillator serves as a muon veto like the one at the TUM demonstrator setup. Therefore, if the SDD hit coincided with an energy deposition in the scintillator above 3 MeV, the event was cut. What remains are the background events. For each of these, I used the stacking action data to reconstruct the full history that led to the SDD hit. This event history was then used to analyze the nature of the cosmic background events.

3.3. Results

For each of the four shielding concepts, I ran a simulation with 10 billion primaries. A primary has to pass through layers of concrete and air before reaching the shielding. In these outer layers, new particles can be created in a variety of ways. The particle that enters the shielding is not necessarily the same one that originated on the generator sphere. Moving forward, I will refer to the particles that enter the shielding as 'incident'. They will be the focus of this analysis, rather than the actual primaries. Plots showing the tracks of all the background events are in Appendix A.

3.3.1. Background Contributions

Different incident particles have different contributions to the background index, as shown in Figure 18. How they create background and how they are affected by shielding is discussed in more detail in the following sections for gammas, muons, and neutrons, respectively. The events labeled as 'others' are not discussed in depth. They are mainly incident protons and few pions that in all cases interact in lead and produce neutrons. They only play a role in the standard configuration. These events are eliminated by three out of the four investigated shielding configurations.

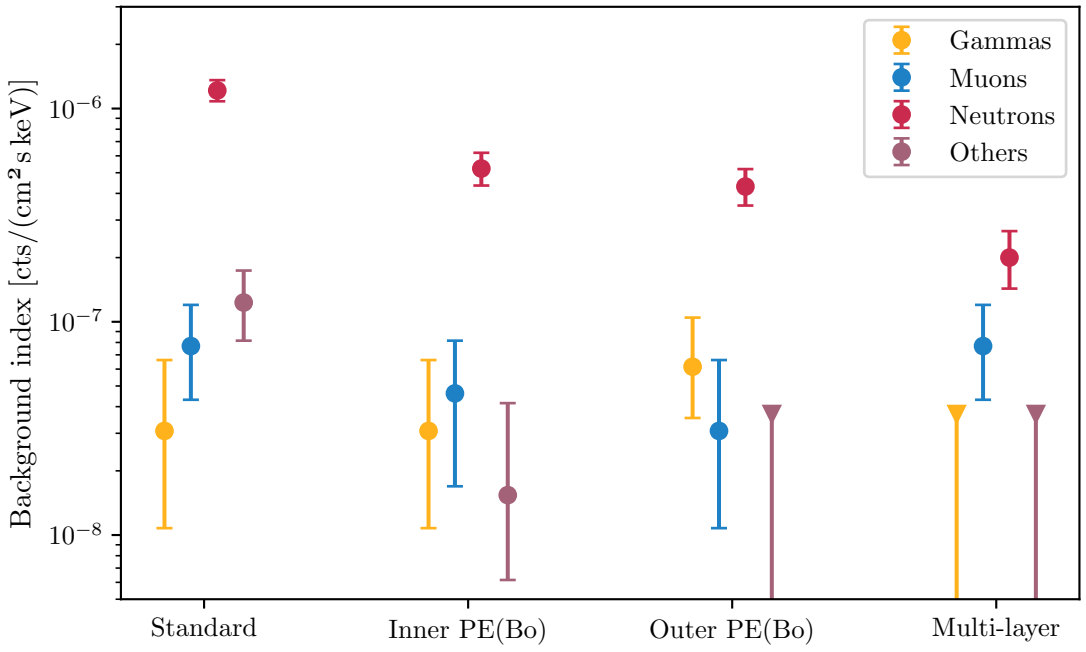

Figure 18: **Background contribution of different incident particles**
Background index produced in the four simulated shielding configurations by gammas, muons, neutrons, and other particles. The latter category contains protons and pions. Neutrons contribute by far the most to the background but are also most clearly affected by varying the shielding. The standard error bars represent 1 σ uncertainty, while the inverted triangles mark 90% exclusion limits.

3.3.1.1 Gammas

Gammas contribute less than $10^{-7}\,\mathrm{cts}/(\mathrm{cm}^2\,\mathrm{s}\,\mathrm{keV})$ to the background across all shielding configurations. They are part of the soft component of cosmic rays, which means that they cannot penetrate thick layers of dense material such as rock or lead [62]. Indeed, there is no background induced by gammas in the multi-layer concept. While at these small numbers the exclusion limit overlaps with the few counts in other shielding setups, the multi-layer concept is the only one that increases the amount of lead shielding and therefore increases its effectiveness against gammas.

Across all simulations, there were only two gammas that passed through the full shielding before hitting the SDD, both with energies above 100 MeV. More common is the detection of particles that came from a long series of interactions, started by incident gammas. As an example, gammas induce pair production, creating an electron-positron-pair near a nucleus. Resulting electrons emit bremsstrahlung, which can in turn induce pair production. Photonuclear reactions produce nucleons. All these interactions happen in lead. If there are more layers of lead shielding, these interactions happen mostly in outer layers, and the resulting particles have a higher likelihood of being stopped by inner layers. Additionally, gammas passing through more lead lose more energy in interactions, reducing the number of gammas that reach the SDD. The simulations clearly show why lead is so effective at shielding against gammas.

3.3.1.2 Muons

The muon veto effectively rejects direct muon hits. However, there are two ways in which muons can still cause background: They can decay, with the decay products causing a signal in the SDD. Or they can interact with the shielding material via scattering or muon capture, producing secondaries that lead to an SDD event. In both cases, there is a significant time difference between the scintillator hit and the SDD hit, which means that the SDD event cannot be identified with a muon veto event and is not removed by the muon veto cut.

Muons, like gammas, contribute less than $10^{-7}\,\mathrm{cts}/(\mathrm{cm}^2\,\mathrm{s}\,\mathrm{keV})$ to the background across all shielding configurations. There is no indication that their events are reduced in the multi-layer setup. As explained in Section 3.1.1, muons are the hard component of cosmic showers, which means the only way to effectively reduce the muon flux is by going deep underground. While the site of BabyIAXO, the HERA south hall, is not deep underground, it does have more overburden than the 30 cm concrete wall implemented in the simulation. Measurements of the muon flux in the HERA south hall indicate that the muon flux is reduced by half compared to the surface [69]. At a smaller scale, simply changing the shielding of the setup does not seem to reduce the muon-induced background.

3.3.1.3 Neutrons

Neutrons contribute by far the most to the cosmic background, but in turn appear to be the most affected by different shielding concepts. The inelastic neutron cross sections in Figure 19 can help explain this relationship. In lead and copper, inelastic events include radiative neutron capture and inelastic scattering. In boron, the inelastic process is the one described in Equation (7). The inelastic process in boron effectively removes free neutrons from the system, while inelastic scattering in lead and copper can produce many more neutrons. Therefore, it is preferable for neutrons to scatter in boron. I will refer back to this plot when discussing the background contribution of neutrons in more depth.

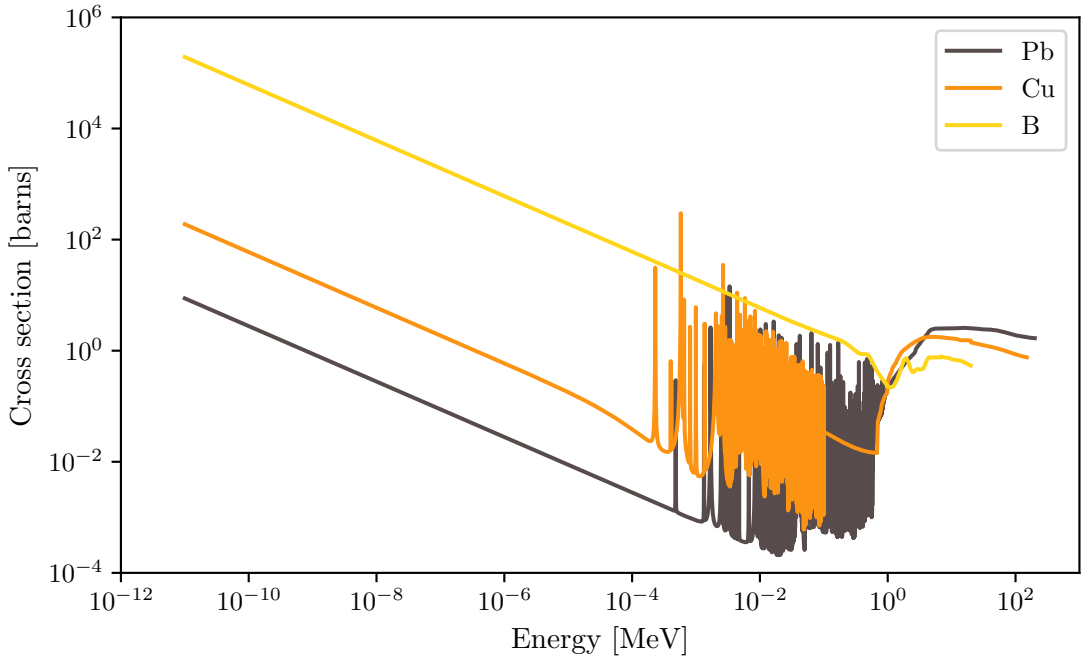

Figure 19: **Inelastic neutron cross sections**
Inelastic neutron cross section for three materials used in the simulated shielding configurations: Lead, copper, and boron. Boron has a much higher cross section than the other two materials up to a neutron energy of around 1 MeV. Copper has a higher cross section than lead for low energies, while at higher energies lead has the largest cross section. Data retrieved from [70].

To further understand the impact of different shielding materials, I divided the neutron-induced background events into categories based on the type of interaction that caused the SDD signal, shown in Figure 20. In the standard configuration, radiative neutron capture in copper is the dominant effect. The copper layer is close to the SDD, with only a thin layer of silicon in between. Any particles produced here can cause a signal easily. The impact of neutron capture in copper is reduced by adding PE(Bo) and remains at a low level for all other shielding concepts. This is explained by PE(Bo) having a much higher inelastic neutron cross section than copper for energies below 1 MeV. PE(Bo) captures most neutrons before they can reach the copper layer and produce a background signal.

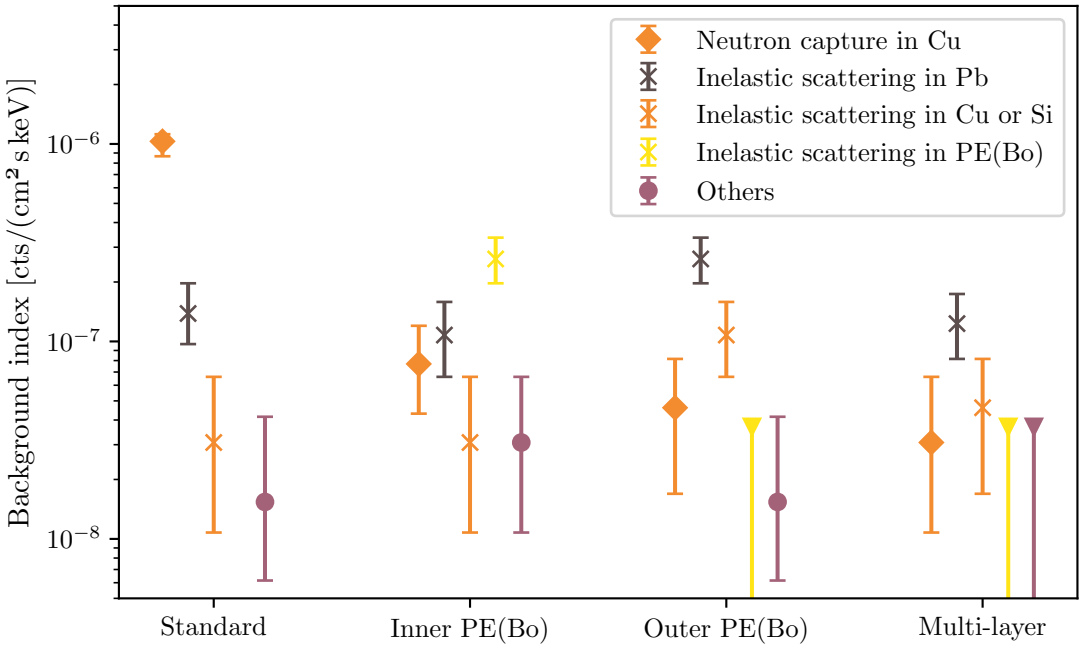

Figure 20: **Different neutron processes' background contribution**
Neutron-induced background index, categorized by the last neutron interaction before the SDD hit. The standard error bars represent $1\,\sigma$ uncertainty, the inverted triangles mark 90% exclusion limits.

Placing the PE(Bo) between the copper and lead layer in the inner PE(Bo) configuration, however, introduces a new source of background: Inelastic neutron scattering in PE(Bo). This background is entirely from the 0.48 MeV gamma emitted by the excited lithium in Equation (7). A single layer of lead between the PE(Bo) and SDD, like in the outer PE(Bo) and multi-layer configurations, shields against this gamma and effectively reduces this type of background to zero.

The third shielding concept, outer PE(Bo), has yet another effect as the dominant background contribution: Inelastic scattering in lead. Inelastic scattering in copper and silicon is the second most dominant process. Both processes have a higher background contribution than in the inner PE(Bo) configuration since neutrons that were not captured in the PE(Bo) layer can proliferate in lead. Without an inner layer of PE(Bo) to reduce those neutrons, they are more likely to cause a signal in the SDD. However, inelastic scattering in lead, copper, and silicon also produces a larger background in the outer PE(Bo) configuration than in the standard one. This effect is harder to understand. It might be that the neutron moderation of polyethylene shifts neutrons to a lower energy range where inelastic scattering in lead and copper is more likely. As shown by the cross sections in Figure 19, the likelihood for inelastic scattering increases towards lower energies for both copper and lead at energies below 1 keV, so this is a possible explanation.

Even though the reason for this increase in inelastic scattering in the outer PE(Bo) configuration is not clear, the multi-layer configuration decreases it again. There

are also none of the events labeled as 'others' in Figure 20. Those are mainly neutrons that pass all shielding layers and scatter directly in the SDD and already play a minor role in previous shieldings. The combination of many layers of lead and additional PE(Bo), with lead in-between, seems to be effective at reducing all types of neutron events. Inelastic scattering in lead is still the largest contributor to background.

Just like with muons, these simulation results are for the cosmic neutron flux at sea level inside a regular room. The background produced by neutrons at HERA south hall might be different. Up to now, there have been neither conclusive measurements nor simulations of the neutron flux in HERA south hall. It is likely that the neutron flux would be reduced in the hall compared to the TAXO lab at TUM due to the higher overburden, but actual measurements and simulations to verify this remain to be carried out.

3.3.2. Background Index

The contributions of all particle types have been combined into a singular background index, shown in Figure 21. It visualizes the cumulative effect of the different shielding configurations. It also includes the background index before applying the muon veto cut, showing that the muon veto alone can reduce the background by up to one order of magnitude. Adding a layer of PE(Bo) leads to a background reduction of 60 % compared to the standard configuration. The multi-layer setup can further halve the background.

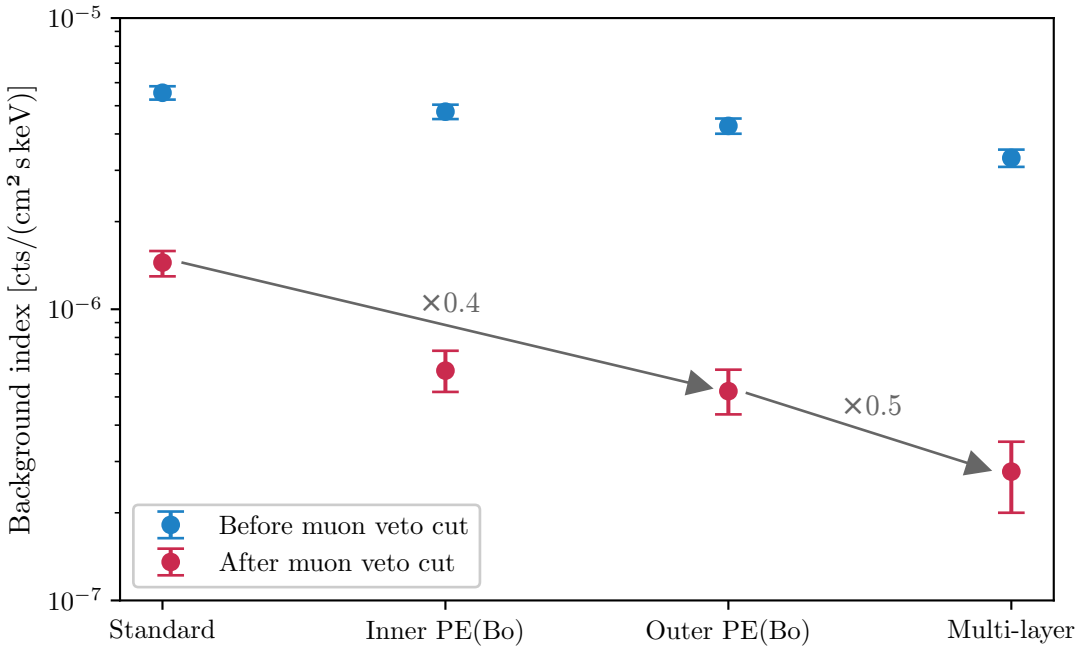

Figure 21: **Simulated background index**
Total background index from the simulations, combining the background contributions of all incident particles, before and after applying the muon veto cut. The error bars mark 1 σ uncertainty.

The best shielding concept of the simulations, multi-layer, has a total background index of $(2.8 \pm 0.7) \times 10^{-7}\,\mathrm{cts}/(\mathrm{cm}^2\,\mathrm{s}\,\mathrm{keV})$, which is still above the BabyIAXO target of $1 \times 10^{-7}\,\mathrm{cts}/(\mathrm{cm}^2\,\mathrm{s}\,\mathrm{keV})$. These simulations reflect the cosmic background in the above-ground lab room of the TUM demonstrator. At HERA south hall, there would be a lower background due to the larger overburden. A reduction of the muon component by half would reduce the background index by 14%. To reach the background goal with the multi-layer setup alone, the neutron component would have to be reduced by 70%. However, the multi-layer setup is not optimized for TAXO and was merely a test to see if multiple layers reduce the background. Since this trend was shown, it can now be the basis for further shielding optimization studies.

The analysis reveals that inelastic scattering in inner layers of lead and copper is a large contributor to the background. Making the inner layers of lead thinner could reduce this background. The inner lead mainly has to shield against the gammas from PE(Bo), for which thinner layers would suffice. There is also room to add more PE(Bo) to further reduce the neutron flux. Further simulation studies have the potential to develop a shielding concept with even lower background than the current multi-layer one. There are also other strategies that can be simulated, for example adding different neutron-shielding materials or implementing a type of neutron-tagging system. Another longer-term objective of TAXO is adding a germanium detector around the SDD as an active veto, which would further reduce the background and can also be simulated.

A real measurement always contains background in addition to cosmic particles, so the results of the simulation cannot be measured directly. However, it is possible to show the reduction of the background due to different shielding configurations by comparing measurements with different shielding setups. In particular, the standard and outer PE(Bo) setup can be built with the TAXO demonstrator at TUM. These measurements are planned for the near future.

4. Demonstrator Muon Veto

The TAXO demonstrator at LSC operates deep underground. To show that the BabyIAXO background goals can also be achieved above ground, a second demonstrator is being built at TUM. Above ground, muons are an inevitable source of background. Luckily, they can be tagged. In order to identify prompt muon-induced background events at the TUM demonstrator, it was equipped with a muon veto system. This system had to be constructed and tested before it could be integrated with the SDD. It was shown to be effective at tagging muons. As a result, the above-ground demonstrator at TUM is ready for long-term background measurements.

The development of the muon veto system is the topic of this chapter. Section 4.1 shows the individual muon veto panels that make up the veto, how they work and how the full veto setup was commissioned. Section 4.2 details the first measurements that were taken with the panels, both standalone and in the veto configuration, to test and characterize them and develop a working processing chain for their raw data. Finally, Section 4.3 showcases the first coincidence measurement with the muon veto and SDD. It explains how the two components were combined into a single setup, how the combined data acquisition and veto analysis works, and shows that the veto is indeed effective at identifying and removing prompt muon-induced events.

4.1. Commissioning

The muon veto was built from six muon veto panels. Their purpose is to tag muons that pass through them, so that muon-induced events can be identified among the SDD data. In order for this to work, the panels have to cover the flush box with the SDD from all sides, leaving no way for a muon to enter it without passing through a panel. This requires building a custom muon veto setup.

4.1.1. Muon Veto Panels

The six muon veto panels, shown in Figure 22, are commercially available panels from NuviaTech. They consist of cuboidal plastic scintillators made of NuviaTech's NuDET PLASTIC material, with a 56% light yield, 2.5 ns decay time, and maximal emission at 425 nm [71]. Four of the panels are small, with a surface area of 45 cm × 50 cm, and two are big, with an area of 60 cm × 60 cm. Each of the panels is 5 cm thick.

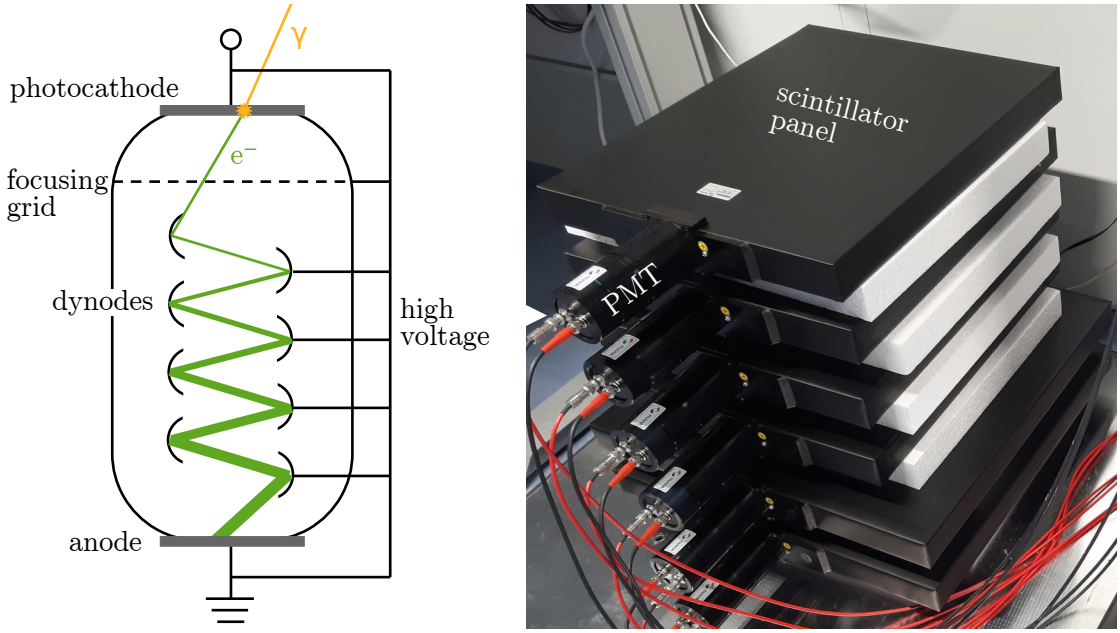

Figure 22: **Muon veto panels and photomultiplier tube (PMT) sketch**
Right are the six muon veto panels. Each PMT is connected to two cables; one supplies the operation voltage and the other one transports the measured signal. *Left* is a sketch to visualize how the PMTs work. A photon hitting the photocathode produces a photoelectron that is accelerated inwards by the focusing grid. The electron hits the series of dynodes on an increasing bias, producing secondary electrons, all of which are accelerated in the electric field and in turn produce secondaries each time they hit a dynode. This electron avalanche enhances the signal. The electrons are finally collected on the anode, where the resulting signal is read out.

The scintillator produces scintillation light when ionizing radiation, e.g., muons, passes through. It is wrapped in reflective foil and an outer layer of black vinyl, so the light is trapped within and no external light can enter. The amount of light is proportional to the energy deposited in the scintillator. To collect and read out this light, each panel is equipped with a 2" PMT of the 9266B series from ET

Enterprises [72]. The PMT converts light into an electric signal through the process sketched in Figure 22. The voltages that have to be applied to each panel's PMT, as given by the manufacturer, are listed in Appendix B. During all my measurements, the PMTs were powered using a Caen N8033 8 channel NIM power supply.

4.1.2. The Muon Cube

These muon panels had to be arranged into a veto setup, fulfilling several requirements. The SDD flush box has to fit inside, and there needs to be additional space for PE(Bo). The full setup should also be compact and easily mountable so it can be transported and set up at various locations like the shallow underground lab at TUM or the HERA south hall at DESY.

I call the fully assembled muon veto setup, shown in Figure 23, the 'muon cube'. It consists of an aluminum frame holding the six panels in a box shape. The big panels form the top and bottom and the small panels the sides. The inner part of the frame carries the top panel, which can be removed like a lid to access the setup inside. Since they are only leaning between the bars of the aluminum frame, the small panels can also be removed easily if more involved operations inside the veto are necessary. The frame was built from 3 cm item profiles as well as custom-made steel plates and feet.

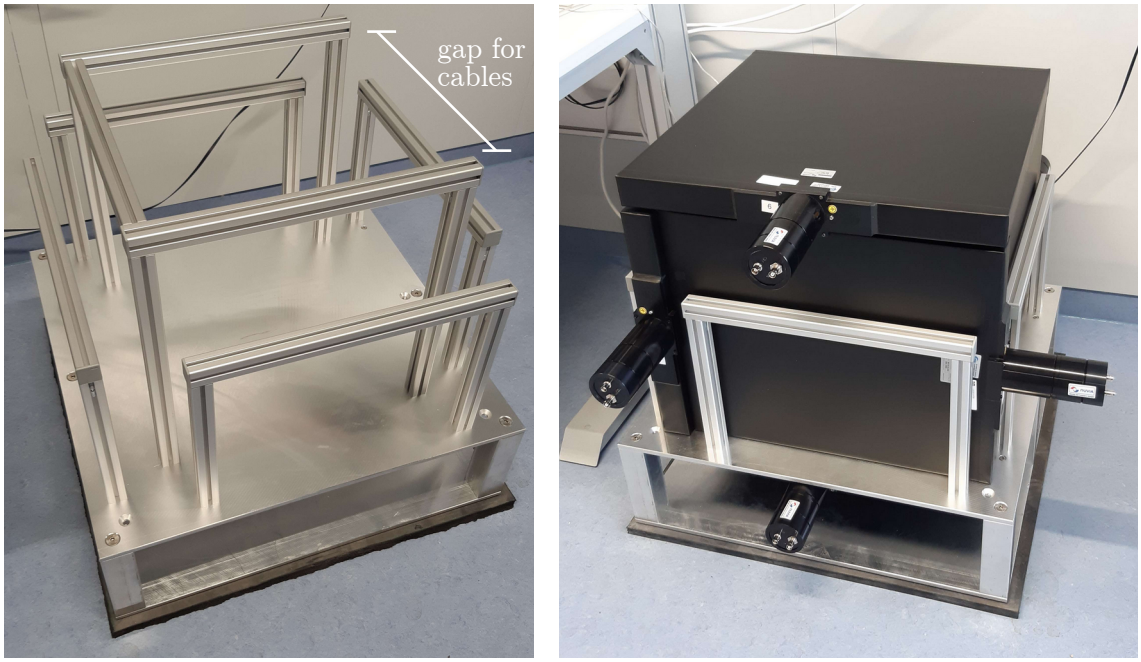

Figure 23: **Muon cube setup**
Left is the empty aluminum frame. The center part has one open side to accommodate the cables from the SDD. *Right* is the cube fully assembled. The side panels have no gaps between each other. The bottom panel hangs under the ground plate, while the top panel is slightly elevated. Despite these two narrow gaps, there is no direct path for a particle to hit the detector inside without crossing through at least one panel. This means the veto has 4π coverage of the SDD.

4.2. Characterization

To be able to work with the muon panels, they had to be tested and characterized first. These first measurements also serve to establish and test the data acquisition (DAQ) system for the panels and understand the signals they produce. Likewise, how they work together in the muon cube was investigated by taking first data with the full cube setup. These characterization measurements show that the muon cube can work as a muon veto.

4.2.1. Signal Processing

A digital signal processing (DSP) chain is used to extract parameters from the raw waveforms of the muon veto panels. These waveforms are produced by the PMTs as sketched in Figure 22. The collection of the electron avalanche on the anode results in a sharp drop in voltage, which manifests as a negative pulse on the signal baseline. For convenience, the waveforms are inverted during data taking. A waveform with one such pulse is shown in Figure 24. The waveforms are saved during data taking and processed offline.

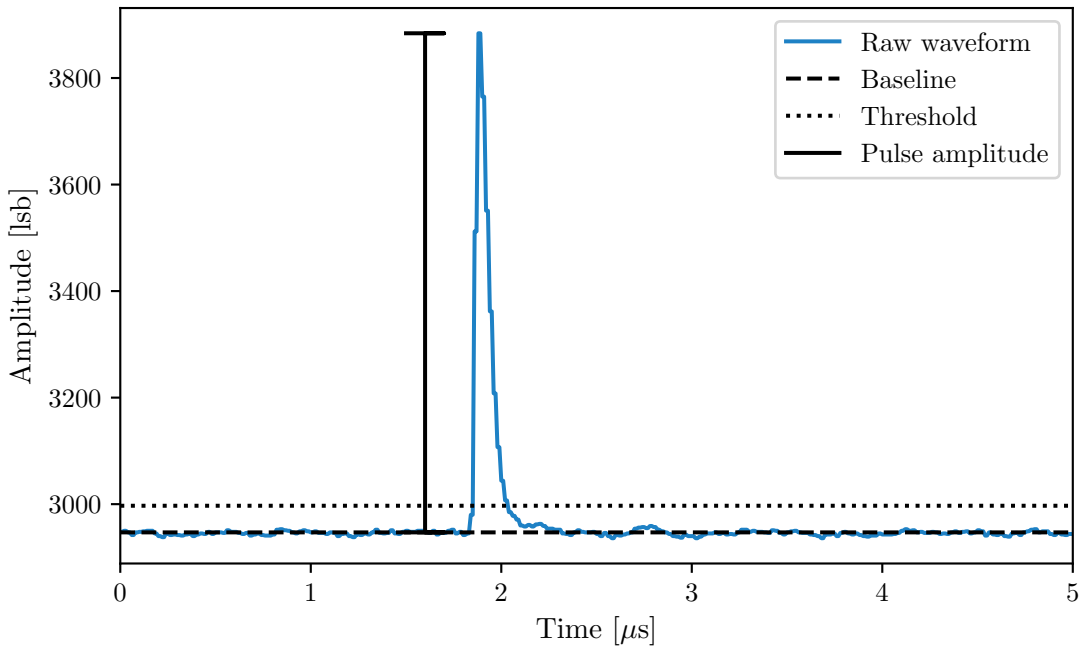

Figure 24: **Muon panel waveform with signal processing**
Waveform of a typical muon panel signal. The black dashed line marks the baseline of the waveform. The black dotted line marks the threshold of the leading edge trigger that identifies pulses. The black vertical line marks the amplitude of this pulse. The higher the amplitude, the larger the energy deposition that produced the signal.

The purpose of the DSP chain is now to extract information from these raw waveforms that can be used to identify if and when a muon passed the panel. I developed a chain that follows the steps sketched on top of the waveform in Figure 24. The first step determines the baseline of the waveform. It does so by finding its mode, which

is the most common value. Subtracting this value leads to a corrected waveform with a baseline at zero. The next step finds signal pulses and saves their positions on the waveform. It uses a simple leading edge trigger with a threshold I set by hand to sit above the general noise level of the baseline. The final step reconstructs the pulse energy. For the purposes of this veto, it is sufficient to use the pulse's amplitude as an energy value. In the end, the DSP chain produces a baseline, a corrected waveform with its baseline at zero, a list of trigger positions and for each trigger an amplitude of the associated pulse.

4.2.2. Efficiency Measurement

The detection efficiency e_{det} of a particle detector describes how likely it is for a particle hitting the detector, in this case a muon hitting the scintillator, to be detected. It can be calculated from a total number of incident particles N_{tot} and the number of those particles that are detected N_{det}:

$$e_{det} = \frac{N_{det}}{N_{tot}}. \tag{8}$$

It is an important parameter to know for the muon panels, since it indicates how well the veto can identify muon-induced events.

4.2.2.1 Setup

To be able to measure both the number of detected events N_{det} and a reference N_{tot}, I stacked three panels on top of each other as shown in Figure 25. The panel in the middle is the one whose efficiency is measured, called the 'sample'. The top and bottom panels are called the 'taggers', since their purpose is tagging muons. The stack was shuffled between measurements so that each one of the six panels was in the sample position once. Muons can fly through the whole stack and cause a signal in both tagger panels. A muon hitting both taggers must also pass through the sample. Therefore, the events with coincident signals in both taggers can be used as reference count of muons passing through the sample N_{tot}. Of course, events in the tagger panels can also be coincident by chance, not because they were caused by the same muon. This random coincidence has to be accounted for during the analysis.

The panel signals were recorded by the flash analog-digital converter (FADC) shown to the right in Figure 25. It is a Caen V1782 Multi Channel Analyzer, a FADC with eight input channels of 16 bit resolution and 1 MHz sampling rate. It can be configured and programmed via the software CoMPASS. Whenever any one of the panels triggered the FADC, all waveforms were saved for offline analysis. Each run lasted around 10 minutes, collecting in the order of 10^5 total events for each panel.

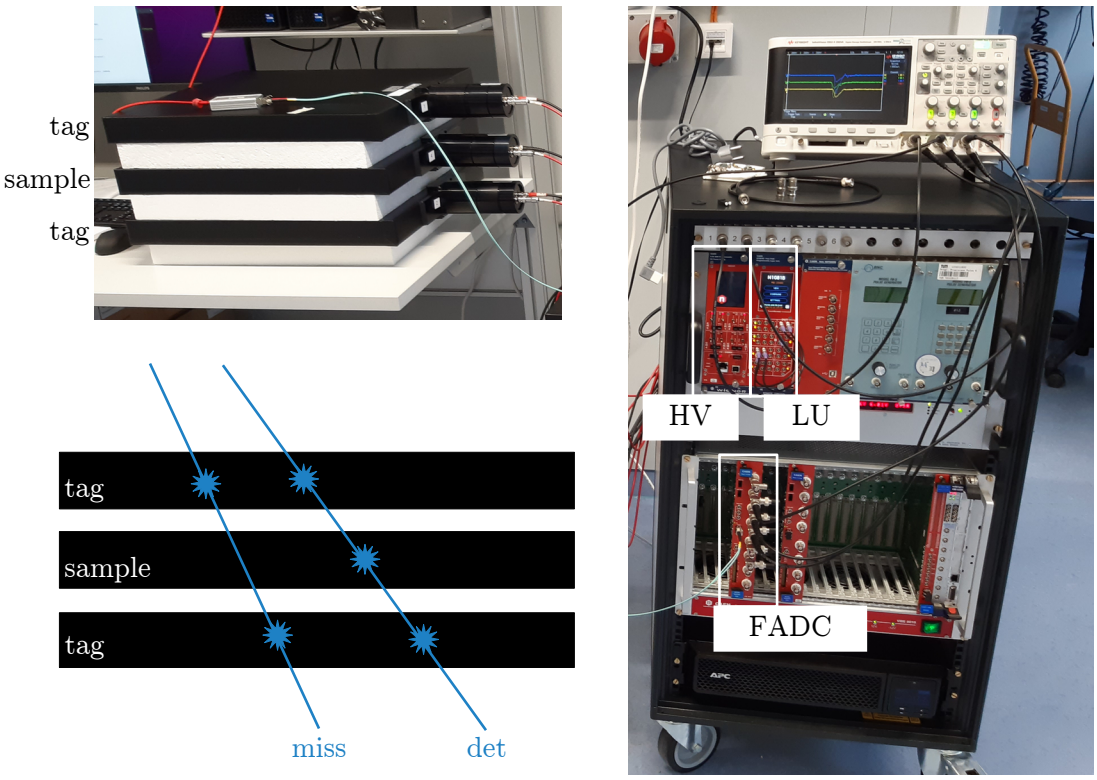

Figure 25: **Setup to study the detection efficiency of the muon panels**
Bottom left is a sketch of the setup, showing the two types of events I used to calculate the detection efficiency of the sample panel. A missed event **miss** is one that is coincident in both tagger panels with no signal in the sample panel. A detected event **det** is coincident in all three panels. *Top left* is a photograph of the same setup, showing three panels stacked atop each other. Each panel's PMT has two cables plugged into it. One cable provides power and is connected to the high voltage supply on the *right*, marked **HV**. The other cable carries the electronic signal from the PMT to the data acquisition unit marked **FADC** on the right. It is connected to the lab PC on the same desk as the panels via the light green optical fiber. Next to the voltage supply is the logic unit **LU**, which can be used to record rates and construct logic functions.

4.2.2.2 Analysis

The recorded waveforms were processed with the DSP chain explained in Section 4.2.1. Two signals were flagged as coincident if their leading edge timestamp fell within a window of 100 ns of each other. For the detection efficiency I only considered tagged muon events, where both taggers measured a coincident signal. Of those, there were two types: Detected muons, where the sample panel also saw a signal, and missed muons, where the sample panel saw no signal. Counting each type of event gave the two numbers N_{det} and N_{miss}. Since the reference count N_{tot} is the total number of events tagged by both taggers, which is the same as $N_{miss}+N_{det}$, the detection efficiency e_{det} of the sample panel is

$$e_{det} = \frac{N_{det}}{N_{det} + N_{miss}}. \tag{9}$$

Events can also be coincident by chance. Since it is more likely for two events to be randomly coincident than three, this can skew e_{det} towards smaller values. This random rate can be determined by adding a time shift to the triggers of one of the tagger panels. The events that are coincident between an unchanged tagger and a time-shifted tagger are considered random. This method effectively eliminates truly coincident events, leaving only the random ones.

I investigated this random coincidence for each of the six runs by time-shifting the data of one tagger by n seconds. Starting with $n = 100\,\text{ns}$, so right outside the 'true' coincidence window, I made n larger in 10 ns steps to see if the random coincidence stayed consistent. It fluctuated around 3 counts and never exceeded 12, which for a true coincident event number in the order of 50000 is negligible. Randomly coincident events can be disregarded, since they have a much smaller impact on the results than random statistical fluctuations, which are in the order of 100s of counts.

4.2.2.3 Results

For each sample panel, I calculated the detection efficiency with Equation (9). The resulting values, shown in Figure 26, are fairly consistent between panels and all above 98%. This is a satisfying efficiency, since it means most muon events can be tagged by a single panel. When the panels are in the cube setup, they cover the SDD detector from all sides. This means that a muon going through the setup and detector has to pass through two panels, in which case the ratio of missed muons is less than $2\% \cdot 2\% = 0.04\%$.

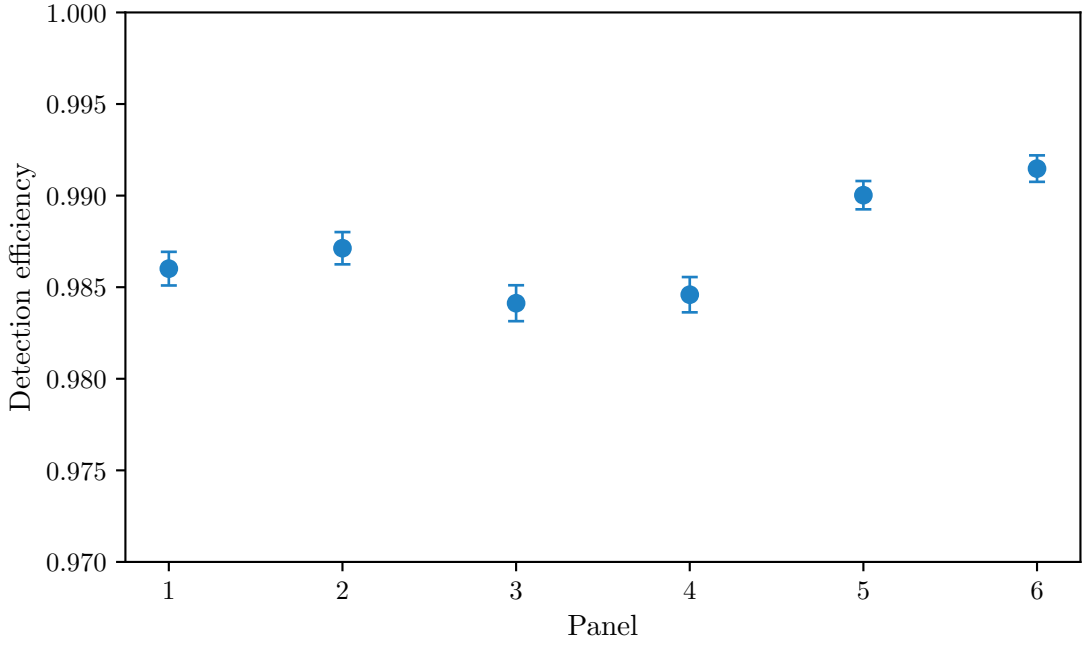

Figure 26: **Detection efficiency of each muon panel**
Panels 1 to 4 are the small ones, panels 5 and 6 the big ones. The detection efficiencies range between $(98.4 \pm 0.1)\%$ and $(99.2 \pm 0.1)\%$. The error bars are 1σ uncertainties.

The measurement also gave an opportunity to investigate the energy spectrum of each sample panel. One such spectrum is shown in Figure 27, where events in coincidence with at least one or both tagger panels are also marked. It illustrates nicely that muons can pass through multiple panels while particles such as gammas that are mainly responsible for the peak at lower energies mostly deposit energy in just a single panel. Said peak is also clearly separated from the energy hill caused by muons. Therefore, muon events can be distinguished from other events by setting an energy threshold between the low-energy peak and the muon hill.

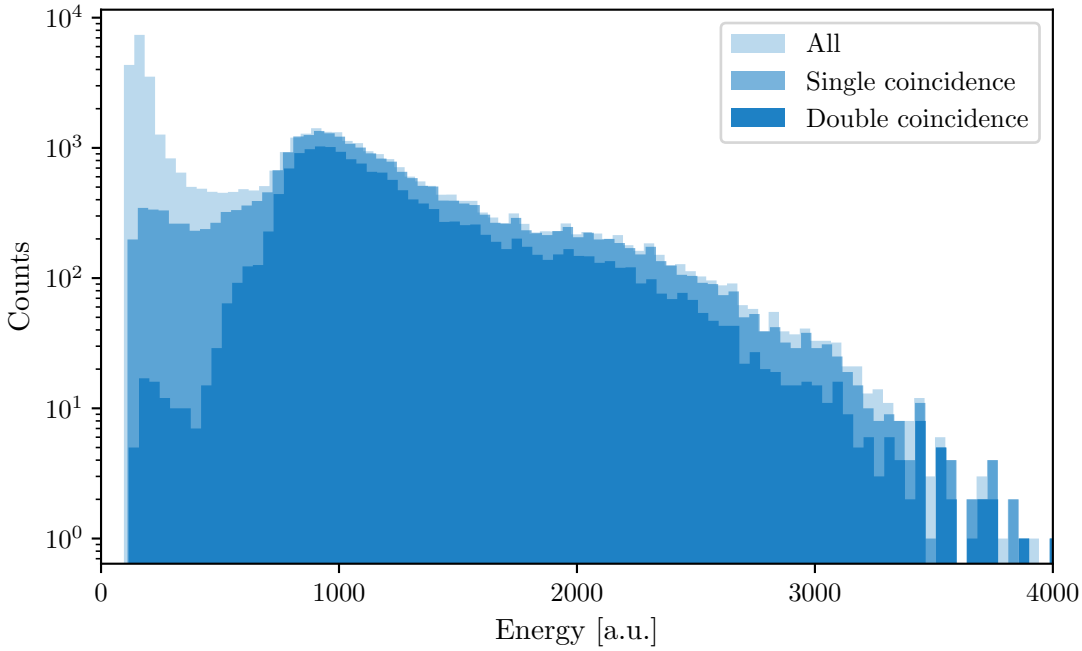

Figure 27: **Energy spectrum of a sample panel from the efficiency study setup** Light blue are all events, medium blue are events with a coincident event in at least one of the tagger panels, and dark blue are events with coincidence between the sample and both tagger panels. The peak at lower energies becomes increasingly smaller for higher number coincidences. The hill at higher energies is caused by muons, which can pass through two or three panels easily.

4.2.3. Muon Cube Measurement

After the efficiency study, I assembled the muon panels into the cube and took data with them for 10 minutes. The DAQ was identical to the efficiency study. Upon triggering on one panel, all waveforms were saved and later processed with the same DSP as before. The muon cube measurements allow for comparisons between the muon cube and efficiency study setup. The cosmic muon flux follows a $\cos^2(\theta)$ distribution [73], meaning it is maximal from above and decreases to zero at angles parallel to the earth's surface. Muons deposit more energy in a material if they pass a longer distance through it. Both effects were reflected in the muon cube measurement, which shows that the muon veto works as expected.

4.2.3.1 Energy Spectrum

The energy spectra taken in the muon cube can be compared to those of the efficiency setup. The spectra of the big panels look the same in both setups, while the ones of the small panels look different. Figure 28 shows this difference for one panel. While the big panels are horizontal both times, the small panels are horizontal in the efficiency study and vertical in the muon cube. The muon hill that was so prominent in the efficiency study spectra is the energy deposited by muons passing through the 5 cm height of the panels. This hill is significantly flattened in the muon cube setup since for a muon to pass through the small panel the same way, it must come at a shallow angle, which is rarer than a muon coming from above. Muons from above enter the panel from its side and can create a much longer path through the scintillator, with a higher associated energy deposition. This is why the energy spectrum in the muon cube configuration has more events at higher energies than the efficiency study setup.

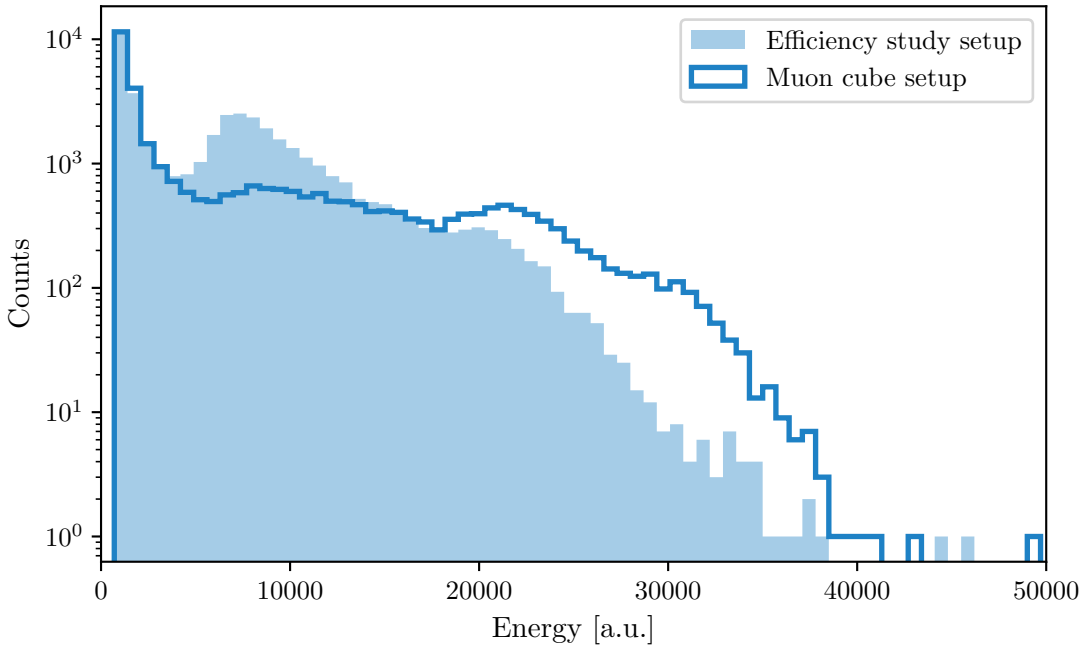

Figure 28: **Energy spectrum of a small panel for different orientations**
In the efficiency study setup, the panel is horizontal, while in the muon cube setup it is vertical. The peak at small energies looks identical between both setups. The muon hill above this peak is flattened and shifted to higher energies in the muon cube setup. This shows how the energy deposited in the panels by muons depends on the orientation of the panels.

The low-energy peak is identical between setups for large and small panels. Events causing energy deposition in this peak are independent from the orientation of the panels. This shows that these low-energy events are indeed not caused by direct muons, but ambient radioactivity and other types of events. Setting an energy threshold to distinguish muons from other events is therefore viable regardless of the panel orientation.

4.2.3.2 Panel Coincidence

As opposed to the efficiency study setup with three panels above each other, the muon cube has six panels in a more complex arrangement. Different pairs of panels record different amounts of coincident events, as shown in Figure 29. As before, coincidence was defined as two events being within 100 ns of each other. The top and bottom panel have the most coincidences. The side panels also have more coincidences with either the top or bottom panel than with any other side panel. This reflects the direction of the muon flux: Muons coming at a steep angle are most likely to pass through the top and bottom panels, with a smaller likelihood of also passing through a side panel. For a muon to pass through two side panels, it must come at more shallow angles that are suppressed with $\cos^2(\theta)$.

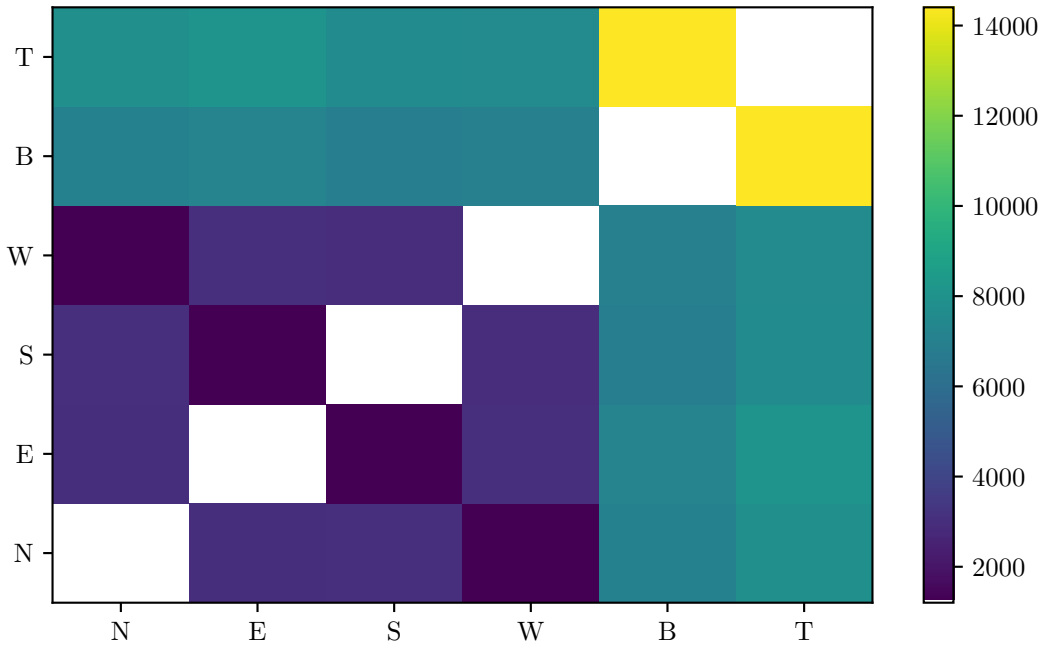

Figure 29: **Coincidence between panels in the muon cube**
For this plot, the panels are named after their position in the cube rather than their usual numbering: **N**orth (Panel 3), **E**ast (Panel 1), **S**outh (Panel 2), **W**est (Panel 4), **B**ottom (Panel 5) and **T**op (Panel 6). This way, their relation to each other is clear. The amplitude is the absolute number of events that are coincident between the two panels on the x and y axis.

As established when discussing the energy spectra, the low-energy events can be distinguished from muon events by applying an energy threshold. The values in the plot do not include this threshold, meaning they contain all events regardless of energy. Applying an energy threshold to select only muon events mainly does one thing: Removing events that are not coincident at all, which does not affect the appearance of the plot. This reflects the observations made earlier: That muons deposit energy in several panels while other sources mainly deposit energy in a single panel, and that the geometry of the muon cube is such that most muons pass through multiple panels. This makes the muon cube well suited to be a muon veto system.

4.2.3.3 Rate

The rate measurement was an opportunity to test the logic unit (LU) shown in Figure 25, since it is an important component of the full demonstrator setup. It is a Caen N1081B programmable logic unit with four sections that can be independently programmed to process signals with a variety of logic functions. In both the efficiency study and the muon cube setup, I connected the muon panels to the inputs of one section of the LU. The section was configured as a ratemeter, a setting where the unit simply counts the events that pass the set trigger threshold each second. It cannot record waveforms or reconstruct event energies. I recorded the rates of each panel with a threshold of 50 lsb for 3 minutes in the efficiency setup and for 10 minutes in the cube setup.

The rate of each panel was normalized by its area, the largest surface of the scintillator panel. Once again, the direction of the muon flux affects the small panels, in this case by reducing the normalized event rate in the setup where their area points sidewards and not up, as shown in Figure 30. The horizontal panels all detect a rate around $0.02\,\mathrm{Hz\,cm^{-2}}$. The muon flux at sea level is commonly approximated as one particle per cm^2 and minute [61]. The detected rates are slightly higher, since they also contain events not caused by muons. Therefore, the measurement is in good agreement with expectations.

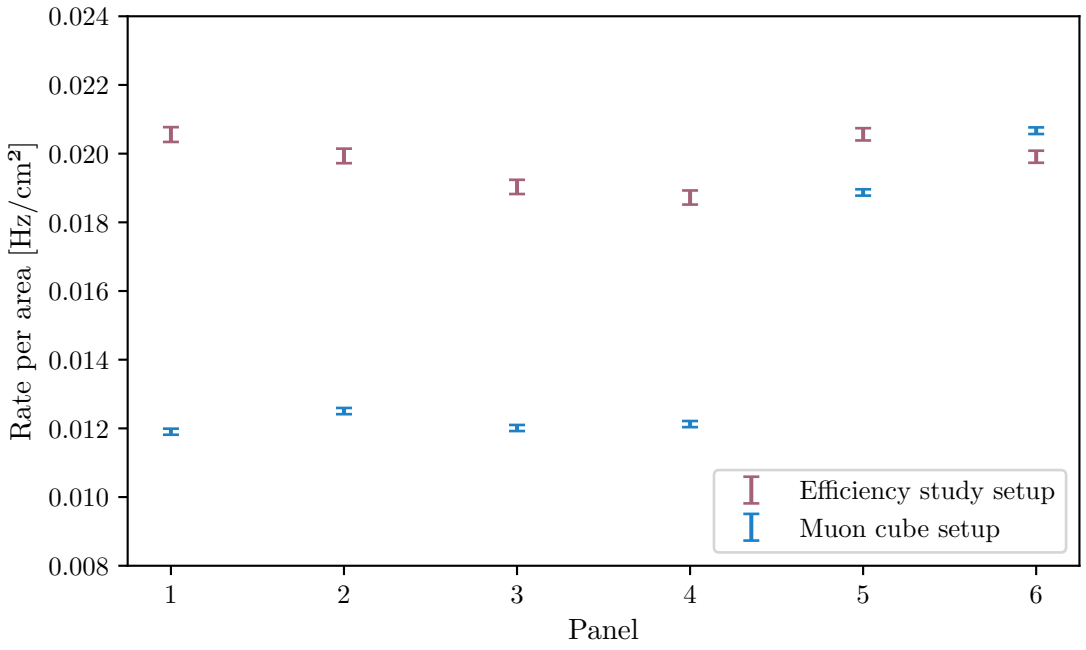

Figure 30: **Event rates in all muon panels across setups**
The total event rate in each panel, normalized by the area of the panel. Panels 1-4 are the small ones, panels 5-6 the big ones. The big ones are horizontal in both setups and so their rates stay consistent. The small panels see a drop in rate once they are put from a horizontal to a vertical position. The error bars are 1σ statistical uncertainties.

4.3. Coincidence Measurement

With the muon cube operational, it was time to develop it into a full muon veto system. To develop and test the system, I took ten days' worth of data with the muon cube and SDD together. This measurement was used to develop the DAQ configuration and analysis chain for the muon veto. The same tools developed here will later be used in a background measurement of the full demonstrator.

4.3.1. Configuration

Since the previous measurements only used up to six muon panels, configuring the DAQ was straightforward. Adding the seven-pixel SDD makes it much more complex. All channels should be read out once any one of the pixels triggers, but there should be no independent trigger on the muon panels. The purpose of the muon panels is to act as a veto for SDD events, so the high rate of muon events with no SDD signal is uninteresting. There should also be no trigger when the SDD is resetting. The detector is operated with a pulsed reset amplifier that continually accumulates charges and is reset either at regular intervals or when a set threshold is reached. This reset causes a signal on the detector waveforms that can trigger the DAQ. Recording the reset would produce a large volume of useless data and should therefore be avoided.

4.3.1.1 Setup

This measurement is meant to test the DAQ and muon veto system for the eventual background measurement. As such, the setup shown in Figure 31 approaches that of the full TAXO demonstrator, except for the shielding materials. The muon cube is unchanged from the characterization measurements, and the SDD is added inside the cube.

The muon panels are supplied by the same high voltage (HV) supply as before. The SDD is supplied with all necessary voltages by a bias board manufactured specially for this detector by XGlab. It is housed in a custom-made NIM module I built for the demonstrator setup. In addition to the voltages, the bias board also handles communication with the detector board, defines the reset logic, and provides the waveforms of the pixels. Each pixel is connected to one input of an 8-channel FADC, the same model as used in the characterization measurements previously. A second, identical FADC receives all the panel signals. Both FADCs are connected and synchronized in a daisy chain configuration. The FADC boards and the logic unit together make up the DAQ system for this measurement.

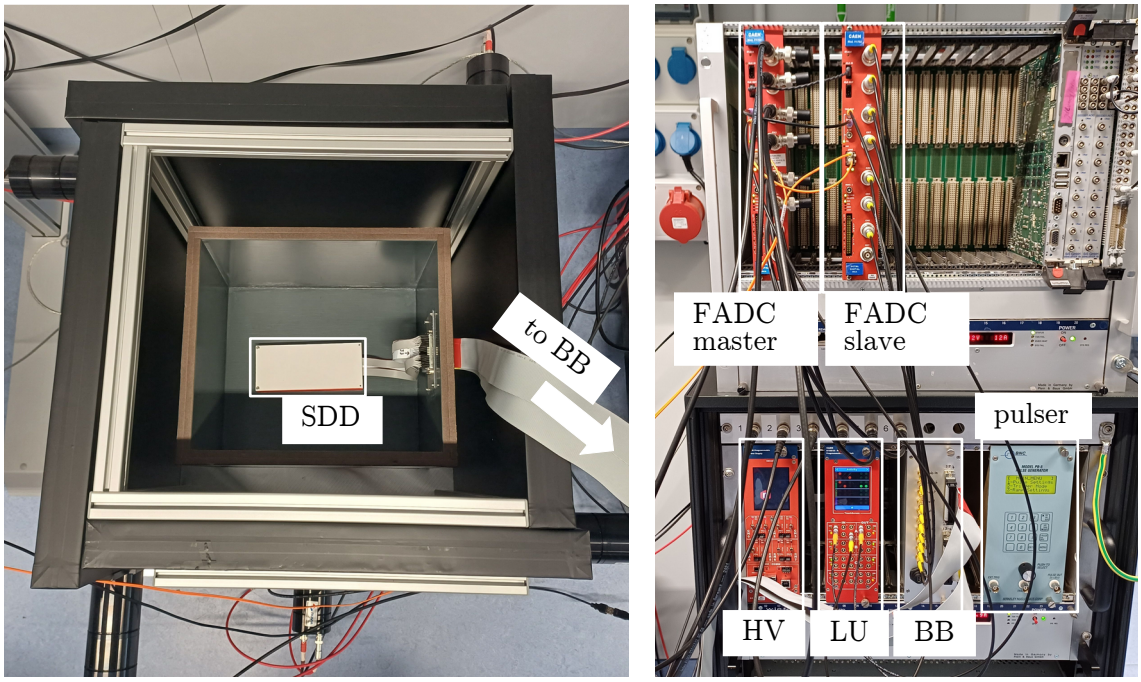

Figure 31: **Setup of the coincidence measurement**
The muon cube has the top panel removed to show the flush box inside. The flush box in turn is opened to reveal the **SDD** inside a small plastic case. There is no shielding inside the box. For the measurement, both the flush box and the muon cube were closed. The muon veto panels are connected to the high voltage supply **HV** and one **FADC** the same way as in the characterization measurements. The SDD is connected to the bias board **BB** via two flatband cables. The channel outputs from the bias board are connected to the other **FADC**. The logic unit **LU** is connected with both FADCs to create a trigger for the DAQ, which is explained in more detail in Figure 32. The **pulser** will be used in the background measurement to monitor the stability of the SDD, but was only tested and not used further in this measurement.

4.3.1.2 Data Acquisition

Setting up the DAQ was not trivial. Two FADC boards must be operated in sync to accommodate all 13 channels. The synchronization produces one 'master' board and one 'slave' board, with the master propagating its internal clock and the signal to start and stop data acquisition to the slave. However, when the boards are synchronized, there is no way to feed them a veto signal that prevents triggering on unwanted signals. But such a veto is necessary, since the SDD reset should not be recorded. This problem was solved by constructing an external trigger signal for the FADCs using the LU. Figure 32 shows and explains the full DAQ configuration in detail.

All 13 channels should be read out once any one of the SDD channels triggers the DAQ, except during a reset. The slave board's internal global OR trigger is a logic signal that is logic high whenever any one of the SDD channels triggers. Notably, this includes the reset. The inhibit of the bias board is logic high during the reset. The LU now receives both signals and constructs a signal that is logic high whenever an SDD channel triggers, but logic low during the reset. This external trigger is then

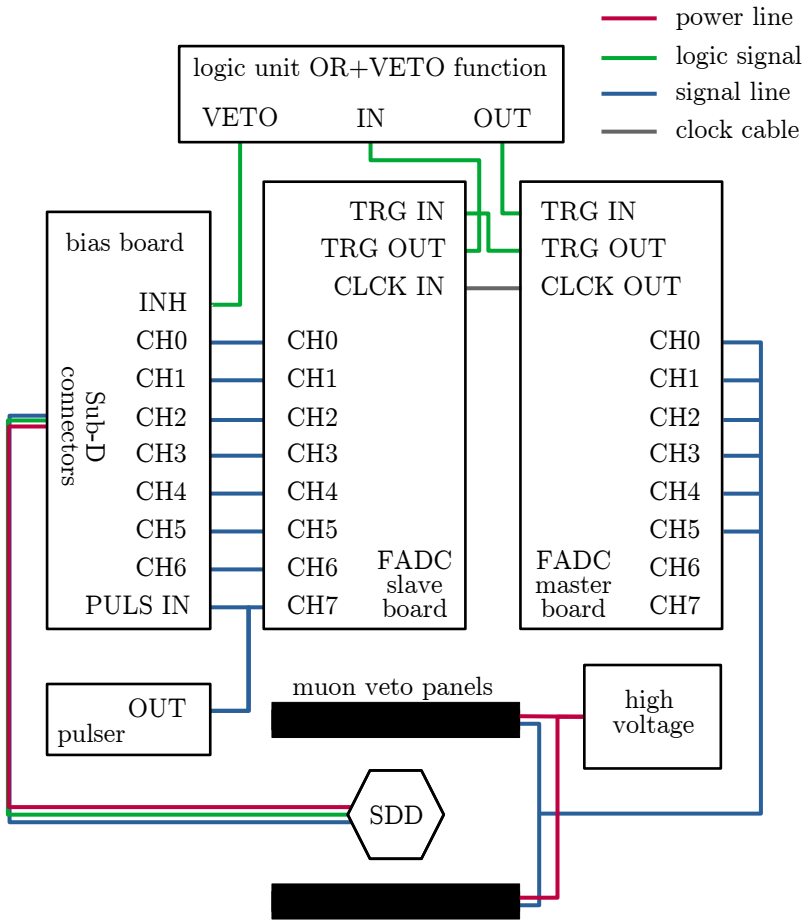

Figure 32: **Circuitry diagram for the coincidence measurement**
The **high voltage** supply provides power to the **muon veto panels**. The panels surround the **SDD**. The SDD is connected to the **bias board** via flat-band cables. The bias board supplies the SDD with all necessary voltages and gives out the signals of each SDD pixel on channels **CH0-6**. These outputs are connected to the inputs **CH0-6** of the 8-channel **FADC slave board**. The muon veto signals are connected to inputs **CH0-5** of the **FADC master board**. For both FADCs to operate in sync, a clock cable must be connected from the **CLCK OUT** of the master to the **CLCK IN** of the slave and the **TRG OUT** of the master to the **TRG IN** of the slave. The **TRG OUT** of the slave is connected to the **IN**put of one block of the **logit unit**, with the **TRG IN** of the master connected to the **OUT**put of the same block. The purpose of this block is to construct a trigger signal that excludes the reset of the SDD. The block is configured as a **OR+VETO function**, and the inhibit **INH** from the bias board that signifies the reset is connected to its **VETO** input. With this configuration, the logic unit output is a logic signal that is logic high whenever the SDD triggers, except when there is a reset. This logic signal, since it is connected to the trigger input of the master board, causes all channels to be read out on that board. The master propagates the same trigger to the slave, where likewise all channels are read out. This way, the waveforms of all channels are saved when the SDD triggers, but not when it resets. The **pulser** can be connected to the **PULS IN** of the bias board and the last input **CH7** of the slave board to monitor the long-term stability of the SDD. In this measurement, the pulser was not used, but it was tested as part of the setup and so is included in this diagram.

propagated to the master board, and from there to the slave board. Both boards save all channel waveforms when this external signal is logic high. For the boards to propagate the correct internal signals and read out their channels in this way, they must be programmed with a custom file. This file can be found in Appendix B, together with all other DAQ settings of the coincidence measurement.

4.3.2. SDD Analysis

Just like for the muon panels, the first step in analyzing the SDD is to process the raw waveforms. The existing DSP chain for the SDD works similarly to the DSP for the muon panels, correcting the baseline, providing trigger information, and reconstructing the energy. However, it does so using a series of trapezoidal filters. After the SDD waveforms are processed with this chain, they can be further analyzed.

4.3.2.1 Calibration

Unlike for the panels, the actual energy of the SDD events is relevant, so the detector must be calibrated. This happened by fixing an ^{241}Am source over the detector and recording the spectrum of this source. It has a prominent gamma line at 59.5 keV, as shown in Figure 33. By fitting a gaussian to this peak for each pixel individually and assuming a linear energy behavior, the pixels were calibrated. That a linear assumption is sufficient for a rough calibration is supported by the detailed calibration and characterization of the SDD in the LSC demonstrator in [57].

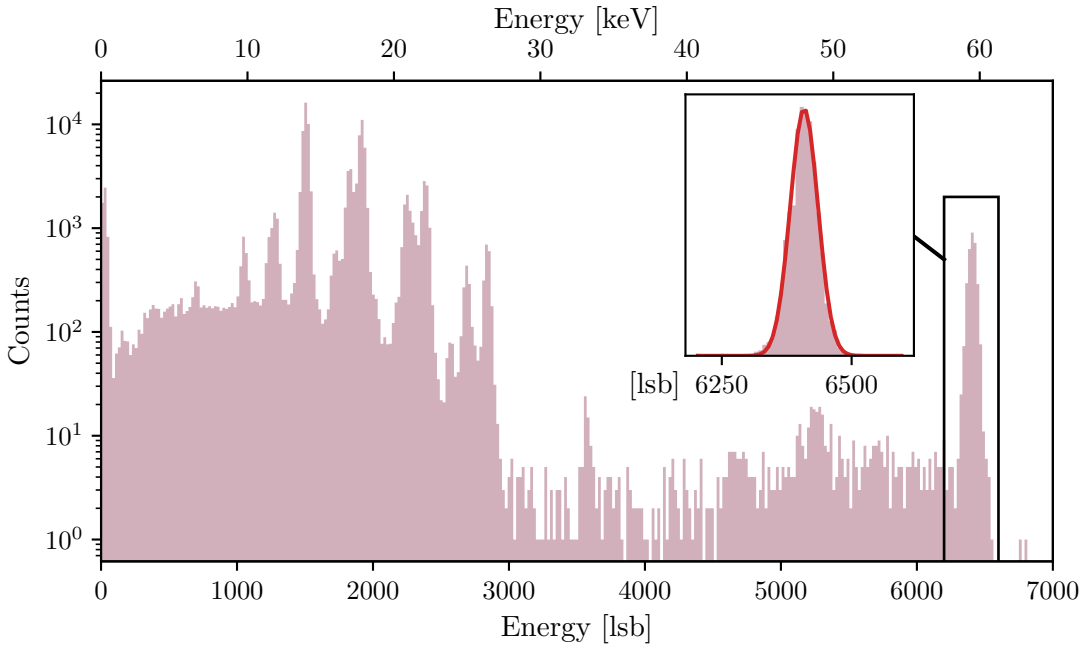

Figure 33: **SDD pixel calibration with an ^{241}Am spectrum**
Spectrum of an ^{241}Am source recorded with one pixel of the SDD. A gaussian fit of the peak at 59.5 keV was used to calibrate the energy for each pixel.

4.3.2.2 Quality Cuts

Of the recorded waveforms, not all are good. Bad waveforms can include those that contain something that is not a physical event, or events that are not usable. If the DSP chain cannot handle them correctly it produces parameters, especially energies, that are faulty. They should be removed to leave only waveforms that are actual events and that the DSP can process without issue. This is the purpose of the cuts performed at this stage. Figure 34 shows an example of a good waveform, compared to several other recorded waveforms that should be removed.

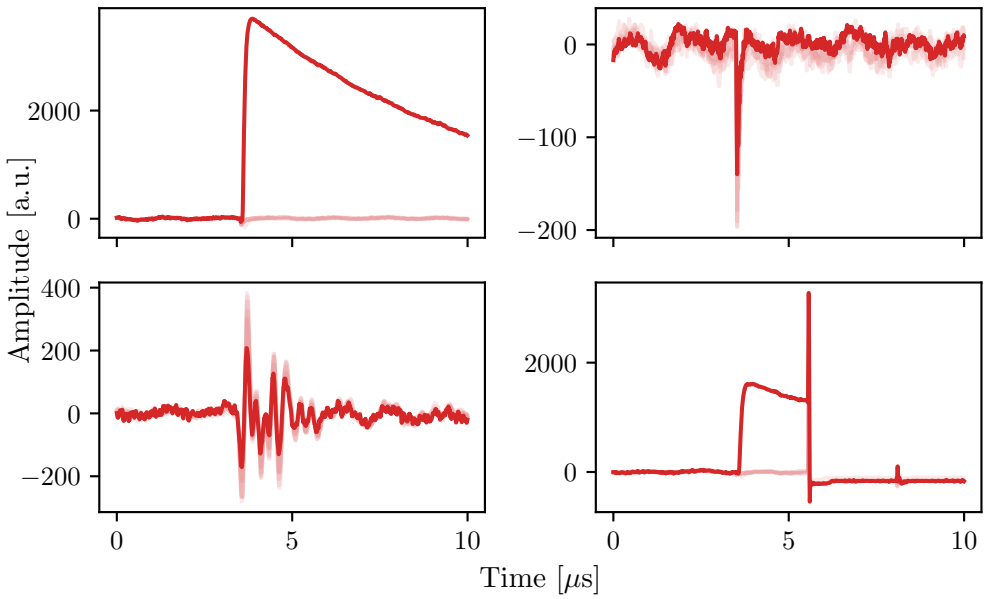

Figure 34: **SDD example waveforms**
Top left is a regular event of the SDD. One pixel sees a signal, which has a fast rise time and an exponential decay. *Top right* is an event that is entirely crosstalk from the muon veto. None of the SDD pixels see a real signal, only a sharp negative peak. *Bottom left* is an event that triggered due to noise coupling into all channels. *Bottom right* is an event that starts the same as the regular event top left, but is interrupted by the reset. Only one pixel sees the signal that initially triggered, but all pixel waveforms are distorted by the reset pulse.

The first cut removes all events with an energy below 2 keV. Waveforms with an energy below this value include those triggered by electronic noise coupling onto the waveforms and crosstalk events. There was an unexpected amount of crosstalk between the muon veto and SDD channels, discussed further in Section 4.3.3.2. In principle, lower thresholds are also possible, but for the purposes of this measurement a 2 keV cut was implemented.

The second cut removes all signals with more than one trigger per waveform. These include pileup events, which the DSP may not accurately reconstruct the energy for. In theory one could write a DSP that could handle pileup as well, but the amount

of pileup events is negligibly small. Most multi-trigger events are either excessively noisy with many triggers or have two triggers due to the reset happening on an event waveform. The reset itself is not recorded, but if it happens immediately after the DSP is triggered by a real signal, it distorts the waveform.

The last cut removes all signals with abnormal baseline fluctuations. Unlike the one for the muon panels, the DSP chain for the SDD determines the baseline by taking the mean of all values for a beginning stretch of the waveform. It also returns a standard deviation for the baseline, which is an indicator for the noise situation. By plotting the distribution of these standard deviations for each pixel, I identified the events with excessive noise and set a threshold to cut them.

Overall, these quality cuts removed a large fraction of all recorded events, although how many differs across different runs. I raised the DAQ threshold of the measurement after discovering the crosstalk discussed in Section 4.3.3.2. For the runs with a lower threshold, only around 5% of events remained after the quality cuts. For the runs with higher threshold, it was around 11%. In both cases, a large number of the cut events appears to have been this crosstalk.

4.3.3. Veto Analysis

The SDD events remaining after the quality cuts contain events caused by muons and events not caused by muons. Identifying the ones caused by muons requires developing an analysis for the muon veto. This analysis has to combine the SDD data and the PMT data to determine if the SDD event was coincident with a muon veto event.

4.3.3.1 PMT Analysis

The waveforms of the muon panel PMTs were processed with the DSP chain described in Section 4.2.1. There was no calibration and no quality cuts. To identify the muon events, the energy spectra were plotted for each panel. I manually set a threshold between the low-energy peak and the bulk of the spectrum. As shown in Section 4.2, this bulk is the energy directly deposited by muons. PMT pulses with an energy above this threshold were therefore considered to be caused by muons. Pulses with an energy below this threshold were discarded. For each muon pulse, the position of the respective leading edge trigger on the waveform was saved since it gives important timing information. In the end, the PMT analysis returns for all recorded events a list of muon pulses and their positions.

4.3.3.2 Muon Veto Crosstalk

While analyzing the PMT and SDD signals, I discovered a type of crosstalk between the muon veto and SDD. It shows on events where there is a simultaneous high energy pulse on all, or nearly all, muon panel waveforms. The SDD waveforms then

have a small negative peak at the same time, which triggers the DAQ and leads to these events being recorded. Figure 35 shows an example of such a crosstalk event.

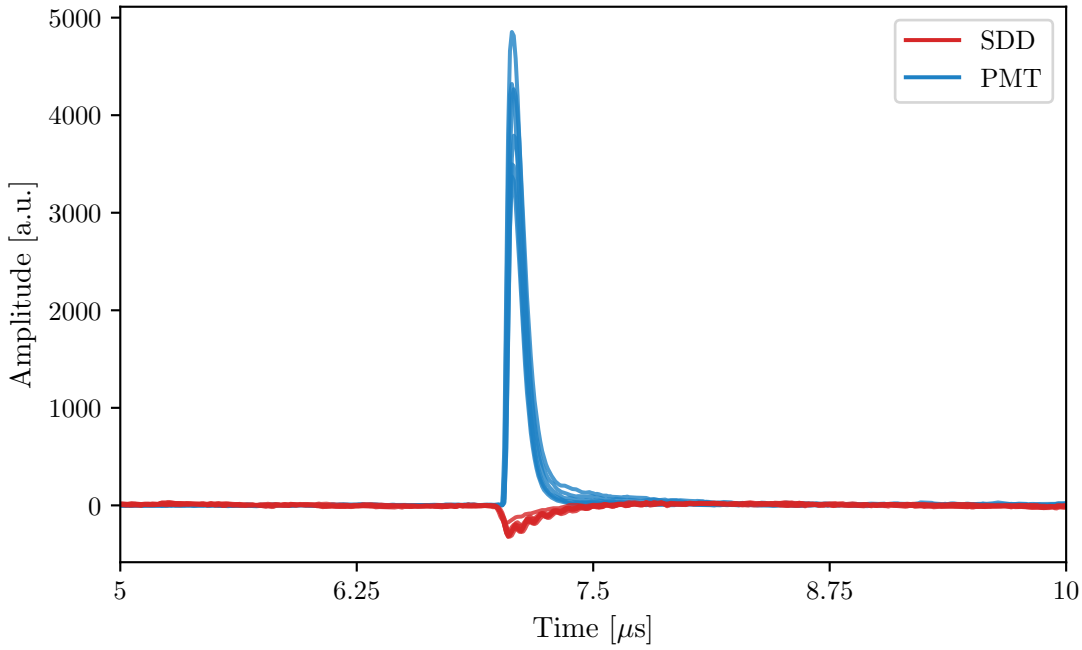

Figure 35: **Example for crosstalk between the muon veto and SDD**
The PMTs of all six muon panels show a simultaneous pulse of similar height. At the same time, all SDD channels have a small negative signal. The crosstalk on the SDD channel is what triggers the DAQ and leads to these events being recorded. The events occur only for high-energy PMT signals.

It appears that high-energy PMT pulses induce crosstalk in the SDD. Crosstalk does not show up for lower-energy PMT pulses. This crosstalk's likelihood looks to be proportional to the signal's amplitude. Those lower-energy events also do not have as many simultaneous PMT pulses. Lower energy events that look to be muons passing through the setup have simultaneous pulses on two or three PMT waveforms, while the high energy events that induce crosstalk in the SDD frequently see five or six simultaneous PMT pulses. What the source of these signals is and at what point of the setup the crosstalk happens is not clear.

These events make up a significant amount of all recorded events. Setting the DAQ threshold higher can mitigate them somewhat. If there are DAQ settings that fully or mostly eliminate these events during data taking has yet to be investigated. Another way to eliminate these events would be to implement a cut during the SDD analysis that removes events with a negative signal. Since the muon veto crosstalk signals on the SDD get reconstructed to small energies by the DSP, these events are nearly eliminated by the 2 keV cut. This is sufficient for this measurement, but a better solution can be found for the proper background measurements.

4.3.3.3 Timing

At this point in the analysis, there is a number of quality SDD events and a number of muon events detected by the muon cube. For an effective veto, the muons have to be identified with their respective SDD events. This happens by comparing the timing of the events. If the trigger position of a SDD signal falls within a certain time window of a muon pulse, it is considered a prompt muon-induced event and can be cut. To determine a reasonable time window and understand the time relationship between the muon veto and SDD better, I plotted the time difference between the SDD triggers and PMT pulse triggers in Figure 36.

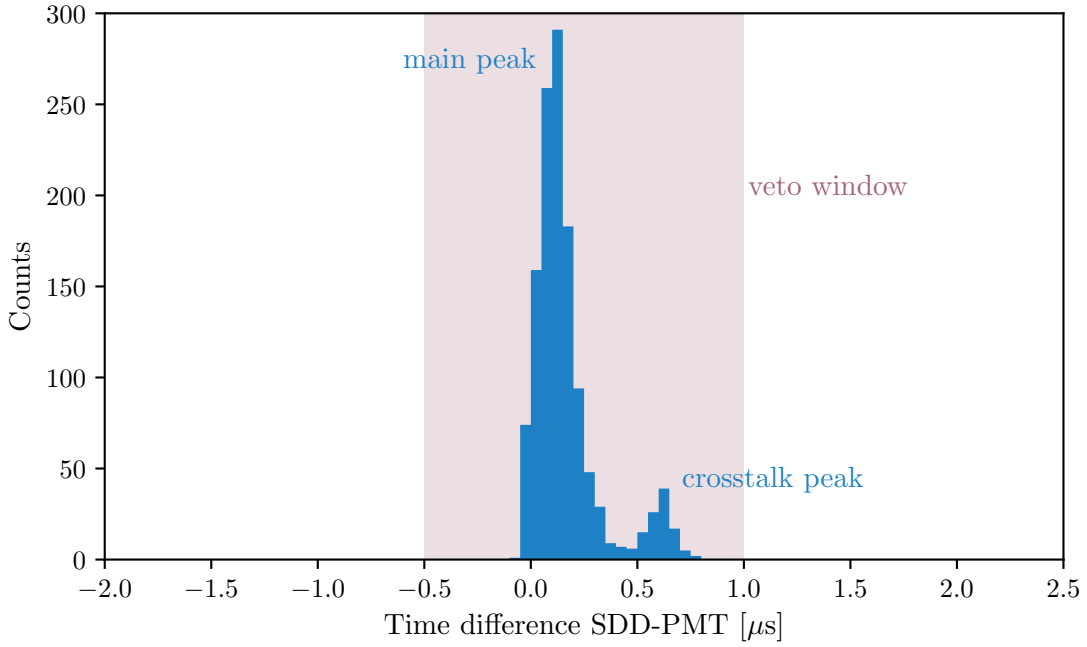

Figure 36: **Muon veto timing**
Time difference between the trigger of the SDD pulses and PMT pulses recorded in the same event. This plot combines all SDD channels and all PMT channels. The values are mostly positive, which means that the leading edge of the PMT signals mostly happens before the SDD signals. There are two peaks. The larger one is the time difference between muon-induced signals in the veto panels and SDD. The smaller one is from crosstalk induced by the main SDD signal on another SDD pixel. The colored area is the time window for the veto. If the time difference falls within this window, the SDD event is cut by the muon veto.

The main peak of time differences is not centered around zero. Rather, it is shifted to positive times, meaning that the muon veto signals happen earlier than the SDD signals. This is caused by the drift time in the SDD. Charge carriers produced in the bulk of the detector must drift towards the anode before they can be detected, which takes some time. Contrast this to the muon veto panels, where instead of charge carriers it is photons that have to traverse the scintillator to the PMT, which happens at the speed of light. Other effects, like different cable lengths, are negligible in comparison. A measurement of a seven-pixel SDD of the same type as the one

used here showed drift times between 20 ns, if the charge carriers are produced close to the anode, and 470 ns, if the charges are produced at the pixel edge [74]. This matches the width of the main peak.

Notably, there is a second peak at higher time differences. This peak is due to crosstalk induced by the main SDD signal on another pixel, as shown in Figure 37. Just like the crosstalk shown previously between the muon veto and SDD, the crosstalk waveform first drops to negative values and then rises again. If the energy reconstructed by the DSP chain is high enough, it is not removed by any quality cuts. Since the crosstalk pulse is delayed compared to the main signal, the time differences between muon veto signals and crosstalk signals such as this one end up in the second peak.

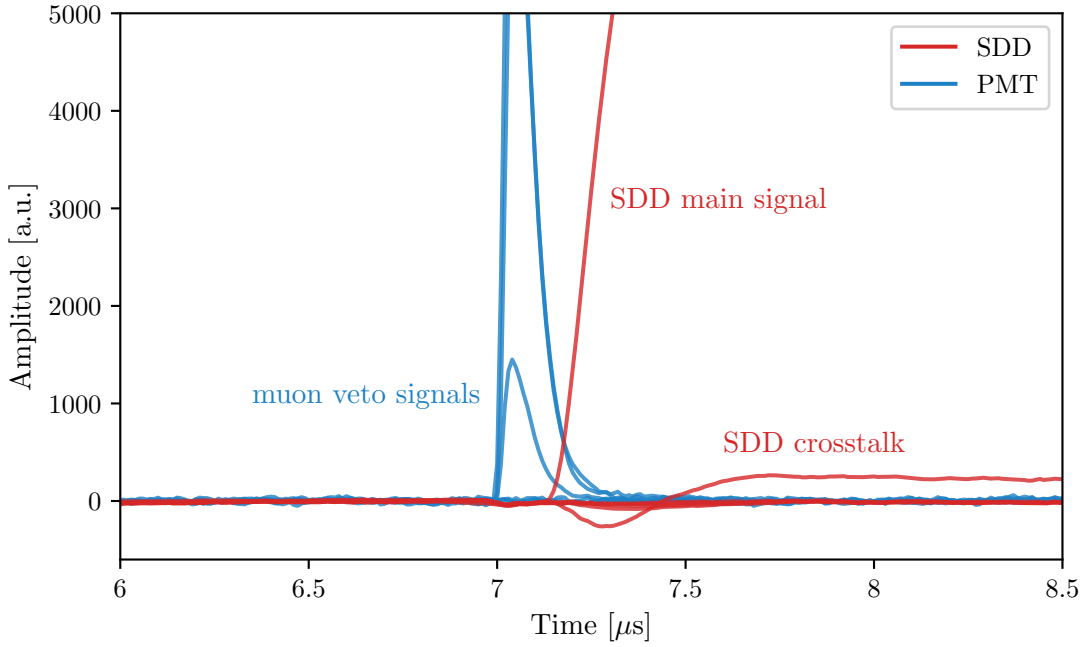

Figure 37: **Example for a muon event with crosstalk between SDD pixels**
Three of the PMT waveforms show a positive pulse, which indicates a muon passing through the veto. One pixel of the SDD has a signal shortly after, which induces crosstalk on another pixel. That pixel's waveform drops first, before rising again to a level above the baseline. Crosstalk is treated as a real signal by the DSP and is not removed by quality cuts if it has a high enough reconstructed energy. The time difference between the muon veto signals and the crosstalk signal is larger than the difference between the muon veto and the main signal and therefore explains the two distinct peaks in Figure 36.

There are almost no time differences outside those two peaks. This means that muon veto events almost always match an SDD event. In the background measurement, pulser-induced events will be used to measure the random coincidence. Since there were no nearby events outside the two peaks, I set a generous coincidence time window from $-0.5\,\mu s$ to $1\,\mu s$ that covers both peaks. If an SDD event has a muon event within this time window, it is counted as a muon-induced event and removed by the muon veto cut.

4.3.4. Results

Over the ten days of measurement, around 200000 events were recorded. After the SDD quality cuts, 7% of them remained. On those, I applied the muon veto cut. It removed around half of the remaining events. To see if the veto and analysis chain worked as intended and actually removed prompt muon events, I plotted the energy spectrum of the SDD, both after the muon veto cut and for only those events that were removed by the cut, in Figure 38.

The raw SDD spectrum shows a clear bump above 100 keV. The minimal ionization energy deposited by muons is roughly 2 MeV per cm [60]. A hill in the energy spectrum starting at 100 keV for a 0.5 mm thick detector is therefore consistent with muons passing through the SDD directly. The energy deposition of muons in material follows a so-called Landau distribution, a distribution with a long tail towards higher energies [4]. The events in this Landau shape are removed by the muon veto. In addition to these high-energy events, there are also lower-energy events removed by the muon veto. Those are most likely from secondary effects of muons, for example fluorescence caused by muons interacting with material near the detector. These types of events are also observed in the background simulations.

In theory, it is possible for events to be randomly coincident with the muon veto. However, the fact that the timing histogram shows the time differences clustered in the two peaks, with no 'base' of randomly distributed time differences, indicates that random coincidence is negligible for this analysis. This also matches the negligible number of random coincidences observed in the time shift analysis done during the detection efficiency measurement. The coincident measurement shows that the muon veto system is fully functional and can be used to take long-term background data with the SDD.

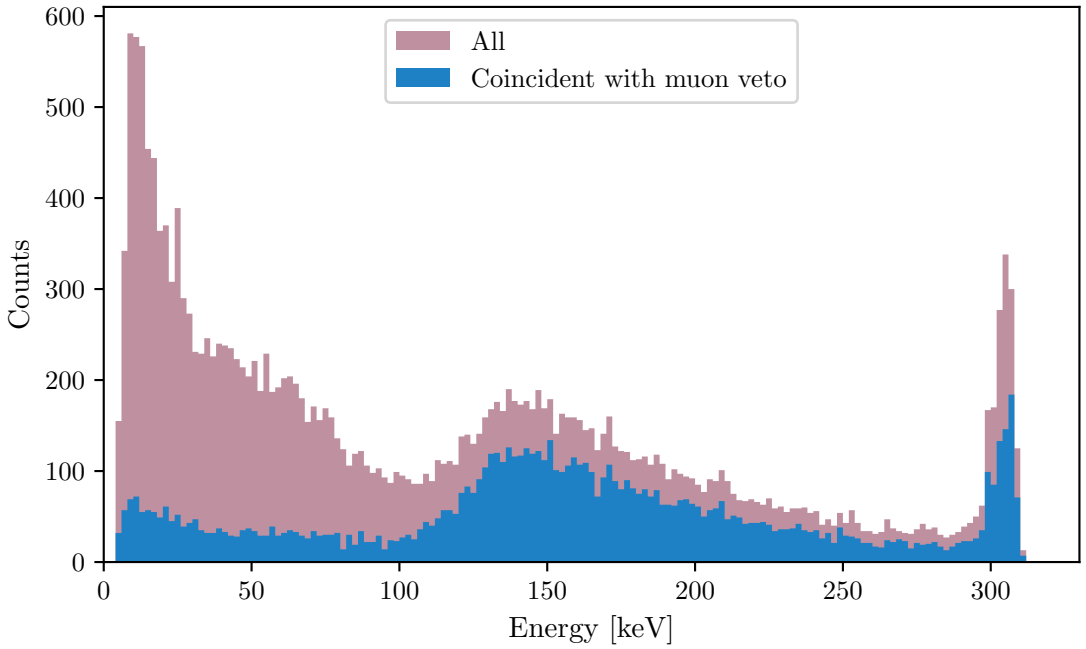

(a) **Events removed by the muon veto cut**

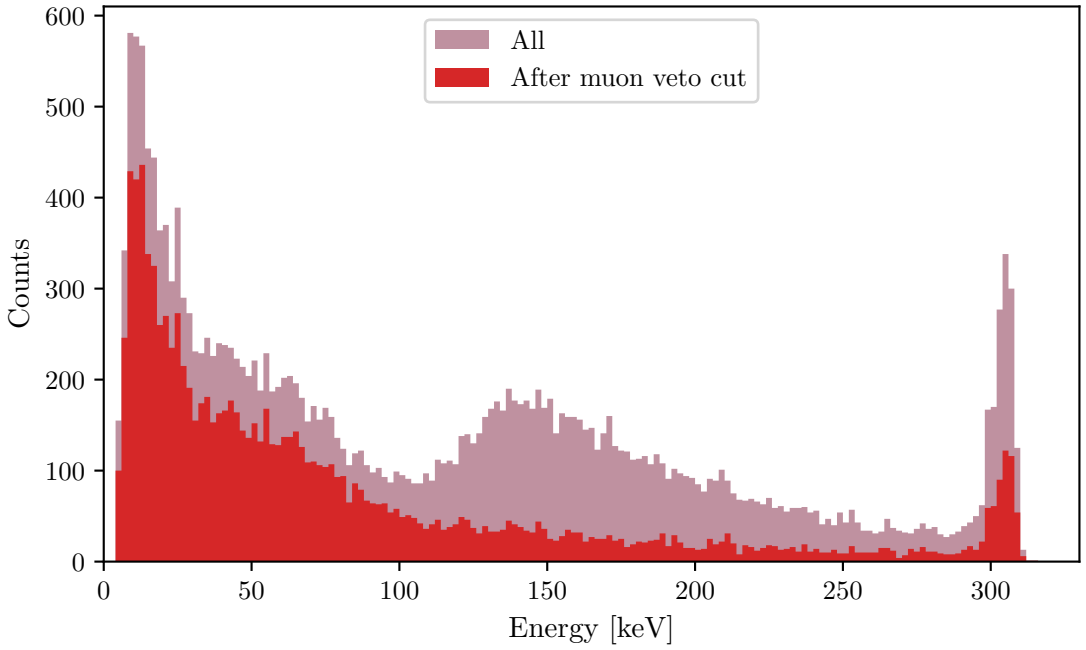

(b) **Events remaining after the muon veto cut**

Figure 38: **SDD spectrum with muon veto cut**
Both plots show the combined energy spectrum of all SDD pixels. The peak at the high-energy end of the spectrum is from oversaturation, since there are events with energies higher than the dynamic range of the DAQ system. The hill above 100 keV is from direct muon events in the SDD. This hill is removed by the muon veto cut, leaving only a background spectrum with a vaguely exponential shape. The muon veto cut also removes events across the whole energy range that were likely caused by secondaries.

5. Conclusion and Outlook

This thesis lays essential groundwork for the future of the TAXO project, aiming to develop a low-background SDD setup for the BabyIAXO experiment. The main challenge for the detectors of TAXO is reaching a background of 10^{-7} cts/(cm^2 s keV) above ground. This requires reducing the background caused by cosmic shower particles as much as possible. This thesis contributes to the solution of this problem in two ways: Firstly, the cosmic background simulations show how the background from cosmic shower particles is produced, how it is affected by different shielding concepts, and, most importantly, where there is potential to reduce it. Secondly, the development of a muon veto setup is a critical step in establishing a demonstrator setup above ground. This demonstrator will take low-background data and test different shielding concepts to test the predictions of the simulations.

The simulations revealed that of all cosmic shower particles, and after applying a muon veto cut, neutrons are the leading cause of background. They initiate chains of processes that result in neutrons, gammas, or other particles hitting the SDD. Shielding against neutrons is not trivial but adding one layer of PE(Bo) was shown to be effective at reducing the background by 60%. A multi-layered shielding concept reduced it by 50% yet again, through a combination of slowing down high-energy neutrons, capturing them, and shielding against secondaries. The concept can be further optimized in the future. Since previous efforts regarding the cosmic background were focused on muons, these simulations revealed the importance of neutrons for the first time and allowed for an important adjustment of the background mitigation strategy.

The reduction in background from adding PE(Bo) can be verified in experiment but requires a functioning demonstrator setup above ground. For this purpose, an all-new muon veto setup was commissioned, characterized, and tested in the scope of this thesis. It was built from six plastic scintillator panels read out by PMTs. Their detection efficiency was measured to be above 98%. The first coincidence measurement with both the veto and the SDD led to the development of a fully functioning DAQ and analysis chain and showed that the veto can successfully identify prompt muon-induced events among the SDD data. It is ready for a long-term background measurement.

The next step is the low-background phase of the TAXO demonstrator at TUM. This means adding passive shielding to the existing setup, flushing it with nitrogen, and upgrading to the latest low-background SDD design. It can then take background data. This data can be compared to the data from the demonstrator at Canfranc to isolate the contribution of cosmic particles and compare it to the simulations. The next step after that is adding the neutron shield. There are PE(Bo) plates already at TUM that will be constructed into an additional layer of shielding inside the muon veto. Taking data with this setup will test the reduction in background due to PE(Bo) shown in the simulations.

In the long term, the setup including the muon veto will be transported to DESY in Hamburg, to take background data at the actual location of BabyIAXO. This location is the HERA south hall, which has more overburden and therefore better protection from cosmic shower particles than the current location of the demonstrator at TUM. In a similar vein, the cosmic particle flux at the BabyIAXO site and a more accurate geometry of the setup can be simulated based on the work presented in this thesis.

The simulation code that was partially developed for this thesis will also be used, with slight alterations, to answer other open questions about backgrounds impacting TAXO. One question is the impact of cosmogenics, meaning radioactive isotopes that are produced by cosmic irradiation. They were not covered in this thesis and will be simulated separately. The simulations will also be used to investigate further concepts to reduce the cosmic background, for example using other neutron absorber materials, developing a system to tag neutrons, or surrounding the SDD by a germanium detector as an active veto. The latter strategy is currently being worked on in the laboratory as well. There are many activities going on within the TAXO project, and this work was one step in bringing it closer to IAXO.

A. Detailed Tracking Plots

The cosmic background simulations discussed in Chapter 3 tracked the production of new particles in the shielding materials. For each background event, i.e., events with an energy deposition in the ROI of (2 to 10) keV that were not removed by the muon veto cut, I plotted the full track that led to the SDD hit. These tracks show the series of processes and particles from the incident particle to the SDD hit. They were the basis for the results in Section 3.3.

The tracks can be read left to right. The particle and process that caused an SDD hit, or the first if there were several, is the leftmost marker at $r = 0\,\text{mm}$. The track from this point shows the path of this particle through the shielding up to the point where it was created. In this way, one can follow the series of particles and their respective creation processes in the different shielding materials for each event. Figure 39 is the shared legend for all plots, explaining the markers and colours. Figures 40 to 44 are the actual tracking plots for the different shielding configurations.

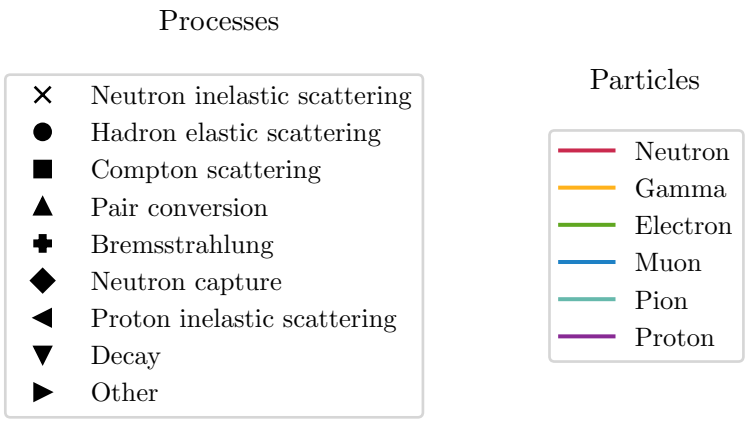

Figure 39: **Legend for the tracking plots**
Legend explaining the markers and colors for the tracking plots. The markers symbolize different processes, the colours of tracks and markers are different particles. The tracks of all background events are plotted in the following figures for each shielding concept:
The standard setup in Figures 40 and 41;
The PE(Bo) inner setup in Figure 42;
The PE(Bo) outer setup in Figure 43;
The multi-layer setup in Figure 44.

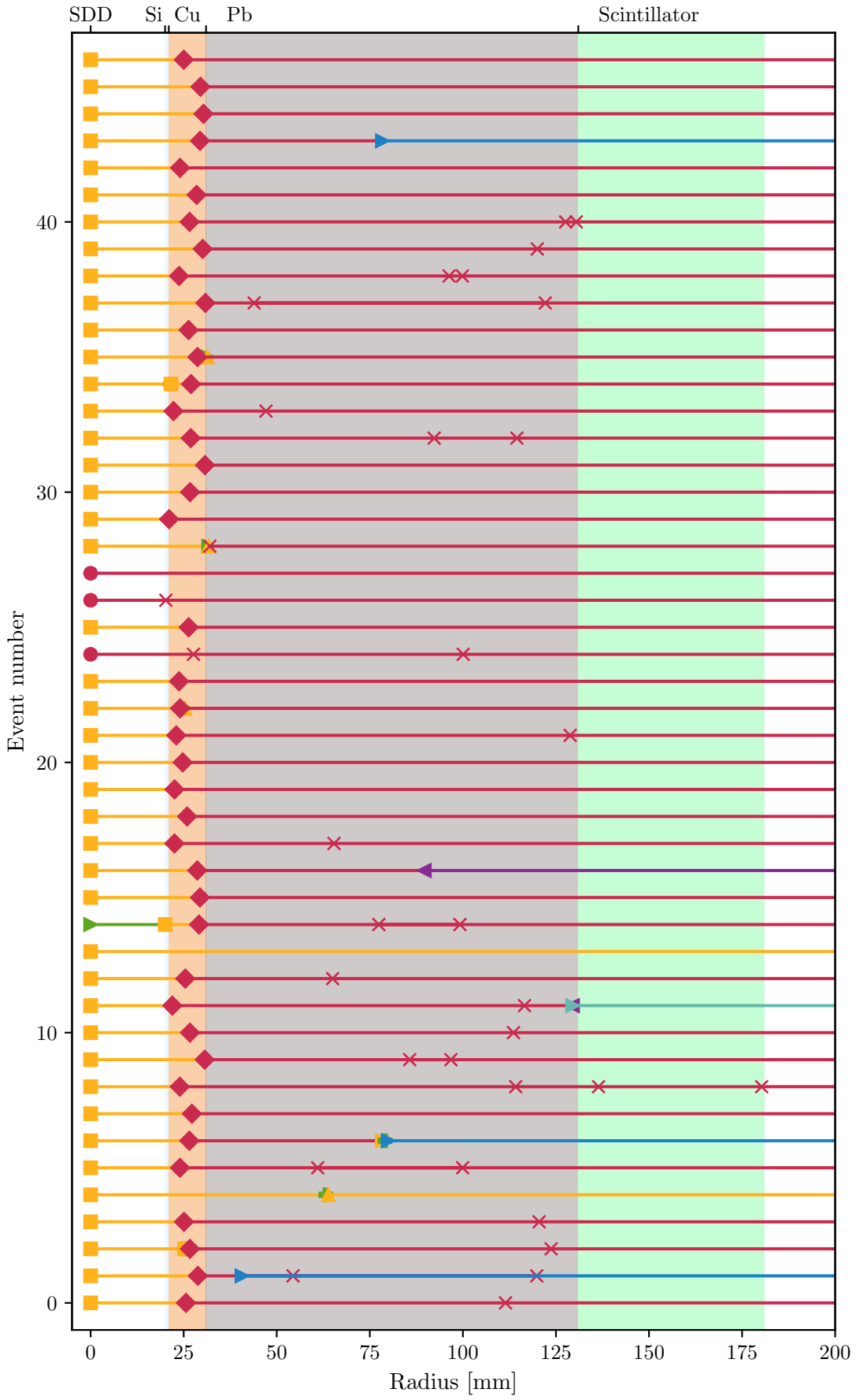

Figure 40: **Tracking plot of the standard setup (part 1)**
The legend for this plot can be found in Figure 39.

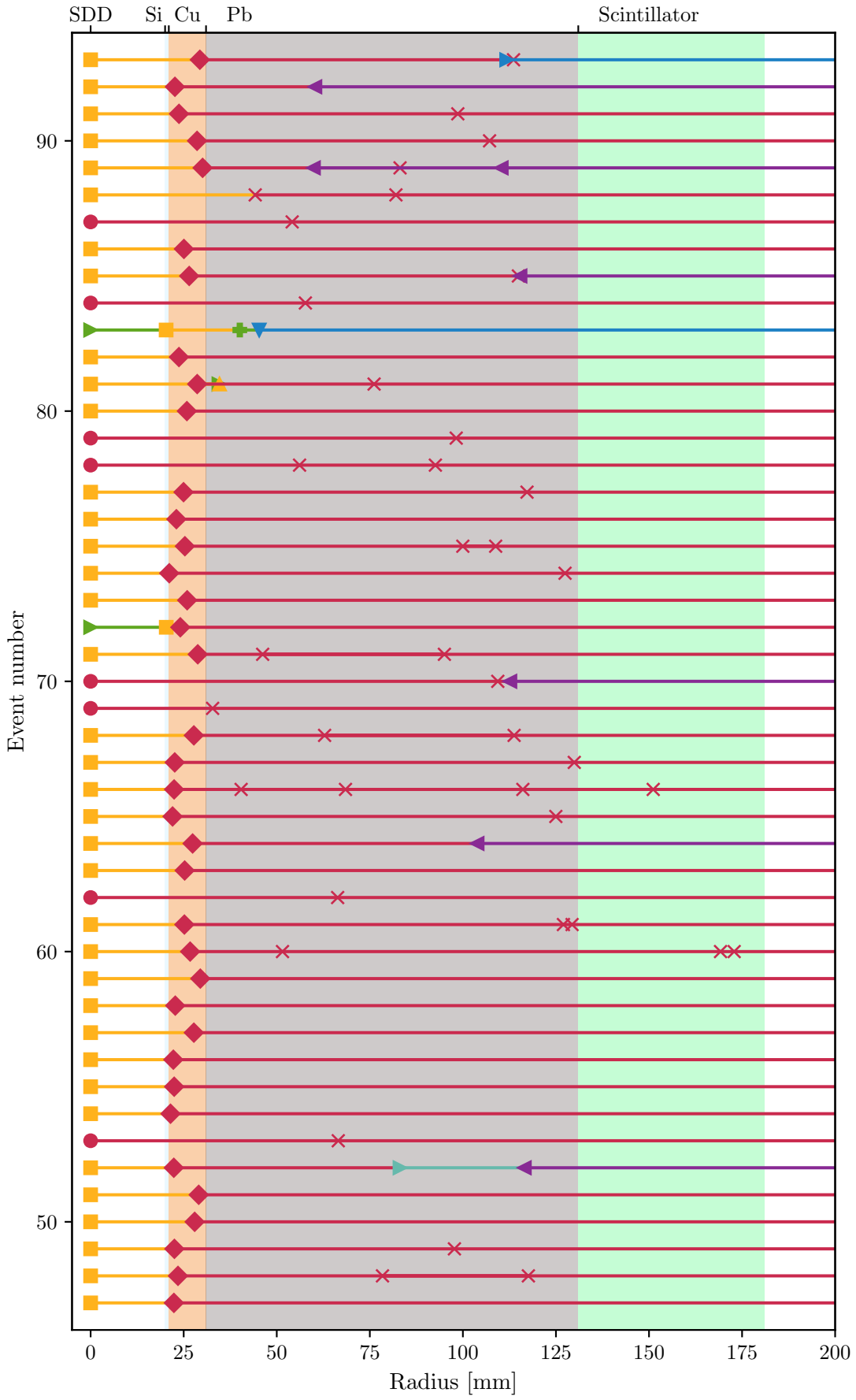

Figure 41: **Tracking plot of the standard setup (part 2)**
The legend for this plot can be found in Figure 39.

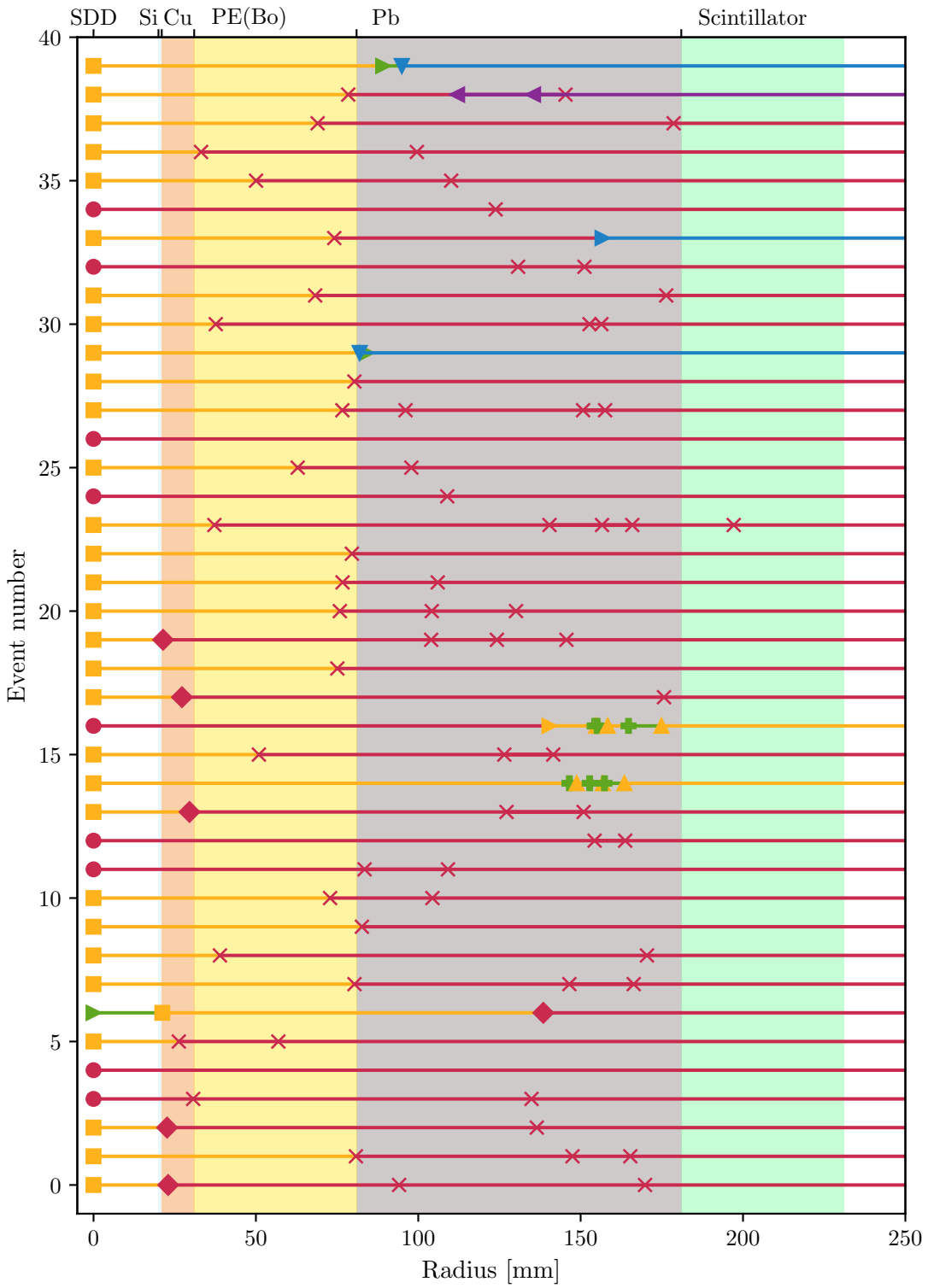

Figure 42: **Tracking plot of the PE(Bo) inner setup**
The legend for this plot can be found in Figure 39.

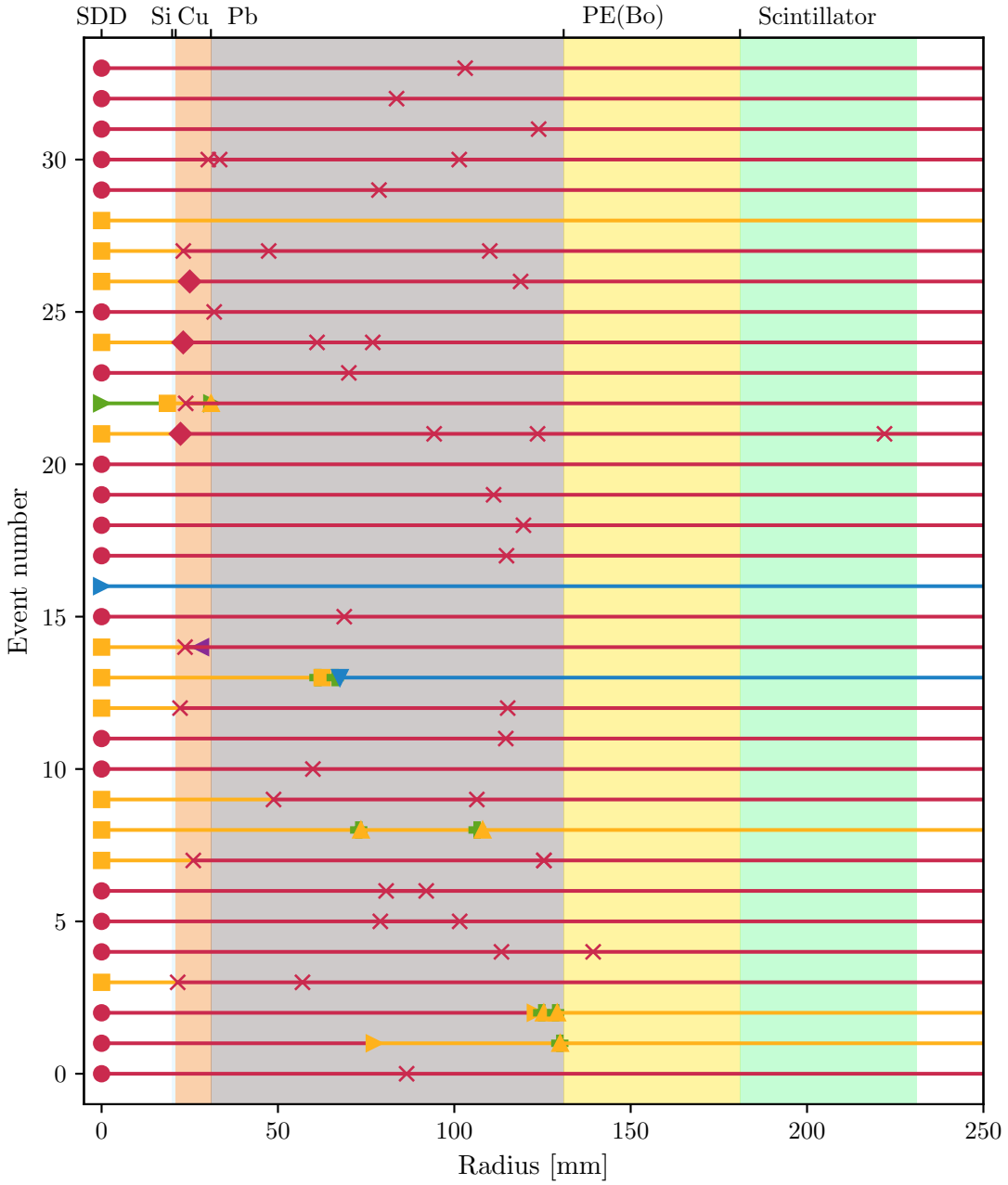

Figure 43: **Tracking plot of the PE(Bo) outer setup**
The legend for this plot can be found in Figure 39.

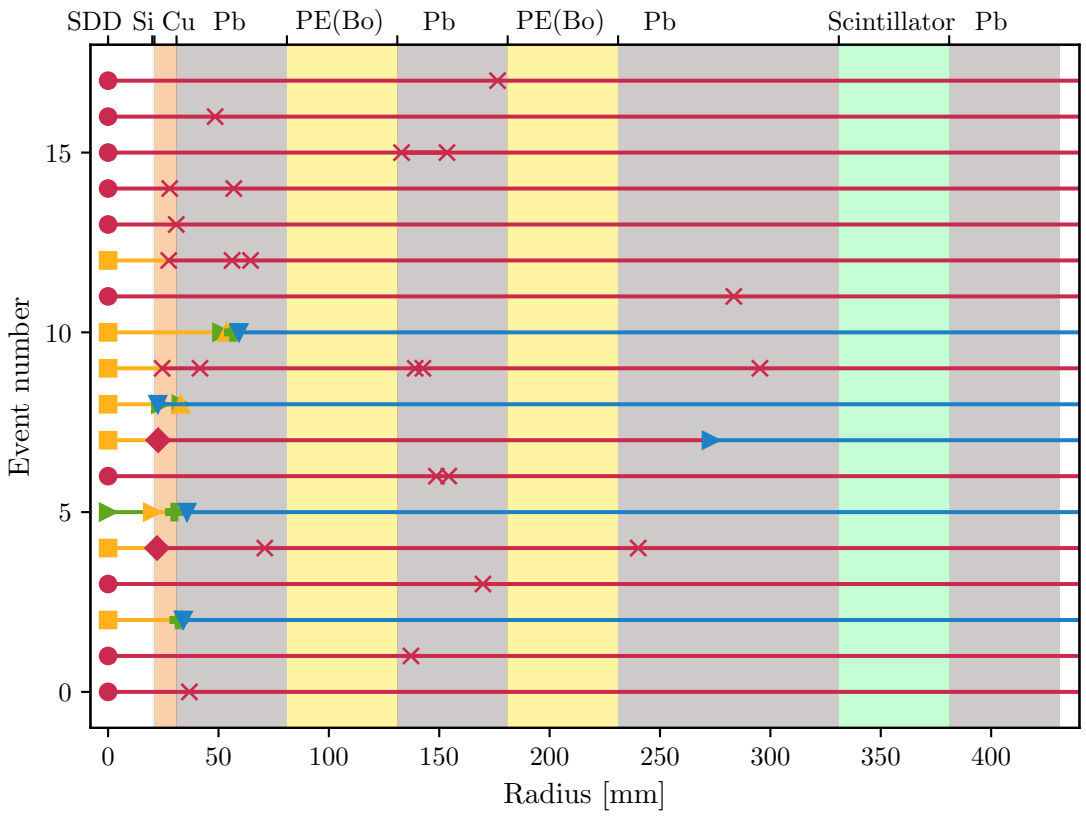

Figure 44: **Tracking plot of the multi-layer setup**
The legend for this plot can be found in Figure 39.

B. Measurement Parameters

These were the settings of the coincidence measurement and can be the basis for any other measurement with the TAXO demonstrator.

Operation Voltages for the Muon Veto Panels

The muon veto panels were delivered with a data sheet listing the following operation voltages:

Panel number	1	2	3	4	5	6
Operation voltage [V]	626	638	605	641	705	693

Logic Unit Settings

The VETO+OR section of the LU was configured with the following settings:

I/O settings	IN	VETO	OUT
50 Ω impedance	TTL; Gate: 1000 ns	TTL; Gate: 10000 ns	TTL; Value: 1000 ns

CoMPASS Settings

Settings that are not listed were left at their default values. The master board receives the muon veto panel waveforms, it was configured as follows:

Input		Synchronization		Misc	
Rec. len.:	20000 ns	Start:	first TRG	Label:	CH
Pre-trig.:	8000 ns	TRG OUT:	software	FPIO type:	TTL
Polarity:	negative	Start delay:	0		
N samples:	256	Offset:	0		
DC offset:	20%				
Fine gain:	1.0X				

The slave board receives the SDD pixel waveforms. It needs to be configured into the low gain mode by opening the casing and setting the jumper of each channel from x1.0 to x0.2. It was configured as follows:

Input		Discriminator		Trapezoid	
Rec. len.:	20000 ns	Threshold:	150 lsb	Rise time:	2 μs
Pre-trig.:	8000 ns	Holdoff:	480 ns	Flat top:	0.5 μs
Polarity:	negative	Smoothing:	16	Pole zero	15 μs
N samp.:	256	Rise time:	200 ns	Peaking:	80%
DC offset:	40%				
Fine gain:	1.0X				

Rejections	Synchronization		Misc	
Disable all	Start:	first TRG	Label:	CH
	TRG OUT:	software	FPIO type:	TTL
	Start delay:	0		
	Offset:	0		

Freewrites File

In order for the DAQ boards to propagate the right signals to their TRG OUT and read out channels in the correct way, they have to be programmed with a so-called freewrites file. I wrote this file for the coincidence measurement. It can be used in any setup where the SDD and muon veto are to be operated together in the same way. The labels `<master>` and `<slave>` have to be replaced with the IDs of the respective boards, which can be found in the CoMPASS interface.

```
<slave> 0x1080 0x1000000 0x1000000
<slave> 0x1180 0x1000000 0x1000000
<slave> 0x1280 0x1000000 0x1000000
<slave> 0x1380 0x1000000 0x1000000
<slave> 0x1480 0x1000000 0x1000000
<slave> 0x1580 0x1000000 0x1000000
<slave> 0x1680 0x1000000 0x1000000
<slave> 0x1780 0x1000000 0x1000000
<master> 0x1080 0x1000000 0x1000000
<master> 0x1180 0x1000000 0x1000000
<master> 0x1280 0x1000000 0x1000000
<master> 0x1380 0x1000000 0x1000000
<master> 0x1480 0x1000000 0x1000000
<master> 0x1580 0x1000000 0x1000000
<master> 0x1680 0x1000000 0x1000000
<master> 0x1780 0x1000000 0x1000000
<slave> 0x10A0 0x300 0x300
<slave> 0x11A0 0x300 0x300
<slave> 0x12A0 0x300 0x300
<slave> 0x13A0 0x300 0x300
<slave> 0x14A0 0x300 0x300
<slave> 0x15A0 0x300 0x300
<slave> 0x16A0 0x300 0x300
<slave> 0x17A0 0x300 0x300
<slave> 0x810C 0x40000000 0x40000000
<master> 0x810C 0x40000000 0x40000000
<slave> 0x8110 0xFF 0xFF
<master> 0x8110 0x40000000 0x40000000
```

List of Figures

Acronyms

ALP	axion-like particle
BabyIAXO	prototype for IAXO
CAST	CERN Axion Solar Telescope
CRY	Cosmic-Ray Particle Library
DAQ	data acquisition
DESY	Deutsches Elektronen-Synchrotron
DSP	digital signal processing
FADC	flash analog-digital converter
HERA	Hadron-Elektron-Ring-Anlage
HV	high voltage
IAXO	International Axion Observatory
LSC	Laboratorio Subterráneo de Canfranc
LSW	light shining through a wall
LU	logic unit
nEDM	electric dipole moment of the neutron
PCB	printed circuit board
PE(Bo)	borated polyethylene
PMT	photomultiplier tube
PQ	Peccei-Quinn
QCD	quantum chromodynamics
ROI	region of interest
SDD	silicon drift detector
SM	Standard Model
TAXO	TRISTAN SDD for IAXO
TUM	Technische Universität München

References

[1] Igor García Irastorza. "An introduction to axions and their detection". In: *SciPost Phys. Lect. Notes* (2022), p. 45. DOI: 10.21468/SciPostPhysLectNotes.45. URL: https://scipost.org/10.21468/SciPostPhysLectNotes.45.

[2] David J. E. Marsh. "Axions and ALPs: a very short introduction". In: *13th Patras Workshop on Axions, WIMPs and WISPs*. 2018, pp. 59–74. DOI: 10.3204/DESY-PROC-2017-02/marsh_david. arXiv: 1712.03018 [hep-ph].

[3] J. H. Christenson et al. "Evidence for the 2π Decay of the K_2^0 Meson". In: *Phys. Rev. Lett.* 13 (4 July 1964), pp. 138–140. DOI: 10.1103/PhysRevLett.13.138. URL: https://link.aps.org/doi/10.1103/PhysRevLett.13.138.

[4] R. L. Workman et al. "Review of Particle Physics". In: *PTEP* 2022 (2022), p. 083C01. DOI: 10.1093/ptep/ptac097.

[5] C. Abel et al. "Measurement of the Permanent Electric Dipole Moment of the Neutron". In: *Phys. Rev. Lett.* 124 (8 Feb. 2020), p. 081803. DOI: 10.1103/PhysRevLett.124.081803. URL: https://link.aps.org/doi/10.1103/PhysRevLett.124.081803.

[6] Maxim Pospelov and Adam Ritz. "Electric dipole moments as probes of new physics". In: *Annals of Physics* 318.1 (2005). Special Issue, pp. 119–169. ISSN: 0003-4916. DOI: https://doi.org/10.1016/j.aop.2005.04.002. URL: https://www.sciencedirect.com/science/article/pii/S0003491605000539.

[7] R. D. Peccei and Helen R. Quinn. "CP Conservation in the Presence of Pseudoparticles". In: *Phys. Rev. Lett.* 38 (25 June 1977), pp. 1440–1443. DOI: 10.1103/PhysRevLett.38.1440. URL: https://link.aps.org/doi/10.1103/PhysRevLett.38.1440.

[8] R. D. Peccei and Helen R. Quinn. "Constraints imposed by CP conservation in the presence of pseudoparticles". In: *Phys. Rev. D* 16 (6 Sept. 1977), pp. 1791–1797. DOI: 10.1103/PhysRevD.16.1791. URL: https://link.aps.org/doi/10.1103/PhysRevD.16.1791.

[9] J. Goldstone. "Field Theories with Superconductor Solutions". In: *Nuovo Cim.* 19 (1961), pp. 154–164. DOI: 10.1007/BF02812722.

[10] Daniel Kastler, Derek W. Robinson, and André Swieca. "Conserved currents and associated symmetries; Goldstone's theorem". In: *Commun. Math. Phys.* 2.1 (1966), pp. 108–120. DOI: 10.1007/BF01773346.

[11] Steven Weinberg. "A New Light Boson?" In: *Phys. Rev. Lett.* 40 (4 Jan. 1978), pp. 223–226. DOI: 10.1103/PhysRevLett.40.223. URL: https://link.aps.org/doi/10.1103/PhysRevLett.40.223.

[12] F. Wilczek. "Problem of Strong P and T Invariance in the Presence of Instantons". In: *Phys. Rev. Lett.* 40 (5 Jan. 1978), pp. 279–282. DOI: 10.1103/PhysRevLett.40.279. URL: https://link.aps.org/doi/10.1103/PhysRevLett.40.279.

[13] Giovanni Grilli di Cortona et al. "The QCD axion, precisely". In: *JHEP* 01 (2016), p. 034. DOI: 10.1007/JHEP01(2016)034. arXiv: 1511.02867 [hep-ph].

[14] Y. Asano et al. "Search for a rare decay mode K+ → + ν and axion". In: *Physics Letters B* 107.1 (1981), pp. 159–162. ISSN: 0370-2693. DOI: https://doi.org/10.

1016/0370-2693(81)91172-2. URL: https://www.sciencedirect.com/science/article/pii/0370269381911722.

[15] Mikhail A. Shifman, A. I. Vainshtein, and Valentin I. Zakharov. "Can Confinement Ensure Natural CP Invariance of Strong Interactions?" In: *Nucl. Phys. B* 166 (1980), pp. 493–506. DOI: 10.1016/0550-3213(80)90209-6.

[16] Jihn E. Kim. "Weak-Interaction Singlet and Strong CP Invariance". In: *Phys. Rev. Lett.* 43 (2 July 1979), pp. 103–107. DOI: 10.1103/PhysRevLett.43.103. URL: https://link.aps.org/doi/10.1103/PhysRevLett.43.103.

[17] Michael Dine, Willy Fischler, and Mark Srednicki. "A simple solution to the strong CP problem with a harmless axion". In: *Physics Letters B* 104.3 (1981), pp. 199–202. ISSN: 0370-2693. DOI: https://doi.org/10.1016/0370-2693(81)90590-6. URL: https://www.sciencedirect.com/science/article/pii/0370269381905906.

[18] A. Ringwald. "Axions and Axion-Like Particles". In: *49th Rencontres de Moriond on Electroweak Interactions and Unified Theories*. 2014, pp. 223–230. arXiv: 1407.0546 [hep-ph].

[19] N. Aghanim et al. "Planck 2018 results. I. Overview and the cosmological legacy of Planck". In: *Astron. Astrophys.* 641 (2020), A1. DOI: 10.1051/0004-6361/201833880. arXiv: 1807.06205 [astro-ph.CO].

[20] Paola Arias et al. "WISPy Cold Dark Matter". In: *JCAP* 06 (2012), p. 013. DOI: 10.1088/1475-7516/2012/06/013. arXiv: 1201.5902 [hep-ph].

[21] Ciaran A. J. O'Hare. "Cosmology of axion dark matter". In: (Mar. 2024). arXiv: 2403.17697 [hep-ph].

[22] Ciaran O'Hare. *cajohare/AxionLimits: AxionLimits*. https://cajohare.github.io/AxionLimits/. Version v1.0. Last updated and accessed Feb 27 2024. July 2020. DOI: 10.5281/zenodo.3932430.

[23] Georg G. Raffelt. "Astrophysical axion bounds". In: *Lect. Notes Phys.* 741 (2008). Ed. by Markus Kuster, Georg Raffelt, and Berta Beltran, pp. 51–71. DOI: 10.1007/978-3-540-73518-2_3. arXiv: hep-ph/0611350.

[24] Ryan Janish and Elena Pinetti. "Hunting Dark Matter Lines in the Infrared Background with the James Webb Space Telescope". In: (Oct. 2023). arXiv: 2310.15395 [hep-ph].

[25] R. Khatiwada et al. "Axion Dark Matter Experiment: Detailed design and operations". In: *Rev. Sci. Instrum.* 92.12 (2021), p. 124502. DOI: 10.1063/5.0037857. arXiv: 2010.00169 [astro-ph.IM].

[26] Antonios Gardikiotis. "Advances in Searching for Galactic Axions with a Dielectric Haloscope (MADMAX)". In: *Annalen Phys.* 536.1 (2024), p. 2300046. DOI: 10.1002/andp.202300046.

[27] Chiara P. Salemi. "The First Laboratory Searches for Low-Mass Axion Dark Matter". PhD thesis. MIT, 2022.

[28] Isabella Oceano. "Axion and ALP search with the Any Light Particle Search II experiment at DESY". In: *PoS* EPS-HEP2023 (2024), p. 117. DOI: 10.22323/1.449.0117.

[29] S. Andriamonje et al. “An Improved limit on the axion-photon coupling from the CAST experiment”. In: *JCAP* 04 (2007), p. 010. DOI: 10.1088/1475-7516/2007/04/010. arXiv: hep-ex/0702006.

[30] Igor Irastorza et al. “The International Axion Observatory IAXO. Letter of Intent to the CERN SPS committee”. In: (Aug. 2013).

[31] A. Álvarez Melcón et al. “Scalable haloscopes for axion dark matter detection in the 30μeV range with RADES”. In: *JHEP* 07 (2020), p. 084. DOI: 10.1007/JHEP07(2020)084. arXiv: 2002.07639 [hep-ex].

[32] T. O’Shea et al. “Prospects on the Detection of Solar Dark Photons by the International Axion Observatory”. In: (Dec. 2023). arXiv: 2312.10150 [hep-ph].

[33] J. Ruz et al. “The CAST experiment”. In: *J. Phys. Conf. Ser.* 110 (2008). Ed. by Roger Barlow, p. 062023. DOI: 10.1088/1742-6596/110/6/062023.

[34] R. Kotthaus et al. “The X-ray Telescope of the CAST Experiment”. In: (Dec. 2005). DOI: 10.48550/arXiv.astro-ph/0511390.

[35] E. Armengaud et al. “Conceptual Design of the International Axion Observatory (IAXO)”. In: *JINST* 9 (2014), T05002. DOI: 10.1088/1748-0221/9/05/T05002. arXiv: 1401.3233 [physics.ins-det].

[36] Andreas Abeln et al. “Conceptual design of BabyIAXO, the intermediate stage towards the International Axion Observatory”. In: *Journal of High Energy Physics* 2021 (May 2021). DOI: 10.1007/JHEP05(2021)137.

[37] I. G. Irastorza et al. “Towards a new generation axion helioscope”. In: *JCAP* 06 (2011), p. 013. DOI: 10.1088/1475-7516/2011/06/013. arXiv: 1103.5334 [hep-ex].

[38] F. Aznar et al. “A Micromegas-based low-background x-ray detector coupled to a slumped-glass telescope for axion research”. In: *Journal of Cosmology and Astroparticle Physics* 2015.12 (Dec. 2015), p. 008. DOI: 10.1088/1475-7516/2015/12/008. URL: https://dx.doi.org/10.1088/1475-7516/2015/12/008.

[39] K. Altenmüller et al. “X-ray detectors for the BabyIAXO solar axion search”. In: *Nuclear Instruments and Methods in Physics Research Section A: Accelerators, Spectrometers, Detectors and Associated Equipment* 1048 (2023), p. 167913. ISSN: 0168-9002. DOI: https://doi.org/10.1016/j.nima.2022.167913. URL: https://www.sciencedirect.com/science/article/pii/S0168900222012050.

[40] C. Ligtenberg et al. “Performance of a GridPix detector based on the Timepix3 chip”. In: *Nuclear Instruments and Methods in Physics Research Section A: Accelerators, Spectrometers, Detectors and Associated Equipment* 908 (2018), pp. 18–23. ISSN: 0168-9002. DOI: https://doi.org/10.1016/j.nima.2018.08.012. URL: https://www.sciencedirect.com/science/article/pii/S0168900218309549.

[41] Krieger, Christoph et al. “Operation of an InGrid based X-ray detector at the CAST experiment”. In: *EPJ Web Conf.* 174 (2018), p. 02008. DOI: 10.1051/epjconf/201817402008. URL: https://doi.org/10.1051/epjconf/201817402008.

[42] S. Kempf et al. “Physics and Applications of Metallic Magnetic Calorimeters”. In: *J. Low Temp. Phys.* 193.3 (2018), pp. 365–379. DOI: 10.1007/s10909-018-1891-6.

[43] D. Unger et al. “High-resolution for IAXO: MMC-based X-ray detectors”. In: *Journal of Instrumentation* 16.06 (June 2021), P06006. DOI: 10.1088/1748-0221/16/06/P06006. URL: https://dx.doi.org/10.1088/1748-0221/16/06/P06006.

[44] V. Anastassopoulos et al. “Search for chameleons with CAST”. In: *Phys. Lett. B* 749 (2015), pp. 172–180. DOI: 10.1016/j.physletb.2015.07.049. arXiv: 1503.04561 [astro-ph.SR].

[45] Caroline Fengler. “Overview of KATRIN Results on the Neutrino Mass and New Physics Searches”. In: *PoS* DISCRETE2022 (2024), p. 011. DOI: 10.22323/1.431.0011.

[46] Susanne Mertens et al. “A novel detector system for KATRIN to search for keV-scale sterile neutrinos”. In: *Journal of Physics G: Nuclear and Particle Physics* 46.6 (May 2019), p. 065203. DOI: 10.1088/1361-6471/ab12fe. URL: https://dx.doi.org/10.1088/1361-6471/ab12fe.

[47] Gerhard Lutz. *Semiconductor Radiation Detectors: Device Physics*. New York: Springer, 2007. ISBN: 978-3-540-64859-8.

[48] Douglas S. McGregor. *Semiconductor Radiation Detectors*. Ed. by Ivor Fleck et al. Cham: Springer International Publishing, 2021, pp. 451–493. ISBN: 978-3-319-93785-4. DOI: 10.1007/978-3-319-93785-4_16. URL: https://doi.org/10.1007/978-3-319-93785-4_16.

[49] Emilio Gatti and Pavel Rehak. “Semiconductor drift chamber — An application of a novel charge transport scheme”. In: *Nuclear Instruments and Methods in Physics Research* 225.3 (1984), pp. 608–614. ISSN: 0167-5087. DOI: https://doi.org/10.1016/0167-5087(84)90113-3. URL: https://www.sciencedirect.com/science/article/pii/0167508784901133.

[50] V Radeka. “Low-Noise Techniques in Detectors”. In: *Annual Review of Nuclear and Particle Science* 38.1 (1988), pp. 217–277. DOI: 10.1146/annurev.ns.38.120188.001245. eprint: https://doi.org/10.1146/annurev.ns.38.120188.001245. URL: https://doi.org/10.1146/annurev.ns.38.120188.001245.

[51] Daniel Siegmann. “Investigation of the Detector Response to Electrons of the TRISTAN Prototype Detectors”. TUM, 2019.

[52] Korbinian Urban. personal communications. 2022.

[53] S Mertens et al. “Characterization of silicon drift detectors with electrons for the TRISTAN project”. In: *Journal of Physics G: Nuclear and Particle Physics* 48.1 (Dec. 2020), p. 015008. DOI: 10.1088/1361-6471/abc2dc. URL: https://dx.doi.org/10.1088/1361-6471/abc2dc.

[54] D.M. Schlosser et al. “Expanding the detection efficiency of silicon drift detectors”. In: *Nuclear Instruments and Methods in Physics Research Section A: Accelerators, Spectrometers, Detectors and Associated Equipment* 624.2 (2010). New Developments in Radiation Detectors, pp. 270–276. ISSN: 0168-9002. DOI: https://doi.org/10.1016/j.nima.2010.04.038. URL: https://www.sciencedirect.com/science/article/pii/S0168900210008879.

[55] Christoph Wiesinger. personal communications. 2022.

[56] Rolf F. Barth et al. “Boron Neutron Capture Therapy of Cancer: Current Status and Future Prospects”. In: *Clinical Cancer Research* 11.11 (June 2005), pp. 3987–

4002. ISSN: 1078-0432. DOI: 10.1158/1078-0432.CCR-05-0035. eprint: https://aacrjournals.org/clincancerres/article-pdf/11/11/3987/1956671/3987-4002.pdf. URL: https://doi.org/10.1158/1078-0432.CCR-05-0035.

[57] Joanna Bilicki. "Commissioning and Characterisation of a low-background Silicon Drift Detector Setup at the Canfranc Deep Underground Laboratory". TUM, 2023.

[58] Elisa Ruiz Chóliz. "Ultra-low background Micromegas X-ray detectors for Axion searches in IAXO and BabyIAXO". Zaragoza U., 2019.

[59] Claus Grupen. "Primary Cosmic Rays". In: *Astroparticle Physics*. Cham: Springer International Publishing, 2020, pp. 121–233. ISBN: 978-3-030-27339-2. DOI: 10.1007/978-3-030-27339-2_6. URL: https://doi.org/10.1007/978-3-030-27339-2_6.

[60] Francesco Riggi. "Interaction of Muons with Matter". In: *Messengers from the Cosmos: An Introduction to the Physics of Cosmic Rays in Its Historical Evolution*. Cham: Springer Nature Switzerland, 2023, pp. 241–247. ISBN: 978-3-031-24762-0. DOI: 10.1007/978-3-031-24762-0_13. URL: https://doi.org/10.1007/978-3-031-24762-0_13.

[61] Claus Grupen. "Secondary Cosmic Rays". In: *Astroparticle Physics*. Cham: Springer International Publishing, 2020, pp. 235–291. ISBN: 978-3-030-27339-2. DOI: 10.1007/978-3-030-27339-2_7. URL: https://doi.org/10.1007/978-3-030-27339-2_7.

[62] Francesco Riggi. "The Secondary Cosmic Radiation". In: *Messengers from the Cosmos: An Introduction to the Physics of Cosmic Rays in Its Historical Evolution*. Cham: Springer Nature Switzerland, 2023, pp. 195–210. ISBN: 978-3-031-24762-0. DOI: 10.1007/978-3-031-24762-0_10. URL: https://doi.org/10.1007/978-3-031-24762-0_10.

[63] Lawrence Livermore National Laboratory. *Cosmic-ray Shower Library (CRY)*. https://nuclear.llnl.gov/simulation/main.html.

[64] S. Agostinelli et al. "Geant4—a simulation toolkit". In: *Nuclear Instruments and Methods in Physics Research Section A: Accelerators, Spectrometers, Detectors and Associated Equipment* 506.3 (2003), pp. 250–303. DOI: https://doi.org/10.1016/S0168-9002(03)01368-8. URL: http://infoscience.epfl.ch/record/49909.

[65] Janina Dorin Hakenmüller. "Looking for coherent elastic neutrino nucleus scattering with the CONUS experiment". Available at https://archiv.ub.uni-heidelberg.de/volltextserver/29165/. PhD thesis. Heidelberg, GER: Heidelberg University, Oct. 2020.

[66] J Lindhard et al. "INTEGRAL EQUATIONS GOVERNING RADIATION EFFECTS. (NOTES ON ATOMIC COLLISIONS, III)". In: *Kgl. Danske Videnskab., Selskab. Mat. Fys. Medd.* Vol: 33: No. 10 (Jan. 1963). URL: https://www.osti.gov/biblio/4701226.

[67] F. Izraelevitch and et al. "A Measurement of the Ionization Efficiency of Nuclear Recoils in Silicon". In: *JINST* 12.06 (June 2017). DOI: 10.1088/1748-0221/12/06/P06014. URL: https://www.osti.gov/biblio/1469292.

[68] Aurélie Bonhomme et al. "Direct measurement of the ionization quenching factor of nuclear recoils in germanium in the keV energy range". In: *The European Physical Journal C* 82 (Sept. 2022). DOI: 10.1140/epjc/s10052-022-10768-1.

[69] Daniel Heuchel. *Background Measurements at Hera Hall South*. presentation for the internal IAXO detector call. 2023.

[70] D.A. Brown et al. "ENDF/B-VIII.0: The 8th Major Release of the Nuclear Reaction Data Library with CIELO-project Cross Sections, New Standards and Thermal Scattering Data". In: *Nuclear Data Sheets* 148 (2018). Special Issue on Nuclear Reaction Data, pp. 1–142. ISSN: 0090-3752. DOI: https://doi.org/10.1016/j.nds.2018.02.001. URL: https://www.sciencedirect.com/science/article/pii/S0090375218300206.

[71] NuviaTech Instruments. *NuDET PLASTIC Plastic Scintillation Detectors Specification Sheet*. URL: https://www.nuviatech-instruments.com/wp-content/uploads/sites/3/2017/12/NVG-375016-Fichesx4-PLASTIC-Aout2019-V3-2.pdf (visited on 04/15/2024).

[72] ET Enterprises. *9266B Series Data Sheet*. URL: https://et-enterprises.com/images/data_sheets/9266B.pdf (visited on 04/15/2024).

[73] J.L. Autran et al. "Characterization of atmospheric muons at sea level using a cosmic ray telescope". In: *Nuclear Instruments and Methods in Physics Research Section A: Accelerators, Spectrometers, Detectors and Associated Equipment* 903 (2018), pp. 77–84. ISSN: 0168-9002. DOI: https://doi.org/10.1016/j.nima.2018.06.038. URL: https://www.sciencedirect.com/science/article/pii/S0168900218307599.

[74] Christian Forstner. "Characterization of a TRISTAN Silicon Drift Detector Array with a Laser System". TUM, 2023.

Acknowledgements

For their support during my master thesis, I would like to thank the following people:

My professor, Susanne Mertens, for giving me the opportunity to work on this thesis. Thank you for being such a supportive professor who always shows interest in every student's work, for giving me the opportunity to travel to conferences and meetings, and for fostering such a humane and productive work environment at your chair.

My supervisor, Christoph Wiesinger, for his invaluable guidance throughout this thesis. Thank you for being a creative and pragmatic supervisor who let me tackle issues hands-on and learn a lot in the process. Despite your busy schedule, you always lent an ear to my questions and made time to give intelligent and effective advice.

Joanna Bilicki, for welcoming and introducing me into the chair so openly and your neverending practical advice. Beyond that, your good sense of humor and the lengthy and entertaining conversations we had about anything from contemporary art to cable car mechanics always brightened my day.

Juan Pablo Ulloa Beteta and Markus Kandler for being great colleagues and conversation partners who made working in the lab a blast. Thank you Juan especially for testing and working with the SDD together with me, which did not always go as planned, and being smart and resourceful in the face of any technical issues. Thank you Markus especially for helping me with soldering work and getting to know the SDD together, and for the life and energy you brought into the lab. The lab playlist will be sorely missed.

Frank Edzards, for the continuous support he lent to the whole TAXO effort, especially when it came to practical issues with the SDD. Thank you especially for your help proofreading my thesis.

Daniela Spreng and Christian Forstner for being great office colleagues. Thank you Daniela especially for your support with GEANT4 and brainstorming coding and simulation issues with me when I thought I was stuck. Thank you Christian for helping me out with any Linux or computer issues I encountered, and for always having a USB flash drive with the right OS or program handy.

Korbinian Urban and Daniel Siegmann for their expertise when it comes to the SDD and electronics in general. Both of you were a great source of advice and knowledge when it came to testing and debugging the SDD and bias board, thank you.

Every member of the chair E47 for experimental dark matter who supported me in one way or another, thank you.

And finally, thank you to my friends and family for your love and support all this time.